Lidar remote sensing of pesticide spray drift

Eduard Gregorio López

Dipòsit Legal: L.1419-2012
http://hdl.handle.net/10803/96788

Lidar remote sensing of pesticide spray drift

Ph.D. Dissertation

Eduard Gregorio López

Advisors:

Dr. Francesc Rocadenbosch Burillo

Dr. Ricardo Sanz Cortiella

Universitat de Lleida

Departament d'Enginyeria Agroforestal

Lleida, November 2012

Universitat de Lleida
Departament d'Enginyeria Agroforestal

Lidar remote sensing of pesticide spray drift

Ph.D. Dissertation

Submitted by

Eduard Gregorio López

Thesis Advisors:

Dr. Francesc Rocadenbosch Burillo
Remote Sensing Laboratory (RSLAB)
Departament de Teoria del Senyal i Comunicacions
Escola Tècnica Superior d'Enginyeria de Telecomunicacions de Barcelona
Universitat Politècnica de Catalunya

Dr. Ricardo Sanz Cortiella
Grup de Recerca en Agricultura de Precisió, Agròtica i Agrotecnologia (GRAP)
Departament d'Enginyeria Agroforestal
Escola Tècnica Superior d'Enginyeria Agrària
Universitat de Lleida

Als meus pares, als meus padrins i a la Marta

Acknowledgments

This PhD thesis has been conducted in the framework of the collaboration agreement between the Universitat Politècnica de Catalunya (UPC) and the Universitat de Lleida (UdL) ref. CTT A-00793 for the “Range-Resolved Remote Sensing of the Concentration of Pesticides in Agroforestry Environments”.

The following institutions are gratefully acknowledged for their contribution to this work:

- Spanish Ministry of Science and Innovation (MICINN) and FEDER (European Regional Development Fund) under the R&D projects AGL2007-66093-C04-03 and AGL2010-22304-C04-03 funding the GRAP (UdL Research Group on Precision Agriculture, AgroICT and Agrotechnology) research activities.

- MICINN and FEDER under the R&D projects REN2003-09753-C02-C02/CLI and TEC2006-07850/TCM funding the RSLab (UPC Remote Sensing Laboratory) research lidar activities.

- The lidar ceilometer prototype has been developed with the financial support of DENA Desarrollos, S.L.

And the participation in:

- MICINN under the R&D projects REN2002-12784-E/CLI and CGL2005-25131-E/CLI funding the DAMOCLES (Determinación de Aerosoles por Medidas Obtenidas en Columna (Lidar y Extinción) y Superficie) thematic network.

- European Commission under EARLINET-ASOS (European Aerosol Research Lidar Network-Advanced Sustainable Observation System) FP6 contract no. RICA-025991 funding the European Lidar Network EARLINET.

- MICINN under the R&D project CTM2006-27154-E/TECNO funding the RSLab participation in the EARLINET-ASOS.

First of all, I would personally like to thank my two thesis advisors, Dr Francesc Rocadenbosch and Dr Ricardo Sanz, for introducing me to the fascinating fields of optical remote sensing and pesticide spray drift, and for their dedication, guidance and constant support during the time spent preparing and writing this thesis.

I would like to give special thanks to Dr Joan Ramon Rosell for the trust placed in me and the marvellous treatment I have received, as well for his constant commitment to new scientific challenges. I am also indebted to Dr Jaume Arnó who not only made possible my integration in the research group GRAP, but who has also given me excellent advice throughout this time. Thanks also are due to Dr Francesc Solanelles, as the conversations we have held have been a great source of new ideas and renewed motivation. I would also like to express my gratitude to the members of GRAP for their help and assistance, especially during the now legendary measurement campaign in Gimenells with the atmospheric lidar.

I thank the members of the Remote Sensing Laboratory of the UPC, and in particular to Professor Adolfo Comerón for all the shared experiences. Thanks similarly go to the members of the Department of Agroforestry Engineering and the Polytechnic School of the UdL for the kindnesses received at all times. My gratitude also goes to the members of the Agroengineering Centre of the Valencia Agrarian Research Institute (IVIA) for their hospitality and collaboration during the field tests conducted in Valencia. I likewise thank the IRTA (Agroalimentary Research and Technology Institute) for kindly allowing me use of the Gimenells field for the field tests with the atmospheric lidar.

Finally, to my parents, to my grandparents and Marta, who have accompanied me on this journey, sharing the joyous moments as well as the more difficult ones. I dedicate this thesis to you.

Eduard Gregorio López

Resum

Els productes fitosanitaris juguen un paper clau en l'agricultura actual donat que contribueixen a millorar el rendiment i la qualitat de la producció, minimitzant els efectes de les males herbes i de les plagues. Tanmateix, l'aplicació de fitosanitaris implica importants riscos sobre la salut humana i animal, així com sobre el medi ambient. Una de les principals vies de contaminació de fitosanitaris és la deriva i per això, un adequat coneixement d'aquest fenomen resulta imprescindible per adoptar millors tècniques de prevenció i d'atenuació. Actualment, la deriva s'estudia utilitzant col·lectors in situ que únicament permeten mostrejar punts concrets dels núvols de fitosanitaris. En aquesta tesi doctoral es proposta utilitzar la tècnica LIDAR (LIght Detection And Ranging) per mesurar la deriva. Es tracta d'una tècnica ben establerta per l'estudi de l'atmosfera i, a diferència dels col·lectors in situ, permet mesurar de forma remota amb elevada resolució temporal i en distància.

Els objectius d'aquesta tesi són (1) dissenyar un sistema lidar específic per la mesura de la deriva i (2) avaluar la capacitat d'aquesta tècnica per quantificar la concentració en els núvols de pesticides. Per a la consecució de l'objectiu (1) s'ha elaborat una metodologia de disseny que pot ser aplicada pel desenvolupament de sistemes lidar per aplicacions fitosanitàries, entre altres. Aquesta metodologia ha estat validada mitjançant la construcció d'un prototipus de ceilòmetre lidar biaxial basat en un díode làser de 905 nm i freqüència de repetició de 5 kHz. El ceilòmetre ha sigut capaç de mesurar blancs topogràfics i capes de núvols. Partint d'aquesta metodologia i atenent a criteris de seguretat ocular, s'han establert els paràmetres de disseny del sistema lidar específic per mesurar la deriva: 1550 nm de longitud d'ona, 25 µJ d'energia per pols, 80 mm d'obertura en recepció, etc. El desenvolupament d'aquest instrument obrirà la porta a nombroses aplicacions impensables amb els col·lectors actuals, com són la realització de mapes de la concentració aèria de fitosanitaris o estimacions del flux de deriva.

Respecte a l'objectiu (2), en aquesta tesi es proposa un model analític quantitatiu que relaciona les mesures lidar de la deriva amb les obtingudes utilitzant col·lectors passius. La relació entre ambdós tipus de sensors també s'ha estudiat mitjançant la realització d'una campanya experimental. Les mesures van mostrar que per a cada assaig existeix una elevada correlació lineal ($R^2 \approx 0.90$) entre el senyal lidar i els col·lectors. Quan s'analitzen a la vegada les mesures obtingudes en tots els assaigs, el nivell de correlació disminueix significativament ($R^2 \approx 0.67$). D'acord amb el model teòric proposat, aquests resultats permeten concloure que els paràmetres meteorològics i d'aplicació que afecten a la deriva únicament es poden considerar invariants al llarg d'un mateix assaig.

Resumen

Los productos fitosanitarios juegan un papel clave en la agricultura actual puesto que contribuyen a mejorar el rendimiento y la calidad de la producción, minimizando los efectos de las malas hierbas y de las plagas. Sin embargo, la aplicación de fitosanitarios implica importantes riesgos sobre la salud humana y animal, así como sobre el medio ambiente. Una de las principales vías de contaminación de fitosanitarios es la deriva y por ello, un adecuado conocimiento de este fenómeno resulta imprescindible para adoptar mejores técnicas de prevención y de atenuación. Actualmente, la deriva se estudia utilizando colectores in situ que únicamente permiten muestrear puntos concretos de las nubes de fitosanitarios. En esta tesis doctoral se propone utilizar la técnica LIDAR (LIght Detection And Ranging) para monitorizar la deriva. Se trata de una técnica bien establecida para el estudio de la atmósfera y, a diferencia de los colectores in situ, permite medir los aerosoles de forma remota con elevada resolución temporal y en distancia.

Los objetivos de esta tesis son (1) diseñar un sistema lidar específico para la medida de la deriva y (2) evaluar la capacidad de esta técnica para cuantificar la concentración en las plumas de pesticidas. Para la consecución del objetivo (1) se ha elaborado una metodología de diseño que puede ser aplicada para el desarrollo sistemas lidar para aplicaciones fitosanitarias, entre otras. Esta metodología ha sido validada mediante la construcción de un prototipo de ceilómetro lidar biaxial basado en un diodo láser de 905 nm y frecuencia de repetición de 5 kHz. El ceilómetro ha sido capaz de medir blancos topográficos y capas nubosas. Partiendo de esta metodología y atendiendo a criterios de seguridad ocular, se han establecido los parámetros de diseño del sistema lidar específico para medir la deriva: 1550 nm de longitud de onda, 25 µJ de energía por pulso, 80 mm de apertura en recepción, etc. El desarrollo de este instrumento abrirá la puerta a numerosas aplicaciones impensables con los colectores actuales, como son la realización de mapas de la concentración aérea de fitosanitarios o estimaciones del flujo de deriva.

Respecto al objetivo (2), en esta tesis se propone un modelo analítico cuantitativo que relaciona las medidas lidar de la deriva con las obtenidas utilizando colectores pasivos. La relación entre ambos tipos de sensores también ha sido estudiada mediante la realización de una campaña experimental. Las medidas mostraron que para cada ensayo existe una elevada correlación lineal ($R^2 \approx 0.90$) entre la señal lidar y los colectores. Cuando se analizan a la vez las medidas obtenidas en todos los ensayos, el nivel de correlación disminuye significativamente ($R^2 \approx 0.67$). De acuerdo con el modelo teórico propuesto, estos resultados permiten concluir que los parámetros meteorológicos y de aplicación que afectan a la deriva únicamente pueden considerarse invariantes a lo largo de un mismo ensayo.

Summary

Phytosanitary products play a key role in modern day agriculture, increasing the yield and the quality of the produce and minimizing the effects of weeds and pests. Nevertheless, application of these products entails significant risks for human, animal and environmental health. One of the main ways in which pesticide contamination occurs is as a result of spray drift and, for this reason, an adequate understanding of this phenomenon is indispensable in order to adopt techniques to prevent it or limit its effects. At the present time, spray drift is usually studied by using *in situ* collectors which only allow sampling of specific points of the pesticide cloud. This doctoral thesis proposes the use of the LIDAR (LIght Detection And Ranging) technique for spray drift monitoring. This is a well-established technique in studies of the atmosphere and, unlike *in situ* collectors, it enables remote measurement of aerosols with high temporal and distance resolution.

The objectives of this thesis are as follows: (1) the design of a lidar system specifically for the remote sensing of pesticide drift and (2) assessment of the capacity of lidar technology to quantify droplet concentration in drift clouds. For the purposes of objective (1), a design methodology was elaborated which can be applied to the development of lidar systems for pesticide applications. This methodology was validated with the construction of a biaxial lidar ceilometer prototype based on a 905 nm laser diode and repetition rate of 5 kHz. The ceilometer has demonstrated its ability to measure topographic targets and cloud layers. Taking this methodology as a starting point and bearing in mind eye safety criteria, the design parameters of a lidar system specifically for drift measurement were established: 1550 nm wavelength, 25 µJ de pulse energy, 80 mm receiving aperture. The development of this instrument will open the doors to numerous applications which are inconceivable with the type of collectors used at the present time. Such possible applications include making maps of the pesticide concentration area and estimations of the spray drift flow.

As for objective (2), a quantitative analytical model is proposed in this thesis which relates the lidar drift measurements with those obtained using passive collectors. The relationship between the two sensor types was also studied by means of an experimental campaign. The measurements showed that for each test there is a high linear correlation ($R^2 \approx 0.90$) between the lidar signal and the collectors. When the measurements obtained in all the tests are analysed at the same time, the level of correlation falls significantly ($R^2 \approx 0.67$). In accordance with the proposed theoretical model, these results allow the conclusion that the application and meteorological parameters which affect spray drift can be considered invariant throughout the same test.

Contents

List of figures

List of tables

List of acronyms

ADC	Analog-to-Digital Converter
AEPLA	*Asociación Empresarial para la protección de las PLAntas*
AERMOD	American Meteorological Society / Environmental Protection Agency Regulatory Model
AES	Atmospheric Environment Service of Canada
ASE	Amplified Spontaneous Emission
AGDISP	AGricultural DISPersal model
AgDRIFT	Agricultural spray DRIFT model
Aglite	Agriculture LIght TEchnology
APD	Avalanche Photo-Diode
ARAL	AES Rapid Acquisition Lidar
BSF	Brilliant Sulphoflavine
CCD	Charge-Coupled Device
CEC	Commission of the European Communities
CFD	Computational Fluid Dynamics
DAMOCLES	*Determinación de Aerosoles por Medidas Obtenidas en Columna (Lidar y Extinción) y Superficie*
DIAL	DIfferential Absorption Lidar
DOAS	Differential Optical Absorption Spectroscopy
DP	Drift Potential
DPSS	Diode-Pumped Solid-State lasers
EARLINET	European Aerosol Research LIdar NETwork
EARLINET-ASOS	EARLINET-Advanced Sustainable Observation System
EEC	European Economic Community
ENOB	Effective Number Of Bits
EPA	US Environmental Protection Agency
FEDER	*Fondo Europeo de DEsarrollo Regional*
FIR	Finite Impulse Response filter
FMS	Frequency Modulated Spectroscopy
FOV	Field Of View
FPS	Filter Particulate Sampler
FSCBG	Forest Service Cramer-Barry-Grim model
FTIR	Fourier Transform InfraRed
GC-MS	Gas Chromatography – Mass Spectrometry
GRAP	UdL Research Group on Precision Agriculture, AgroICT and Agrotechnolgoy
HITRAN	HIgh resolution TRANsmission
HVS	High Volume Sampler

ICNIRP	International Commission on Non-Ionizing Radiation Protection
IEC	International Electrotechnical Commission
IIHR	Iowa Institute of Hydraulic Research
INO	*Institute National d'Optique (Quebec City, Canada)*
IR	InfraRed
IRTA	*Institut de Recerca i Tecnologia Agroalimentàries (Catalunya)*
ISCST3	Industrial Source Complex Short-Term Model v.3
ISO	International Organization for Standardization
IVIA	*Instituto Valenciano de Investigaciones Agrarias*
LASER	Light Amplification by Stimulated Emission of Radiation
LDV	Laser Doppler Velocimeter
LIDAR	LIght Detection And Ranging
MICINN	*MInisterio de CIencia e INNovación (España)*
MPE	Maximum Permissible Exposure
MPLNET	Micro Pulse Lidar NETwork
MRA	Multiple Regression Analysis
MRL	Maximum Residue Limit
NA	Numerical Aperture
NEP	Noise Equivalent Power
NIR	Near-InfraRed
OPC	Optical Particle Counter
OPO	Optical Parametric Oscillator
OSDM	Orchard Spray Drift Model
PBL	Planetay Bounday Layer
PM	Particulate Matter
$PM_{2.5}$	Particulate Matter of 2.5 microns in diameter or smaller
PM_{10}	Particulate Matter of 10 microns in diameter or smaller
PMT	Photo-Multiplier Tube
PRF	Pulse Repetition Frequency
PS-CW	PSeudorandom-Continous Wave
QE	Quantum Efficiency
ROMT	Remote Optical Measurement Technique
RSLab	UPC Remote Sensing Laboratory
RTI	Range-Time Intensity plot
SNR	Signal-to-Noise Ratio
SPALINET	Spanish and Portuguese Aerosol Lidar NETwork
SRA	Simple Regression Analysis
SRL	Scanning Raman Lidar
SRS	Stimulated Raman Scattering
TDLAS	Tunable Diode Laser Absorption Spectroscopy
TIA	TransImpedance Amplifier
TSP	Total Suspended Particulates

UC	University of California
UConn	University of Connecticut
UdL	*Universitat de Lleida*
UHOH	University of HOHenheim
ULV	Ultra Low Volume
UPC	*Universitat Politècnica de Catalunya*
UV	UltraViolet
UW	University of Washington
VIS	Visible
WSP	Water-Sensitive Paper

1

Introduction

This chapter explains the advantages and the risks associated with the application of phytosanitary products, provides details of the corresponding regulations and outlines the problem of drift. A description is then given of the limitations of the methods presently used for the measurement of drift and LIDAR (LIght Detection And Ranging) technology is proposed as a favourable alternative. The application of lidar systems in drift monitoring is however subject to a series of limitations which will be tackled as part of the objectives of this thesis. Finally, a description is given of how this work is organised.

1.1 The application of phytosanitary products

Agriculture has to be able to guarantee a sufficient production of food that is accessible to all and of a quality that is safe to eat. The application of phytosanitary products, more commonly known as pesticides, is an essential part of the process of achieving these objectives. Phytosanitary products are active substances or preparations of active substances which are used to protect plants or vegetable products against harmful organisms or to impede the action of such organisms (CEC, 1991).

The use of phytosanitary products allows improvement and protection of the yield and quality of agricultural production by eliminating or reducing the competition of weeds and pest attacks. These substances ensure a reliable supply of agricultural products and the low-cost availability of quality fruit and vegetables. Increased yield has the added benefit of reducing the demand for land that would otherwise be set aside for food production and enabling it to be used for other purposes (CEC, 2002). An example of how important this sector is can be seen in the figures for the period 2000-2010 with the phytosanitary market in Spain recording annual sales of between 500 and 650 million Euros. In 2009, sales on a worldwide scale amounted to a total of 37,860 million dollars (AEPLA, 2012).

Despite their obvious advantages, pesticides are commonly a toxic product and entail a series of risks and costs in terms of human, animal and environmental well-being. Known as occupational exposure, health risks can be the result of direct exposure to the pesticide on the part of workers who produce, handle, apply the product, etc. There is also a risk of indirect exposure, either as a result of consuming food containing pesticide residues or through what is known as bystander exposure, when the pesticides have travelled beyond the treatment area. The effects of contact with pesticide products are highly varied and depend on the level of toxicity, dose accumulation, etc. They range from simple headaches to irreversible problems such as carcinogenicity or genotoxicity. Special care needs to be taken with the more sensitive groups such as young children or the elderly. The risks for the environment (loss of biodiversity) are caused by spray drift, leaching or spills, all of which provoke the unwanted dispersal of pesticides resulting in the contamination of water and land.

Over the last 20 years a significant number of regulations have been introduced in the phytosanitary sector to minimize these risks, making it one of the most regulated of all sectors (Carlile, 2006). Some of the most important of these regulations are given below:

- Directive 91/414/EEC (CEC, 1991), now Regulation 1107/2009 (EEC, 2009), concerning the marketing of phytosanitary products. This directive provides a list of authorised active substances and harmonizes pesticide assessment and authorization procedures throughout the member states of the EU. Application of this directive has led to a notable reduction in the number of active substances available on the market.

- Directive 2000/60/EEC (CEC, 2000) or water framework directive. This Directive provides a list of the main water pollutants, included among which are the phytosanitary products, for which specific measures must be taken.
- Regulation 396/2005 (EEC, 2005) sets the maximum residue limits (MRLs) of pesticides that can be found in products of animal or vegetable origin for human or animal consumption.
- Directive 2006/118/EEC (CEC, 2006) on groundwater protection. This directive sets maximum pesticide concentration values of 0.1 μg/l for individual pesticides and 0.5 μg/l for total pesticides.

One aspect in which the aforementioned directives and regulations falls short is that hardly any reference is made to the pesticide application stage, a stage which is fundamental when it comes to determining associated risks. In an effort to correct this deficiency, Directive 2009/128/EEC (CEC, 2009) has recently been published concerning the sustainable use of pesticides. Amongst other questions, the directive recognises the negative effects of drift, with the consequent prohibition of aerial pesticide spraying, and the need to apply measures to reduce the pollution risks caused as a result of the phenomenon of drift. The directive also underlines the need to promote research aimed at determining the impact of pesticide use on human health and the environment. A National Action Plan is presently being drawn up on the sustainable use of pesticides. This Action Plan should be approved before the end of the year 2012.

1.2 Spray drift of pesticides and its measurement

1.2.1 The problem: Spray drift of pesticides

It is common practice to apply pesticide products using spraying equipment in the form of water droplets which contain the active ingredients. One of the main problems that result from this practice is that just a fraction of the spray liquid actually reaches its intended target. Part of the spray liquid is lost on falling to the ground (runoff) and another part is scattered in the atmosphere. Spray drift is defined by the standard ISO 22866 (2005) as the quantity of plant protection product that is carried out of the sprayed (treated) area by the action of the air currents during the application process. The drift itself can be in the form of droplets, as dry particles or vapours (Gil and Sinfort, 2005).

Drift is one of the biggest sources of pollution as a result of the application of pesticide products and entails a risk for both human health and the environment (EPA, 1999). Losses as a result of spray drift can amount up to 30-50% of the applied product (Van den Berg et al., 1999). Drift clouds can damage crops close to the treated area, contaminate surface water, reach residential areas, etc. It has even been shown that the pesticides can travel thousands of kilometres via air currents, ending up in areas as remote as the polar regions (Unsworth et al., 1999).

Pesticide drift is a complex phenomenon which is affected by a multitude of factors, of which some of the most important include the characteristics of the spray liquid (volatility and viscosity) (Hofman and Solseng, 2001), the equipment employed and the techniques used in the application (nozzles, droplet size, motion of the spraying vehicle), the weather conditions (wind speed and direction, turbulence and atmospheric stability, temperature, humidity) and the equipment operator (care, attitude, technique). The mechanisms that govern this phenomenon need to be fully understood to enable optimization of the loss prevention and reduction strategies currently in use (Felsot et al., 2011). Drift related data needs to be included for official registration of any new pesticide formulations.

The phenomenon of drift is normally carried out through field tests based on the use of point collectors located close to the area where the treatment is being applied which intercept the generated aerosol plume (ISO 22866). There are some serious drawbacks to this method, of which some of the most important are listed below (Gregorio et al., 2011):

- Information on the pesticide cloud is not time resolved. Conventional collectors only provide integrated parameters over the whole observation period.
- Two- (surface) or three-dimensional (volume) imaging of the plume is not possible. Collectors only display specific sample points of the plume, therefore ignoring the remaining drift volume.
- Their efficiency is largely influenced by the prevailing micro-meteorological conditions during the trial.
- A comparatively large amount of personnel and time resources is required; thus limiting the number of trials that can be carried out in practice.

1.2.2 Laser remote sensing technique

The application of remote sensing lidar techniques to airborne spray drift monitoring can overcome the above limitations. The lidar technique, which is also known as laser radar, benefits from the relatively strong interaction between the electromagnetic radiation at optical wavelengths and the aerosol/molecular atmospheric constituents (Measures, 1992). Laser remote sensing is commonly used in atmospheric studies and a number of lidar networks are currently in use: European Aerosol Research Lidar Network (EARLINET) (Schneider et al., 2000), Micro Pulse Lidar NETwork (MPLNET) (Berkoff et al., 2003), SPALINET (Spanish and Portuguese Aerosol Lidar NETwork) (Sicard et al., 2011), etc.

The advantages of lidar systems in terms of temporal and distance resolution and, more recently, scanning capabilities, led in the early days of this technique to the idea of its possible application in the field of spray drift measurement (Collis, 1968). Since the idea was first mooted, lidar systems have been used in various spray drift studies undertaken in the United States and Canada (Section 2.3.1). However, despite its advanced features, lidar technology has

been unable to establish itself as a commonly used method to measure drift. Its limited application is due to the following factors:

- Cost and complexity of atmospheric lidar systems. Until the mid-90s these instruments were comprised of very powerful laser emission sources (Nd:YAG or ruby laser) and large aperture receiver telescopes operating in combination with photomultiplier tubes (PMTs). This design made the systems complex, heavy, expensive and not particularly suitable for transportation. The development of micro pulse lidar systems (Spinhirne, 1993) and modern lidar ceilometers (Gregorio et al., 2012), both based on the emission of low energy pulses at high repetition rates, opened the door to the development of more affordable and compact lidar systems.

- Eye safety limitations (IEC 60825, 2007). Atmospheric lidar systems are commonly not eye-safe. This aspect is of crucial importance when quasi-horizontal measurements are being taken, as is the case with plume drift monitoring, because of the high risk that the laser beam could strike bystanders. The development in recent years of laser sources at eye-safe wavelengths (~1.5 μm) is leading to the appearance and development of eye-safe lidar systems (Mayor and Spuler, 2004).

- Lidar signal inversion. Due to its complexity, little work has been done on the determination of drift droplet concentration from the lidar measurements. The information provided by the measurements has thus far been of a generally qualitative nature (Section 2.3.1).

The lidar system used during the spray drift measurement campaign as part of the research presented in this thesis is shown in Fig. 1.1.

Fig. 1.1. Elastic lidar system (in the background, Leosphere ALS 300) measuring the drift generated by a hydropneumatic sprayer (behind the trees) treating an apple orchard on 24/09/2009 in Gimenells (Lleida). In the bottom left-hand corner an enlarged view is shown of the emitter/receiver unit. The blue arrow represents a recreation of the emitted UV laser beam.

1.3 Objectives of the thesis

This thesis centres on the study of the application of lidar systems for the remote sensing of pesticide drift in agroforestry environments. The two main objectives of this study are set out below:

Objective 1. *The design of a lidar system specifically for the remote sensing of pesticide drift.* With this purpose in mind, this work will examine the limitations (eye safety, laser and photodetector availability, cost, etc.) which have so far restricted the use of lidar techniques in drift monitoring. The specific tasks that will be carried out for this objective are as follows:

- Review of the currently existing lidar instruments and techniques which show the greatest similarity to the intended design: ceilometers and eye-safe systems.
- Development of a link-budget methodology for the design of lidar systems for pesticide and ceilometer applications.
- Experimental validation of the developed methodology.
- Calculation of the key design parameters.

Objective 2. *Assessment of the capacity of lidar technology to quantify droplet concentration in drift clouds.* The tasks associated with this objective are as follows:

- Review of the different studies in which lidar systems have been used to monitor aerosols from agricultural sources.
- Development of a theoretical model which enables an understanding of the relationship between the lidar signal and the physical properties (such as droplet concentration) of cloud drifts.
- Experimental comparison of drift measurements performed with the lidar systems and those obtained through conventional *in situ* collectors.

1.4 Organization of the thesis

This thesis is organized into six chapters. *Chapter 1* is this introduction, *Chapter 2* summarizes the techniques used for drift measurement, presents the basic aspects of the lidar technique and reviews the studies in which this technique has been applied to monitor aerosols from agricultural sources. *Chapter 3* presents the methodology applied in the design of a lidar ceilometer, the prototype that has been developed and the measurements taken with this instrument. This prototype will be used as a basis for the development of a lidar instrument for drift measurement. *Chapter 4* shows the results of an experimental campaign of drift measurement. An analytical and empirical study is undertaken of the relationship between the measurements obtained through passive collectors and those obtained with an atmospheric lidar

system rented for the tests. *Chapter 5* establishes the key parameters for the design of a lidar system for the purpose of drift measurement. For this, an eye safety study is undertaken as well as simulation of the signal-to-noise (SNR) ratio at different wavelengths. Finally, *Chapter 6* presents the conclusions of the thesis.

2

Airborne spray drift measurement using passive collectors and lidar systems

This chapter is divided into three sections, the first of which reviews the most commonly used pesticide drift measurement methods in the field and in wind tunnels. The principal mathematical models used in drift simulation are also examined. The second section presents the basic fundamentals and main variants of the lidar technique. As was explained in Chapter 1, this work is a study of the lidar system as an alternative to conventional drift measurement techniques. The final section of this chapter acts as a link between the previous two sections in that a bibliographic review is conducted of the different studies in which lidar systems have been applied to monitor pesticide drift or measure aerosols (particulate matter) generated in agricultural and livestock farming.

2.1 Review of conventional spray drift assessment techniques

2.1.1 Field spray drift measurement

The techniques used for the field measurement of airborne spray drift can be classified into three main groups (Gil and Sinfort, 2005): chemical analysis, use of tracers and laser (lidar) measurements. Chemical analyses are based on the extraction and analysis of pesticides present in the air through the use of chromatographic techniques. Gas chromatography-mass spectrometry (GC-MS) is the most widely used analytical technique in the determination of pesticide residues present in the atmosphere (Yusa et al., 2009) and it has also been used in spray drift studies (Briand et al., 2002). Tracers are substances which allow simulation of the transport of airborne pesticides. The most commonly used tracers are visible or fluorescent dyes, metal salts and radioactive isotopes (Cooke and Hislop, 1993). By using tracers instead of pesticides for spray drift studies, costs are reduced and the complexity of the analysis techniques is diminished, although some scientists have argued that tracers alter the properties of the formulation as well as the behaviour of the cloud drift (Riley and Wiesner, 1998). Lidar measurement of spray drift will be reviewed in Section 2.3.

Pesticide or tracer capture for subsequent analysis is carried out using either active (or dynamic) collectors or with passive collectors. These collectors must comply with the following main requirements (Miller, 1993):

- High collector efficiency for small diameter droplets (10-100 μm) at low air speeds (< 1 m/s). The efficiency of a collector is defined as the ratio of the number of droplets striking the collector to the number which would strike it if the streamlines were not deflected (Johnstone et al., 1977).
- A defined sampling area.
- It must be possible to effectively remove the pesticides (or tracers) from the sampling surface.

The main collector types used for airborne drift measurement (that is, the fraction of the drift which remains suspended in the air) will now be reviewed. The measurement of drift deposited on the ground, known as ground sedimentation, is not the concern of this study, though for information purposes it should be mentioned that horizontal-surface collectors (Petri dishes, filter paper, chromatography paper) placed downwind are usually employed for its evaluation (Miller, 2003).

Dynamic air samplers

Dynamic air samplers normally have some electromechanical device which is able to sample a large volume of air. Active collectors allow determination of pesticide (or tracer) concentrations

in the air, as it is possible to relate the sampled air volume with the amount of captured pesticide (Glass, 2006). Examples of dynamic air samplers include (Bui, 1998): volumetric air samplers, cascade impactors, impingers or rotating rod samplers (rotorod).

Volumetric air samplers and cascade impactors are devices whose operation is based on drawing in a controlled flow of air which is then directed through a filtering medium so that the amount of captured spray can subsequently be determined analytically (Miller, 1993). Cascade impactors are aspirated air samplers with several collection stages that enable drift droplet classification by size. These systems enjoy a high sampling efficiency even for small sized droplets. The main drawbacks are their cost and complexity, as well as the need for large amounts of power for the air aspiration.

The Rotorod is a device whose operating principle is based on the high speed rotation of a collection surface using an electric motor. This technique allows the sampling of large air volumes through small collection surfaces. In addition, the efficiency of the collector rises as the relative speed between it and the droplets which strike it increases (Cooper et al., 1996). One of the limitations which should be mentioned is that the air flows generated by the Rotorod can alter the sampled volume of air.

Passive surface collectors

Included in this group are all the static collectors which enable drift evaluation from the impact of droplets on their surface. Due to their simplicity and low cost, this is the most commonly used family of collectors in experimental spray drift studies. Examples of passive collectors include: cards, ribbons, water-sensitive papers or magnesium oxide-coated slides. Standard ISO 22866 (2005), concerning field drift measurement methods, establishes cylindrical surfaces of 2 mm diameter (usually polythene lines) as reference collectors (Fig. 2.1).

The measurements obtained with these collectors can be expressed in units of tracer (or pesticide) mass per unit of surface area. It is possible to relate this value to the amount of spray liquid applied by using the expression (Solanelles, 2009),

$$f_z = \frac{D v_s h_t}{\rho_m q_L}, \tag{2.1}$$

where f_z is the relative value of the drift, D [g/m^2] is the amount of tracer deposited on the surface of the collectors, v_s [m/s] is the operating speed of the sprayer, h_t [m] is the total height of drift measurement (for example, 5 m for vine crops or 10 m for fruit trees), ρ_m [g/l] is the concentration of tracer in the spray liquid and q_L [l/s] is the spray flow rate.

If airborne drift is sampled at different heights, by using for example nylon strings (lines) held up by vertical posts (Fig. 2.1), the relative value in reference to the total height of the post (total drift fraction) is given by Solanelles (2009),

$$F_{drift} = \sum_{i=1}^{N} \frac{f_i}{N_z}, \tag{2.2}$$

Where N_z is the total number of sampled levels.

May and Clifford (1967) studied experimentally the efficiency of various passive collectors (cylinders, spheres, ribbons and discs) and reached the conclusion that their efficiency depends on the Stokes number [dimensionless], given by

$$S_t = \frac{\rho_g U_0 d_p^2}{18\eta l}, \tag{2.3}$$

where ρ_g [kg/m^3] is the droplet density, U_0 [m/s] is the free air stream velocity, d_p [m] is the particle diameter, η [kg/(m·s)] is the air viscosity and l [m] is the width or diameter of the collector. In general, the higher the Stokes number, the higher the efficiency of the collector.

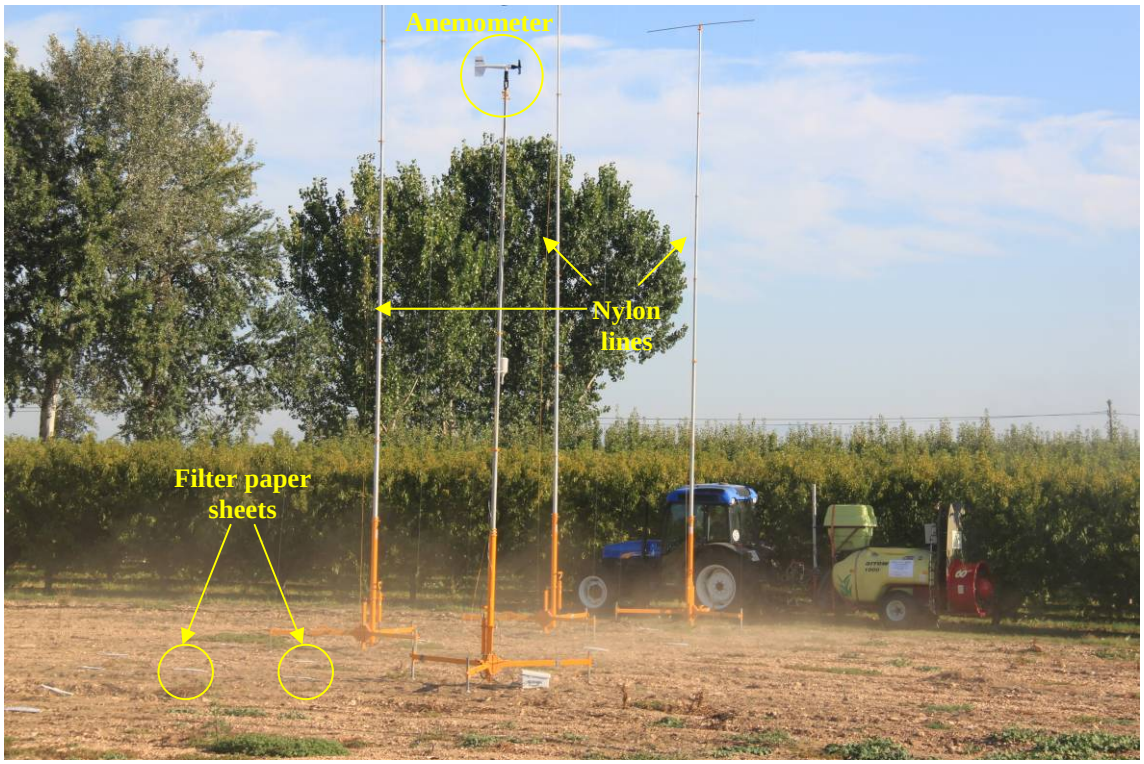

Fig. 2.1. Field measurement of pesticide spray drift. Four posts can be seen, one of which is holding up an anemometer and the other three vertical sampling lines (2 mm diameter nylon line). Several horizontal collectors (filter paper sheets) can be seen on the left of the photograph placed on the ground for monitoring spray drift sedimentation.

Plant species as spray drift indicators

As an alternative to the use of collectors, studies have been made (Marrs et al., 1989) of the possible application of plant species as indicators of herbicide drift. The studies show a good correlation between the response of the plants and the volume of drift.

2.1.2 Wind tunnels and spray drift potential

Unlike field tests, wind tunnels allow drift measurements to be taken in controlled and repeatable conditions. It is a very useful tool for determining and comparing the drift potential (DP) of spraying systems. Despite these advantages, the limited dimensions of the tunnels mean that complete drift studies cannot be performed and such studies must be conducted in the field.

DP measurement in a tunnel is performed by spraying with a static or dynamic nozzle placed inside the tunnel and measuring the resulting drift with collectors, normally of the passive type. As can be seen in Fig. 2.2, the spraying is commonly applied perpendicular to the flow of air that is generated.

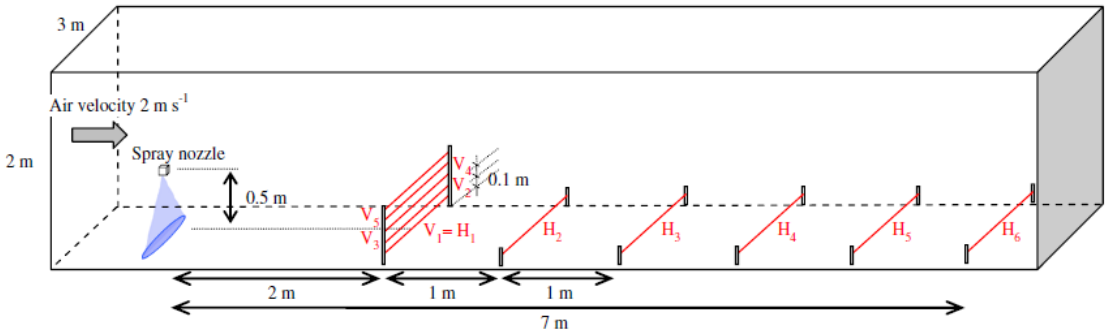

Fig. 2.2. Wind tunnel arrangement for testing of drift risk. H_1 to H_6 comprise an array of horizontal 2 mm diameter polythene lines used for the measurement of fallout deposits. V_1 to V_5 are collector lines for the assessment of airborne spray drift (Nuyttens et al., 2009).

Standard ISO 22856 (2008) establishes general principles for the measurement of spray drift potential in wind tunnels. DP is defined in this standard as the fraction of the spray drift (the percentage of the output of a spray generator) that is displaced downwind as airborne spray. Following this definition, the drift potential (per unit) is calculated as,

$$DP_1 = \sum_{i=1}^{N_x} X_i \cdot \Delta d_i \,, \tag{2.4}$$

where X_i [ml/(ml·m)] is the airborne (V_i, Fig. 2.2) or fallout deposit (H_i, Fig. 2.2) recovered per volume of emitted spray solution and per distance, Δd_i [m] is the distance between the (horizontal or vertical) collectors, and N_x is the number of collectors considered. This expression only takes into account the total drift volume, not its distribution, and represents drift as a fraction of the spray generated at the nozzle outlet.

Another approximation for calculating drift potential is that used by Nuyttens et al. (2009). In this case, the following expression is applied,

$$DP_2 = \sum_{i=1}^{N_v} V_i \cdot h_i \,, \tag{2.5}$$

where V_i [ml/(ml·m)] is the volume of airborne deposit recovered from the line V_i (Fig. 2.2) per volume of emitted spray solution and per distance, h_i [m] is the height above the floor, and N_v

is the number of vertical collectors. This expression takes into account not only the drift volume but also the height at which it occurs, so the greater the height the higher the drift potential.

As an alternative to field and wind tunnel measurements, Balsari et al. (2007) developed a test bench to allow assessment of the drift potential. This bench is comprised of a metal structure inside of which is a series of collectors (filter clothes) provided with sliding covers. During the test, the sprayer passes over the bench with the nozzles in operation. When the machine has made its pass, the protection covers open enabling the collectors to capture the spray droplets which are still suspended in the air and which constitute a potential source of drift. Assays with the test bench have a high level of reproducibility and require less time than field tests.

2.1.3 Drift simulation models

Simulation models are used to predict the behaviour of pesticide clouds, contributing thereby to a safer and more efficient use of these products. The models require information about the distribution of droplet sizes and the meteorological conditions, as well as data about the equipment and application procedure used. They provide graphical or numerical information about the deposition of pesticides on the ground or on the crop, as well as predictions of the airborne drift concentration (Riley and Wiesner, 1998). Simulation models should not be considered as a replacement for experimental tests, but rather as a complementary tool that offers greater understanding of the phenomenon of drift (Gil and Sinfort, 2005). Butler Ellis and Miller (2010) classified these models into four categories: plume dispersion models, computational fluid dynamics models, droplet tracking models and multiple regression models.

Plume dispersion models

These allow estimation, from the application and meteorological conditions, of the concentration of pesticides at a point in space. These models are suitable for simulating far-field drift (0.5-10 km) and the effects of atmospheric stability, but it is difficult to introduce details about the spray source. The most commonly used dispersion model is the Gaussian plume type, whose general form is given by (Turner, 1994),

$$\chi = \frac{Q}{2\pi U \sigma_y \sigma_z} \exp\left[-\frac{1}{2}\frac{y^2}{\sigma_y^2}\right]\left\{\exp\left[-\frac{(H-z)^2}{2\sigma_z^2}\right] + \exp\left[-\frac{(H+z)^2}{2\sigma_z^2}\right]\right\}, \qquad (2.6)$$

where χ [g/m^3] is the air pollutant concentration, Q [g/s] is the pollutant emission rate, U [m/s] is the wind speed at the point of release, σ_y [m] is the lateral standard deviation of the cloud, σ_z [m] is the vertical standard deviation of the cloud, y [m] is the distance perpendicular to the along-wind distance, z [m] is the height above the ground, and H [m] is the release height.

Droplet trajectory models

These models simulate the individual trajectory of the droplets by assuming that they are all separate, spherical and are only subject to the force of gravity and aerodynamic friction (drag). They allow simulation of the effects of the equipment on the spraying and are therefore tools

which are suitable for evaluating the evolution of near-field drift. The Lagrangian equation which governs the movement of the droplets in these models is

$$\frac{d^2 x_d}{dt^2} = \frac{1}{\tau}\left(\overline{U} - \overline{U}_s\right) - g \,, \tag{2.7}$$

where x_d [m] is the droplet position, τ [s] is the time that a droplet needs to adapt to local airflow (relaxation time), $\overline{U}$ [m/s] is the mean air velocity, $\overline{U}_s$ [m/s] is the mean droplet velocity and g [m/s^2] is gravity.

Various models simulating this type of application have been developed over the last 30 years in the United States, where aerial treatment of large areas is highly prevalent. An updated review of these models can be found in Teske et al. (2011). Some of the main aerial spraying models are the Forest Service Cramer-Barry-Grim (FSCBG) model (Dumbauld et al., 1980), the agricultural dispersal (AGDISP) model (Bilanin et al., 1989) and the AgDRIFT model (Teske et al., 2002). AgDRIFT is a Lagrangian model that contains aerial, ground and orchard airblast modules.

Several random-walk models have been developed to model the drift generated by boom sprayers. In these models, the droplet speed at a particular instant is related to the speed at a prior instant but with a random component added as a result of turbulence. By way of example, the equation for the horizontal component of the speed in a random-walk model can be written as (Butler Ellis and Miller, 2010)

$$\Delta U_v = \left(U_h - U_v\right)\left(1 - \alpha_t\right) + \varepsilon \sigma_U \sqrt{1 - \alpha_t^2} \,, \tag{2.8}$$

where ΔU_v is the increment in the horizontal velocity U_v [m/s], U_h [m/s] is the horizontal ambient velocity, $\alpha_t = \exp\left(-\Delta t / T_L\right)$, where Δt [s] is the time step and T_L [s] is the Lagrangian time scale, ε is a Gaussian random number between -1 and 1, and σ_U is the RMS horizontal velocity fluctuation.

Computer fluid dynamics models

Computational fluid dynamics (CFD) codes, like FLUENT© or CFX©, allow simulation of the turbulent flow by resolving the Navier-Stokes equations. For this reason they are commonly used for modelling orchard airblast spraying. One of the drawbacks that should be mentioned is the considerable amount of time that is required to create the model and for its simulation. In addition, this software has to be operated by specialist personnel.

Multiple regression models

Modelling of pesticide drift has occasionally been based on experimental data. The drawback of this approach is that it requires a significant amount of data because of the numerous parameters which have an influence on the phenomenon of drift.

2.2 Review of lidar remote sensing systems

Lidar techniques made their first appearance back in the 1930s, when conventional search lights were used for monitoring the atmosphere (Hulburt, 1937). However, the development of modern lidar systems is closely associated with the invention of the laser by Theodore Maiman (1960). The first lidar system was demonstrated by Smullin and Fiocco (1962), when they focused pulsed optical radiation onto the surface of the moon and detected the echoes. All the basic lidar techniques were developed in the following ten years, some of which are reviewed in this section. At the present time, lidar technology is commonly used to study the atmosphere for meteorological or environmental purposes (Rocadenbosch, 2003a). Typical applications include the detection and quantification of pollutant chemical species, the determination of wind speed and direction, cloud monitoring (ceilometry) (Ludbrook and Winstanley, 1977; Gregorio et al., 2012) and planetary boundary layer (PBL) monitoring (McCormick et al., 1972; Tomás, 2011), etc. Shown in Fig. 2.3 are two examples of atmospheric measurements performed with the lidar system of the UPC.

One of the most significant developments in recent years has been the introduction of new laser devices such as the diode-pumped solid-state (DPSS) lasers, which are more efficient and require less cooling than traditional lamp-pumped Q-switched lasers (Hecht, 2010). This factor, along with the rapid developments in electronics and the application of new modulation techniques, such as the pseudorandom-continuous wave (PS-CW) techniques (Takeuchi et al., 1983; He et al., 2010), is driving the development of more compact and affordable lidar systems. Another tendency which is presently taking place is the use of eye-safe wavelengths ($\lambda > 1.5\,\mu m$), an aspect which will be covered in more detail in Chapter 5.

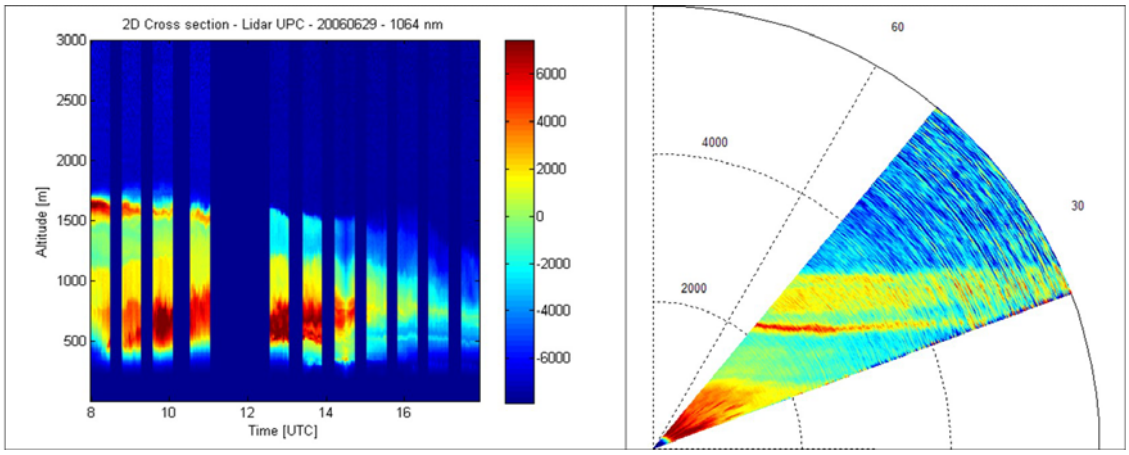

Fig. 2.3. (*left*) Temporal evolution of the atmospheric boundary layer (range-corrected lidar signal) measured with an elastic lidar system at 1064 nm, on 29/06/2006 at Arenosillo (Huelva). (*right*) 2D sweep at 532 nm from 20 to 50º (angular resolution, 1º, total observation time, 1 min.).

Depending on whether the backscattered wavelength is the same as the emitted wavelength, lidar systems are classified into elastic or inelastic types. When the emitter and receiver are located in the same physical place the systems are called monostatic, otherwise they are described as being bistatic. Lidar systems are coaxial when the emitter optical axes are

coincident with the receiver optical axes, otherwise they are known as biaxial. Lidar systems can also be classified according to their application (aerosol lidars, wind lidars, cloud lidars, temperature lidars, etc.).

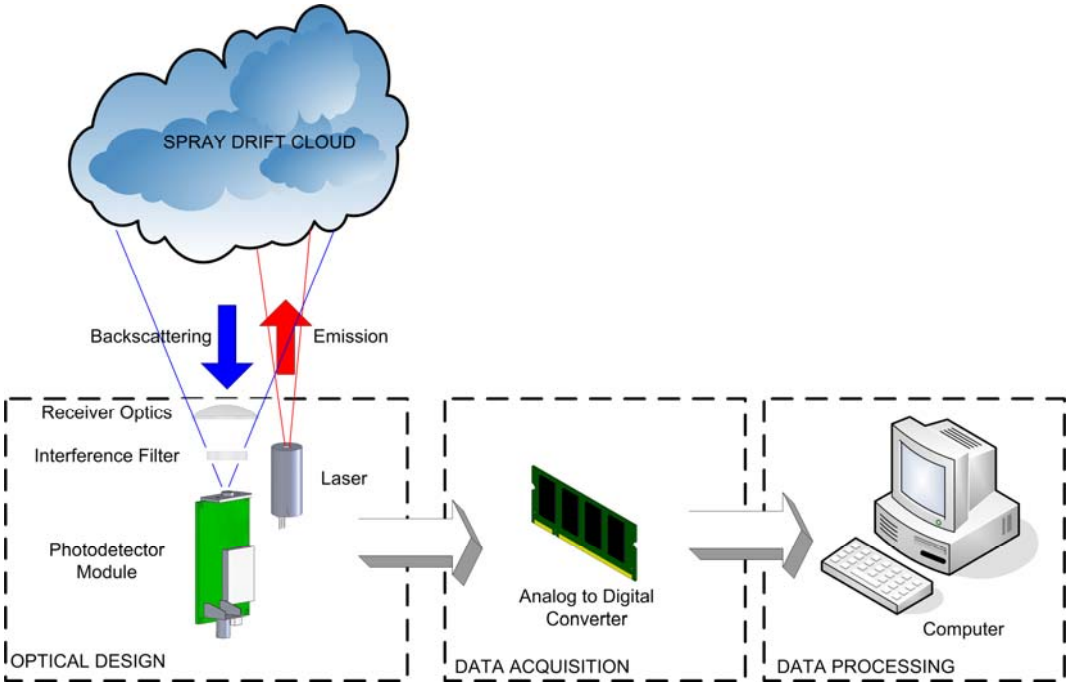

Fig. 2.4. Set-up of a typical lidar system.

2.2.1 Elastic backscatter lidar

The elastic backscatter lidar technique (Fig. 2.4) is the most commonly used technique. Its operating principle is usually based on the emission of an extremely short laser pulse (i.e. in the nanosecond range) and the detection of the backscattered radiation at the same wavelength (elastic interaction). The delay between the emitted pulse and the plume-backscattered received signal (time-of-flight delay) enables computation of the distance to the scattering particles (e.g. aerosols/droplets) (Collis and Russell, 1976) as

$$R = \frac{c \cdot t}{2}, \tag{2.9}$$

where R [m] is the distance along the line of sight from which the returns are received, c [m/s] is the speed of light, and t [s] is the time-of-flight delay. The factor 2 arises because the total distance travelled by the laser pulse takes into account the round-trip travel to the scatterers in suspension.

Lidar equation

Pulsed elastic lidars provide an "optical echo" or received signal consisting of a range-resolved intensity profile as a result of the interaction between the emitted laser pulse and the propagation medium under study (the atmosphere in this case). Under the hypothesis of simple scattering, this intensity profile follows the lidar equation, which expresses the received power as (Collis and Russell, 1976)

$$P(\lambda,R) = P_0\left(\frac{c\tau_l}{2}\right)\beta(\lambda,R)\frac{A_r}{R^2}\exp\left[-2\int_0^R \alpha(\lambda,r)dr\right]\xi(\lambda)\xi(R), \qquad (2.10)$$

where $P(\lambda,R)$ [W] is the received power, λ [nm] is the wavelength, R [m] is the distance, P_0 [W] is the transmitted peak power, c [m/s] is the speed of light, τ_l [s] is the duration of the emitted laser pulse, $\beta(\lambda,R)$ [$m^{-1}sr^{-1}$] is the volumetric backscattering coefficient (equivalently, the backscattering cross-section per volume and solid angle unit) at wavelength λ, A_r [m^2] is the effective area of the receiver telescope (i.e., the "optical antenna"), $\alpha(\lambda,r)$ [m^{-1}] is the volume extinction coefficient (equivalently, atmospheric attenuation), $\xi(\lambda)$ is the spectral transmissivity factor of the emission-reception optical system and $\xi(R)$ is the overlap factor between the emitted laser beam and the receiver field of view. The overlap factor models the fraction of illuminated cross-section in the medium that is "viewed" by the receiving telescope (Measures, 1992).

As in Eq. (2.9), for a lidar system that, in emission, uses laser pulses of duration τ_l and, in reception, a temporal detection window τ_d, the spatial resolution of the system is given by (Collis and Russell, 1976)

$$\Delta R = \frac{c(\tau_l + \tau_d)}{2} \approx \frac{c\tau_d}{2}, \qquad \tau_l << \tau_d. \qquad (2.11)$$

In the case of analogue signal acquisition by using acquisition card sampling at a frequency f_s, $\tau_d = 1/f_s$ in Eq. (2.11), while in the case of photon counting acquisition, τ_d is directly the bin time. Obviously, when the duration of the emitted laser pulses is comparatively much lower than the detection window, $\tau_l << \tau_d$, and Eq. (2.11) reduces to $\Delta R \approx c\tau_d/2$.

Lidar setup

Lidar systems emit at wavelengths ranging from ultraviolet (UV) to near-infrared (NIR). The wavelength is conditioned by the atmospheric transmissivity, its interaction with the target scatterers and by the availability of lasers with appropriate power, pulse length, repetition rate and spectral purity.

In reception, a spectrally selective optical element (in the simplest case, an optical interference filter) selects the optical wavelength of interest from the backscattered radiation (which includes a background component, e.g. solar) and an optoelectronic receiver transduces the received optical power (Eq. (2.10)) into a voltage. The optoelectronic receiver is usually constituted by a photodetector, normally a photomultiplier tube (PMT) for $0.2\ \mu m < \lambda < 0.7\ \mu m$ or an avalanche photodiode (APD) for $\lambda > 0.8\ \mu m$ (Measures, 1992; Rocadenbosch, 2003a), followed by a conditioning stage (e.g. transimpedance amplifier). Next, a signal acquisition system (either analogue or photon-counting based) acquires and digitizes the return signal for disk storage and subsequent processing. By way of example, the emission and reception configurations of the UPC lidar system are shown in Fig. 2.5 (Rocadenbosch et al., 2001).

Fig. 2.5. The UPC 3D-scanning 2+1 elastic-Raman LIDAR system (Rocadenbosch et al., 2001).

(a) The 3D-scanning 2+1 channel elastic-Raman lidar. Emission subsystems: laser (A), Mecalux body (B). Reception subsystems: telescope (C), fibre optics bundle (D) (one end is coupled to the telescope and the other end to the 2+1 polychromator, i.e., the spectrally selective receiving element). Acquisition subsystems: 2-channel acquisition card (Spectrum MI.3011, 2×20 Msps/12 bit) (H), Transient recorder (Licel TR20-160, 250 MHz) (G), Scanning subsystems: U-fork (E), reduction gear (F).

(b) Front view of the portable Scanning Raman Lidar (SRL) showing the Nd:YAG laser (A), the frequency doubler (B) (1064/532 nm simultaneous emission), the polariser assembly (C), the master clock fibre line (D), the receiving telescope (E), the elevation gears and reduction belt (F), the elevation stepping motor and on-axis reducer (G) and the elevation screw (H) for overlap factor adjustment. The laser platform (I) and the telescope (E) are assembled on an aluminium frame. The frame is mounted on a U-fork (J), which provides the azimuth movement by means of the reduction gear (K). The whole scanning structure is mounted on a Mecalux body (B in Fig. 2.5(a)) so that the lidar can rotate some 300º in azimuth and 90º in elevation, this figure being only limited by the strain on the laser cooling hose (J in Fig. 2.5(c)), which is joined to the laser power supply. Emergency stop switches (L).

(c) Rear view of the portable Scanning Raman Lidar (SRL). The figure shows the laser overlap emitter (A) mounted on top of the aluminium platform (B), the micromechanical system for overlap factor (OVF) adjustment in the horizontal direction (i.e., parallel to laser platform (B)) using sliding micrometric slabs, and the main optical receiving parts formed by the receiving telescope (D), a rotary ball-and-socket joint (E) and the optoelectronic front end (F). In the photograph, an elastic receiver (F) is coupled to the rotary joint in place of the eye-piece, hence implementing a single-channel lidar. To implement the 2+1 elastic/Raman configuration, the receiver is replaced with an optical fibre bundle conveying the return radiation to the polychromator.

2.2.2 Other lidar techniques

Raman Lidar

Most of the light that interacts with atmospheric molecules is scattered at the same wavelength (Rayleigh scattering), though a small fraction is scattered inelastically (Raman scattering). The Raman return wavelength λ_R is calculated as

$$\lambda_R = \frac{\lambda_0}{1-\lambda_0 \kappa}, \tag{2.12}$$

where λ_0 is the incident wavelength and κ [cm^{-1}] is the wavenumber shift. Raman lidars capture this inelastic backscattering and are able to measure the concentration of gases, since the

wavenumber shift is a characteristic parameter of each chemical species. The main drawback of these systems is that the intensity of the Raman signal is some three orders of magnitude lower than the elastic return and they therefore commonly require night-time operation. The main parameters estimated by Raman systems are the absolute concentration of atmospheric molecular species, the atmospheric temperature profiles and the water vapour profiles (Rocadenbosch, 2003b).

Differential Absorption Lidar

Differential Absorption Lidar (DIAL) is a lidar technique that uses two or more tuning wavelengths, one of which (λ_{on}) is tuned to a strong gas absorption line, and hence largely absorbed, and another (λ_{off}) de-tuned, which is virtually not absorbed. The species concentration N [m^{-3}] is derived from this differential absorption as (Gimmestad, 2005)

$$N = \frac{1}{2\Delta\sigma\Delta R}\ln\left[\frac{P_{off}(R+\Delta R)}{P_{off}(R)}\frac{P_{on}(R)}{P_{on}(R+\Delta R)}\right], \tag{2.13}$$

where P_{on}[W] is the lidar signal at wavelength λ_{on}, P_{off} [W] is the lidar signal at wavelength λ_{off}, $\Delta\sigma$ [m^2] is the difference between the molecular absorption cross-sections at the two wavelengths and ΔR [m] is the considered range increment.

DIAL is a range-resolved technique when based on pulsed systems and it is normally used to determine the concentration of chemical species in the atmosphere and, indirectly, to perform measurements of temperature and humidity (Schotland, 1964). It is a highly sensitive method as its differential principle tends to cancel out instrumental errors.

Wind Lidar

These instruments enable simultaneous remote measurements to be taken of wind fields (magnitude and direction) with a high distance resolution, unlike weather balloons which can only measure at the height at which they happen to be. Wind lidars can be classified into coherent and incoherent systems (Foreman, 1965).

Coherent detection entails optical mixing of the return signal with that sent by the laser at the same frequency (homodyne detection) or a frequency-offset version of this signal (heterodyne detection). Its operating principle is based on determination of the Doppler shift f_d in the return radiation, a parameter that is related to the radial velocity v_r of the scatterers as

$$f_d = -\frac{2v_r}{\lambda}. \tag{2.14}$$

The main advantage of heterodyne over homodyne systems is that with the former it is possible to know whether the movement is towards or away from the lidar system.

Incoherent detection uses direct-detection or spatial-correlation techniques. Direct-detection systems detect the Doppler shift via high-resolution interferometric techniques. Spatial

correlation techniques study the correlation of airborne particles detected by the lidar. Execution of spatial correlation techniques is limited by the available scanning speed of the lidar system.

Other remote optical measurement spectroscopic techniques

In addition to the lidar techniques presented above there are other remote optical measurement techniques (ROMTs) principally used in the detection of chemical species in the atmosphere. These techniques differ from lidar in that they do not give range-resolved measurements. At the present time, no ROMT technique exists that can be used to detect all species types. Instead of this, there exists a variety of ad-hoc techniques to detect a specified range of species with a particular sensitivity. The main characteristics and most suitable applications of four commonly used ROMT techniques are shown in Table 2.1 for comparison purposes.

	DIAL	**TDLAS**	**DOAS**	**FTIR**
Wavelength	UV-VIS-NIR-MIR	VIS-NIR-MIR	UV-VIS	NIR-MIR
Simult. detection of several species	No	Limited	Yes	Yes (large variety)
Sensitivity	High	High	Medium	Low
Spatial resolution	Yes	No	No	No

Table 2.1. Overview of the main differences between four different remote optical measurement spectroscopic techniques (Gregorio and Rocadenbosch, 2007).

Differential Optical Absorption Spectroscopy (DOAS) (Platt et al., 1979) is a technique used since the late 1970s to determine the species concentration (i.e., column content) integrated along the light path by spectroscopic analysis of the received beam. This is usually carried out in the UV (ultraviolet) or VIS (visible) spectral regions. DOAS instruments are used in both passive and active setups and are usually constituted by a continuous light source (e.g. a Xe-arc lamp in an active setup or the sun in a passive one), a spectrometer and a radiation detector.

Tunable Diode Laser Absorption Spectroscopy (TDLAS) uses the modulated emission of a tunable laser diode to scan over a significant (and technologically feasible) absorption line of the target species (consider HITRAN database (Rotham et al., 1998)). High sensitivities can be achieved, particularly using FMS (Frequency Modulated Spectroscopy).

Fourier Transform Infrared (FTIR) Spectroscopy allows simultaneous detection of multiple species in the IR spectral region. FTIR instruments are usually constituted by an IR source, which emits the transmission light beam through an interferometer. The received signal (i.e. the interferogram) is mathematically manipulated (Fourier Transform) to yield the absorption spectrum.

A comprehensive review of these spectroscopic techniques can found in Sigrist (1993).

2.3 Lidar systems applied in agricultural aerosol studies

Agricultural and livestock farming generate a large amount of emissions into the atmosphere, whether in the form of gases (ammonia (NH_3), methane (CH_4), nitrous oxide (N_2O), etc.) or in the form of aerosols, as pesticides or dust (Yates et al., 2011). Monitoring these emissions is extremely important because of their impact on human and animal health and on the environment in general. In this section, the main studies are reviewed in which lidar technology, principally elastic systems, has been used for the detection of aerosols emitted as a result of agricultural operations. Firstly, the application of lidar systems in spray drift studies is reviewed, followed by lidar-based work centred on the monitoring of particulate matter (PM).

The remote detection of gaseous species from agricultural sources, which is not the concern of this thesis, can be carried out using more complex lidar techniques, such as DIAL or Raman systems, or other ROMTs like TDLAS or FTIR.

2.3.1 Lidar systems applied in spray drift studies

The first works on the use of lidar technology for pesticide spray drift monitoring were conducted during the summers of 1966 and 1967 by the Stanford Research Institute in collaboration with the U.S. Forest Service (Collis, 1968). In these studies two pulsed elastic backscatter lidars were used (Mark I and Mark V) for monitoring the insecticide clouds generated in aerial treatments over several forests. Although these lidars had a very low pulse repetition frequency limited to a few pulses per minute (Table 2.2), first images of the vertical cross-section of the insecticide clouds were obtained from the backscattered lidar intensity.

Another study was carried out by Zalay et al. (1980), which assessed the feasibility of using a mobile atmospheric laser Doppler velocimeter (LDV) for monitoring the spray plume generated in aerial applications. The relative intensities measured by the LDV agreed with the concentration obtained by terrestrial collectors and Kromekote cards. Though LDV systems are much more complex than elastic lidars, unlike the latter the LDV allows determination of the speed of the droplets from the Doppler frequency of the backscattered radiation.

Despite these previous works, it was not until the late 80s, with the development of the ARAL lidar system (Table 2.2) by the Atmospheric Environment Service (AES) of Canada, when elastic-backscatter lidar measurements of spray drifts became more common. The ARAL system (Hoff et al., 1989) is an elastic-backscatter lidar that allows rapid scans of the cross-section of the pesticide plume, obtaining near-real-time maps of relative intensities corresponding to airborne droplet concentration. This instrument was used in various works (Mickle, 1994; Mickle, 1996) to study the dynamics of the aerial emitted pesticides and, more specifically, the influence over them of aircraft wing-tip vortices. Range-resolved lidar data showed the evolution of these vortices, demonstrating that under crosswind conditions, the

upwind vortex rapidly reaches the surface while the downwind vortex remains suspended in the air generating spray drift up to large distances.

Lidar System	Wavelength	Output Energy* (Peak power)	Pulse Length	Pulse Repetition Frequency	Receiving Diameter	Range Resolution
Mark I (Collis, 1968)	694.3 nm	≈240 mJ (10 MW)	24 ns	1-2 pulses per minute	101.6 mm	N/A
Mark V (Collis, 1968)	1060 nm	≈600 mJ (50 MW)	12 ns	1-2 pulses per minute (1966) 12 pulses per minute (1967)	152.6 mm	N/A
ARAL (Hoff et al., 1989)	1064 nm	50 mJ (≈5.6 MW)	9 ns	10 Hz	355.4 mm	N/A
UConn lidar (Stoughton et al., 1997)	1064 nm	125 mJ (≈8.3 MW)	<15 ns	50 Hz	254 mm	2.55 m
UC Davis lidar (Holmén et al., 1998)	1064 nm	100 mJ (≈8.3 MW)	12 ns	50 Hz	254 mm	2.5 m
IIHR lidar (Eichinger et al., 2006)	1064 nm 532 nm	25 mJ (≈2.5 MW)	10 ns	50 Hz	254 mm	1.5 m
UW lidar (Tsai, 2007)	355 nm	8 mJ (≈2 MW)	3-5 ns	10 Hz	N/A	0.6 m
Aglite lidar (Marchant et al., 2009)	1064 nm 532 nm 355 nm	435 µJ 50 µJ 93 µJ	N/A	10 kHz	280 mm	18 m 12 m 12 m
UHOH lidar (Behrendt et al., 2011)	355 nm	300 mJ (60 MW)	5 ns	30 Hz	400 mm	3 m

*Output energy (per pulse). N/A: Not Available.

Table 2.2. Specifications of pulsed elastic backscatter lidar systems used for monitoring aerosols emitted by agricultural sources.

The high temporal and spatial resolution of lidar systems (Table 2.2) makes them an ideal tool to validate theoretical spray-transport models. In this way, researchers from the University of Connecticut (Stoughton et al., 1997) used an elastic backscatter lidar system (Table 2.2) to scan vertical and horizontal planes of pesticide plumes generated in aerial applications over a forest. The comparison of these results with those obtained from theoretical models showed that the lidar is capable of detecting airborne spray drift up to distances of several kilometres. Mickle (1999) reports another comparison between lidar measurements and spray-transport models in an insecticide efficiency study conducted in Florida.

Lidar systems have also been used to assess the influence of atmospheric stability over spray drift movement and dispersal. Miller and Stoughton (2000) made several horizontal and vertical scans of an aerially applied pesticide plume, observing that under stable conditions the cloud spreads more slowly than under unstable conditions. In a recent study, Miller et al. (2012), used lidar to compare the movement of spray plumes from insect foggers and ULV (ultra-low volume) applicators in various stability conditions. It was concluded that spraying covers larger

areas (and is therefore more efficient) when conducted under strong wind conditions. This information is very useful for appropriate time scheduling of spray operations.

Remote quantification of the spray drift plume concentration by means of lidar was carried out by Hiscox et al. (2006) in field trials under stable atmospheric conditions. The authors proposed a new methodology to obtain the absolute concentration of the pesticide cloud from the backscattered lidar signal. Given the application rate of the nozzles and the initial drop size distribution, theoretical models of evaporation and deposition were applied to simulate the temporal evolution of the quantity of product suspended in the atmosphere. Both the lidar-measured backscatter signal and the model-derived product quantity were divided by the volume of the pesticide plume, which in turn was estimated from lidar images. A good correlation in the concentrations estimated from these two independent methods was observed, giving the calibration factor between the lidar measurements and product concentration.

Another methodology used to quantify the lidar signal has recently been developed by Khot et al. (2011). These authors use active (rotorods) and passive (plastic cards) collectors to make point measurements of the spray plume generated by various ground sprayers. A linear correlation ($R^2 \approx 0.77$) was obtained between the backscattered lidar signal and the *in-situ* measurements [nL/cm^2] of the collectors. From this linear relationship, it was possible to quantify the spatial distribution in the straight-line sections of the plume scanned by the lidar system.

Most of the lidar systems used in previous works are not eye-safe and have optomechanical configurations inherited from atmospheric applications making them better adapted for far-field remote sensing and limiting their application in ground spray drift studies. Despite this, some work with lidars has been carried out in fruit orchards (Huddleston et al., 1996). In another study (Miller et al., 2003), lidar measurements allowed the generation of tri-dimensional images of the spray drift plume over an orange orchard, detecting the cloud up to heights of 18 meters above the canopy. It was also possible to visualize the alignment between the plume and the wind direction above the canopy and between the plume and the rows below the canopy top. Moreover, it was shown how, in unstable atmospheric conditions, a higher fraction of pesticide drifts above the vegetation. In the same line, researchers from the University of Washington in Seattle (Tsai, 2007) have used an ultraviolet lidar (Table 2.2) for monitoring the pesticide plume over an apple orchard. The lidar measurements were compared with those obtained with a spray simulation model (OSDM: Orchard Spray Drift Model), revealing significant discrepancies between the two sets of results. This highlights the potential of lidar instruments to contribute to the improvement of these transport models.

Recently in Canada, INO (Institute National d'Optique) has developed a short-range digital lidar (Allard et al., 2007) intended, amongst other applications, for drift measurement. The tests that have been carried out (Fig. 2.6) have shown that the system is capable of close-range

monitoring of spray clouds. Unlike systems used in previous studies, it is an eye-safe instrument although its low range (< 100 m) may limit its practical application in spray drift studies.

Fig. 2.6. INO Short-range lidar placed on the rear end of a hydropneumatic sprayer (Allard et al., 2007).

2.3.2 Lidar monitoring of PM emissions from agricultural sources

Agricultural activities are responsible for 5% of $PM_{2.5}$ emissions (particles less than 2.5 μm in diameter) into the atmosphere and 25% of total PM_{10} emissions (less than 10 μm) (Erisman et al., 2008). Exposure to these particles can entail serious health risks, especially as they have been linked to cardiac and respiratory diseases. As in the case of pesticides, the point samplers which are commonly used for PM measurement are unable to provide a full view of the plume generated by the agricultural source. The studies that have been undertaken over the last 15 years using lidar systems have shown that these instruments allow monitoring of PM clouds with high temporal and distance resolution. The main difficulty lies in calibrating the backscattered lidar signal in order to quantify the numerical or mass concentration of PM.

Holmén et al. (1998) carried out the first work in which a backscatter elastic lidar system was used (Table 2.2) to study PM_{10} emissions from land preparation operations. The tests were performed during the harvesting and disk harrowing operations at a wheat field located in California's San Joaquin Valley. The lidar measurements were compared with those obtained from various point samplers. It was shown that the point collectors may or may not be able to detect the aerosol flow depending on where they are positioned. It was concluded in this study that future monitoring techniques should combine lidar systems with strategically positioned point collectors in order to obtain PM samples for subsequent chemical analysis. In two later studies (Holmén et al., 2001a,b), the same authors used the elastic lidar together with a series of point collectors to determine the vertical profile of concentrations and the height of the PM_{10} plumes generated in disking, ripping, root cutting and listing operations .

In 2005, a measurement campaign was conducted of the dust plumes emitted during disking and harvesting operations at a cotton field located in New Mexico (Hiscox et al., 2008; Holmén et al., 2008). The University of Connecticut's elastic backscatter lidar was used in this campaign

(Table 2.2) as well as several optical real-time particulate samplers. As can be seen in Fig. 2.7a, the lidar measurements (total backscatter) and those obtained with the *in situ* collectors (concentration, μg/m^3) present a high correlation ($R^2 = 0.79$) for total suspended particulates (TSP) and a moderate correlation ($R^2 = 0.61$) for PM_{10}. The lidar system was calibrated based on correlation with the TSP, with estimation of the aerial dust concentrations. The lidar was also used to study plume dispersal and its height and motion under different meteorological conditions (unstable, neutral and stable). Scanning was also performed at different heights, with the combination of the resulting data providing a 3D image of the dust plume (Fig. 2.7b).

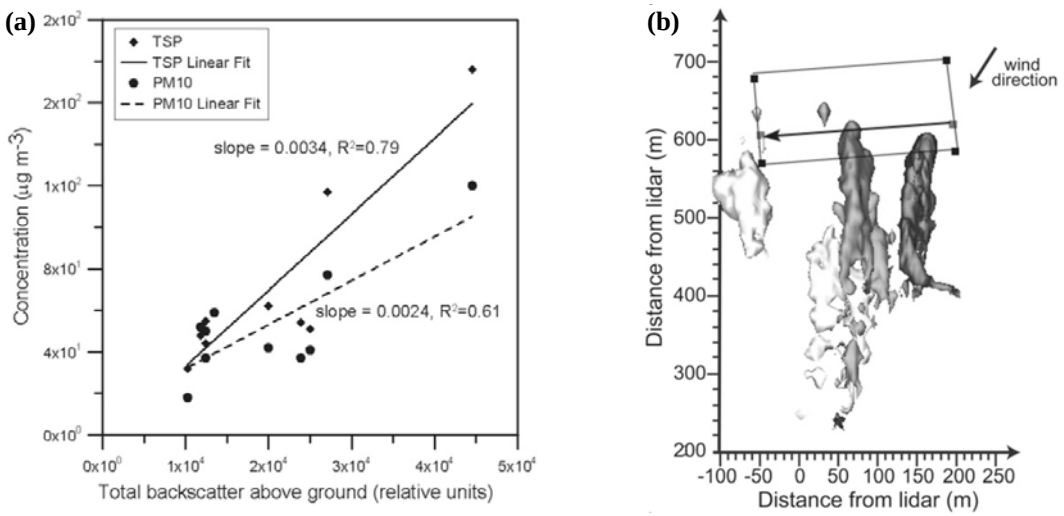

Fig. 2.7. (a) TSP and PM_{10} at the ground vs total lidar backscatter approximately 3 m above the ground. (b) Three-dimensional rendering of combined lidar scans (Hiscox et al., 2008).

Lidar measurements have also been used to validate dust plume dispersal models from agricultural field preparation operations. Wang et al. (2008; 2009) developed a random-walk (Lagrangian) model to simulate the temporal and spatial evolution of the concentration (3D) of PM_{10} plumes. One of the main improvements of this model is that it allows simulation of sources in motion (e.g. tractor). The concentrations obtained with the model were compared with the lidar measurements taken during the above mentioned disking operations in New Mexico. A correlation of $R^2 = 0.78$ was obtained between the predictions of the model and the lidar measurements. In general, the accuracy of the model falls as the height or averaging time increases.

Livestock housing is another important source of emissions of particulate matter (Cambra-López et al., 2010). In addition, the tendency to increase the number of animals, for reasons of economy of scale, means that more and more emissions are being generated from this source. In this context, a pioneering study was undertaken by Hartung et al. (1997) in which a UV lidar system was used along with a high volume sampler (HVS) to monitor the aerosol plume emitted by a pig farm. Another study in a swine production facility was carried out by Eichinger et al. (2006) using an elastic lidar system (Table 2.2). In this work it was shown that, contrary to common belief, the plumes emitted in the farms are not continuous, do not present a Gaussian profile and can spread vertically as well as horizontally. Studies were also carried out at a pig

farm in the north of Germany (Behrendt et al., 2011; Valdebenito et al., 2011) using the aerosol scanning lidar system of the University of Hohenheim (Table 2.2). In these studies, lidar data inversion was used to obtain the values of the backscatter coefficient corresponding to the emitted aerosol plume. These values were used to evaluate the simulations performed with an atmosphere-microphysics-chemistry model.

In the last five years, development of the Aglite (AGriculture LIght TEchnology) lidar system by the Space Dynamics Laboratory (Utah State University) has entailed a significant advance in the characterisation of aerosols from agricultural sources (Marchant et al., 2009). The Aglite Lidar is a portable scanning lidar that uses a high-repetition rate low-pulse energy YAG laser with photon-counting detection (Table 2.2). Unlike the systems used in the studies thus far mentioned, this lidar emits at three wavelengths (1064, 532 and 355 nm) using doubling and tripling crystals. The availability of three channels enables information to be obtained about the physical characteristics of the monitored aerosols.

As can be seen in Fig. 2.8, the Aglite system calculates the mass concentration [$\mu g/m^3$] of the plume by merging the data from the *in situ* sensors (optical particle counters (OPCs) and filter particulate samplers (FPS)), with the lidar measurements (Zavyalov et al., 2009). The *in situ* measurements are used as boundary conditions to invert the lidar signal applying the Klett algorithm (1985). The *in situ* data are also used to calculate a calibration factor, called a mass conversion factor, to convert the backscatter coefficient β [$sr^{-1}m^{-1}$] to mass concentration.

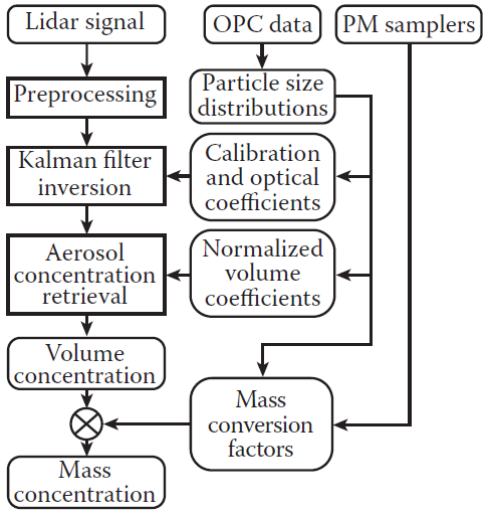

Fig. 2.8. Aglite retrieval algorithm to convert lidar signal return to aerosol mass concentration (Zavyalov et al., 2009).

In Marchant et al. (2010), a new iterative least squares method was developed to determine the concentration of agricultural aerosols measured with the Aglite system. This method has advantages over the Klett method in that it allows the generation of stable solutions at ranges beyond the reference point and at low SNR values.

The Aglite system has been experimentally used (Bingham et al., 2009; Marchant et al., 2009; Zavyalov et al., 2009; Wojcik et al., 2012) to measure PM concentrations and fluxes [g/s] generated by a swine feeding facility, a cotton gin and during almond harvesting. To obtain the emission flux in each case, the lidar scanned the concentration field upwind and downwind of the target area of study (Fig. 2.9), simultaneously measuring the wind speed with anemometers.

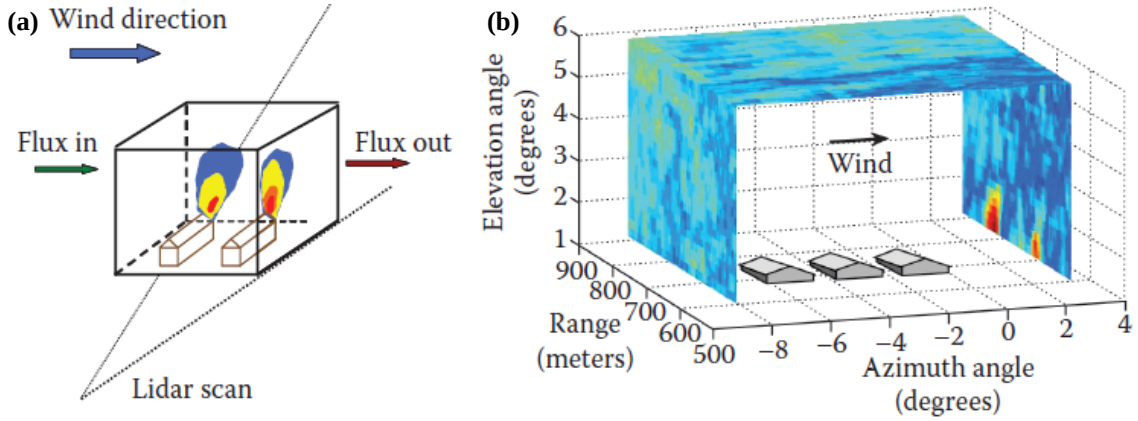

Fig. 2.9. (a) Scheme for using lidar to generate particulate fluxes. (b) Example of a "staple" lidar scan over the facility showing aerosol concentrations on the three sides (Bingham et al., 2012).

The flux is calculated by multiplying the area integrated mass concentration difference by the wind speed during the scan as

$$F_x = \int_r \int_h \bar{v}_\perp(r,h)\left[C_D(r,h) - C_{\bar{U}}\right] dr dh\,, \tag{2.15}$$

where $\bar{v}_\perp$ [m/s] is the average wind speed component, the direction of which defines the long axis of the box, $C_D - C_{\bar{U}}$ [g/m^3] forms the mass concentration difference upwind and downwind, integrated over the range r (width) and height h of the exit plume.

The concentration and flux measurements obtained with the Aglite system have been checked against various aerosol dispersal models. Bingham et al. (2009) compared the Aglite measurements with the simulations generated by the Industrial Source Complex Short-Term Model v.3 (ISCST3). In a subsequent campaign, Marchant et al. (2011) used the Aglite system at a cattle farm, estimating the emission rates per day and animal of $PM_{2.5}$, PM_{10} and TSP (total suspended particles). These values were compared with the values simulated by the Meteorological Society and US Environmental Protection Agency Regulatory Model (AERMOD). Significant differences were observed between the results obtained from the two methods, which was attributed to the fact that the model does not simulate high plumes very well, while the lidar did not measure the clouds at a low height. The Aglite system has also been used by Wen et al. (2011) to estimate PM emission rates when applying various ploughing methods and under different weather conditions.

2.4 Concluding remarks

Most airborne spray drift measurements carried out today are still made using collectors and tracers. The use of this type of methodology is costly and time-consuming. Moreover, because of the extensive variety of crop and meteorological conditions it is difficult to make an accurate assessment of the real spray drift hazard associated with each application technique. As a result, there has been a growing interest in the search for alternative methods which can be used either

in the laboratory, with wind tunnels, or in the field. The use of optical systems like the lidar has emerged as one of the most feasible options.

This review shows that lidar systems allow real-time monitoring of airborne spray drift obtaining range-resolved images of the spray plume while requiring fewer personnel and consuming less time. Considering these obvious advantages, the use of lidar systems in future airborne spray drift studies should be promoted and correlation relationships between results from conventional sampling techniques and spray transport models should be investigated.

However, despite the advantages of lidar systems for airborne spray drift monitoring, they have thus far been used in only a limited way. This is because currently available lidar systems inherit their architecture design from atmospheric monitoring applications (high energy, low pulse-repetition-frequency systems), which make them expensive and require trained personnel for their operation. In addition, many of these instruments are not eye-safe, preventing their practical application particularly in ground spray drift studies (quasi-horizontal sounding). Recent developments over the last few years in relation to efficient low-energy high-PRF lasers (typically 1-100 μJ and 1-10 kHz repetition rates) and reasonably priced photodetectors in the eye-safe bands (1.5 and 2.1 μm) will allow the development of affordable lidars which are better adapted to airborne spray drift monitoring with high spatial and temporal resolutions.

3

Parameter design of a biaxial lidar ceilometer

This chapter presents system parameter design and related opto-mechanical engineering of a 905-nm diode-laser lidar ceilometer prototype for cloud-height monitoring. In turn, this provides the development grounds of an ad-hoc microlidar for spray drift monitoring in Chapter 5. Both systems are eye-safe, low-pulse energy, and have biaxial configuration.

The chapter starts with a brief review of the state-of the-art ceilometer technology; acceptable parameter ranges are identified for the key system parts. Parameter tuning is achieved by imposing goal criteria on the simulated signal-to-noise ratio (SNR) and laser-telescope overlap factor. The system is based on a low-cost pulsed semiconductor laser, low-cost Fresnel-lens telescope, a low-NEP avalanche photodiode opto-electronic receiver, and collimating/focusing adjustable parts. Finally, preliminary test measurements are presented.

3.1 Introduction

Lidar technology based on ceilometers enable high resolution (distance and time) determination of cloud base heights and are commonly used in airports to ensure air traffic safety (Rocadenbosch, 2003a), as well as in weather and scientific stations. Several commercial models are presently available in the market. Their operating principle normally entails the emission of laser pulses at high repetition-frequency rates and with low energy content, obtaining the signal to-noise ratios required for data inversion and/or real-time data processing through pulse averaging (Ludbrook and Winstanley, 1977). This configuration has enabled the development of small-sized and eye-safe lidar ceilometers, which cost less than conventional lidar systems. Despite these achievements, major shortcomings are presented in the scientific literature concerning the methodologies applied to the design of these instruments. Most of the work is based on the final specifications of the ceilometers, while the finer details of the opto-mechanical solutions that have been implemented are commonly not discussed as they may well involve commercial/industrial interests and/or patented results.

The prototype developed is conceived as an affordable and eye-safe instrument, capable of determining rain-cloud heights, and operates as a cooperative sensor for storm forecasting. A maximum range of 7.5 km is considered sufficient for these purposes. Similar detection ranges can be found in commercial ceilometers (All Weather, 2005 & 2007; Eliason Engineering, 2012; Jenoptik, 2012; Vaisala, 1999, 2004 & 2010]). A biaxial configuration is chosen because of its greater simplicity and since the aim is not the detection of surface fogs.

The chapter is largely design and methodologically oriented with special emphasis on the design and prototype engineering of both the optical and mechanical aspects concerning the ceilometer emission and receiving subsystems. Step-by-step applied-design methodology is presented. Section 3.2 presents the most relevant design parameters of a lidar ceilometer. Section 3.3 presents the simulations carried out to assess the prototype design parameters. Section 3.4 is devoted to the main core of the prototype design and covers both the emission and receiving subsystems. In Sect. 3.5, the constructed prototype and the first-test measurements are presented. Finally, Sect. 3.6 gives concluding remarks.

3.2 State-of-the-art: design parameters

In what follows the main variables that must be taken into account in order to design a lidar ceilometer with the desired performance are presented. To that aim the section is divided into three parts. In the first two parts, the design parameters of the emission and receiver subsystems are respectively discussed. In the third, two possible ceilometer configurations are discussed.

3.2.1 Emission subsystem

Commercial lidar ceilometers usually use pulsed laser diodes, with wavelengths of around 900 nm and repetition frequencies of a few kHz, as light sources. Main advantages are the low cost of laser diodes, their ease of operation, and the extensive availability of photodetectors at these wavelengths. The duration of the laser pulses is usually between $\tau_l = 10$ and 150 ns (Ludbrook and Winstanley, 1977; Streicher et al., 2004), and the sampling frequencies (f_s), between 20 and 100 MSps (10^6 samples per second) with equivalent detection time $\tau_d = 1/f_s$, all of which enables spatial resolutions (Eq. 2.11), between 3 and 30 m (MTECH, 2012; Kärkkäinen et al., 1997).

As mentioned above, while the low-cost laser diodes are the predominant solution in commercial systems, it should also be noted the development of some instruments based on solid-state lasers, including the Jenoptik CHM15k model (Jenoptik, 2012), whose transmission source is a 1064 nm Nd:YAG laser.

Emission wavelength, λ

As for eye-safe wavelengths (~1.5 μm in (IEC 60825-1:2007])), some experimental prototypes have been designed (Gaumet et al., 1998) and even some commercial models (Degreane, 2012) based on Erbium-doped glass laser. While at 1.5 μm it is possible to significantly increase the energy emitted and meet eye safety requirements, its application is limited because of the scant availability of photodetectors, generally InGaAs-APD with very small diameters ($d_D \leq 200$ μm) and low detectivities (Kovalev and Eichinger, 2004). For these reasons the preferred option is a 905 nm design.

Pulse energy characteristics

Since commercial lidar ceilometers normally use laser diodes of high pulse repetition frequency (PRF) with energies in the interval between 1 and 10 μJ (Ludbrook and Winstanley, 1977; Münkel et al., 2002), eye safety at 900-nm wavelength is ensured by expanding the laser beam with a consequent reduction of radiant exposure ($J \cdot m^{-2}$). The expansion optics also enables minimization of laser beam divergence, which in laser diodes has an elliptical shape and values of the order of 175×525 milliradians, to a few milliradians.

3.2.2 Receiving subsystem

A classical ceilometer receiving subsystem consists of three main elements:

- Optics to capture and focus the backscattered lidar signal, where the primary lens (system aperture) usually has a diameter (d_0), ranging between 100 and 200 mm (Ludbrook and Winstanley, 1977; Vaisala, 2004).
- Interference filter (in the nm range) to select the radiation at the wavelength of interest.
- Photodetector module responsible for transducing the light into an electrical signal. At 900 nm this usually consists of the combination of a silicon avalanche photodiode (Si-APD) and

a transimpedance amplifier (TIA). Using Si-APDs, intrinsic responsivities (R_{io}) between 0.30 and 0.62 A/W can be obtained, at a much lower cost than photomultiplier tubes (PMT), corresponding to quantum efficiencies (QE) between 40 and 85 % (Excelitas, 2011), with gains (M) commonly ranging between 30 and 250. The noise equivalent power of the module (NEP_m) is proportional to the square root of the photosensitive detector area (diameters between 0.25 and 5 mm) and to the bandwidth B_N of the photodetector module (Kovalev and Eichinger, 2004). The NEP_m, commonly takes values from 20 to 700 $\mathrm{fW}/\sqrt{\mathrm{Hz}}$ (Hamamatsu, 2012).

- Diaphragm aperture working as a spatial filter, to achieve both a large field of view and a high background-rejection ratio (Abramochkin and Tikhomirov, 1999; Agishev and Comeron, 2002; Freudenthaler, 2003).

Field of View, FOV

The field of view must be larger than the laser beam divergence so that the atmospheric cross-section illuminated by the laser is fully seen within the receiver FOV. The half-angle FOV in commercial ceilometers is usually between 0.5 and 5 mrad (half-angle). For final specification of this parameter account should be taken of the fact that narrow fields of view reduce background radiation and the effects of multiple scattering, while for higher values full overlap is achieved at low elevations and alignment between the emission and reception axes of the system is easier.

3.2.3 Ceilometer configuration

When conceptualizing a lidar ceilometer, one of the key parameters to assess its detection capacity is the measurement range or distance interval in which the clouds can be detected. Two ceilometer "families" can be distinguished in terms of their maximum range:

- Systems, such as the All Weather, Inc. model 8339 (All Weather, 2005), the Eliasson Engineering CBME80 model (Eliasson, 2012) or the Vaisala CL31 ceilometer (Vaisala, 2004), which measure up to an approximate altitude of 7.5 km.
- Specially designed systems for high-altitude cirrus detection with a maximum range between 12 and 15 km. Such systems include the All Weather, Inc. model 8340 (All Weather, 2007), the Jenoptik CHM15k model (Jenoptik, 2012) or the Vaisala CL51 (Vaisala, 2010).

The minimum sounding range of the instrument depends fundamentally on whether it has a coaxial or biaxial configuration. Coaxial ceilometers have a single emission-reception axis with the laser beam always within the FOV of the telescope. This enables detection from elevations of virtually zero and is extremely useful for monitoring low altitude phenomena. However, a coaxial configuration has the drawback of internal optical cross talk, which means electronic compensation systems have to be incorporated as in Vaisala's CT25k model (Vaisala, 1999), or the development of ad-hoc optical solutions as in the Vaisala CL31 (Vaisala, 2004), which

incorporates a special lens with an outer area responsible for focussing backscattered light onto the photoreceiver and a central area responsible for laser beam collimation. In contrast, one of the characteristic features of biaxial ceilometers is their different emission and reception optical axes. Biaxial configuration avoids the problem of optical cross talk but is optically not as efficient as the coaxial solution. As it is shown in Fig. 3.1, the overlap function depends on the receiving FOV ϕ, diameter of the telescope's objective lens (or mirror) d_0, divergence of the emitted laser beam θ, laser-output aperture W_0, and on the distance d_i and tilt angle δ between the two axes (Measures, 1992).

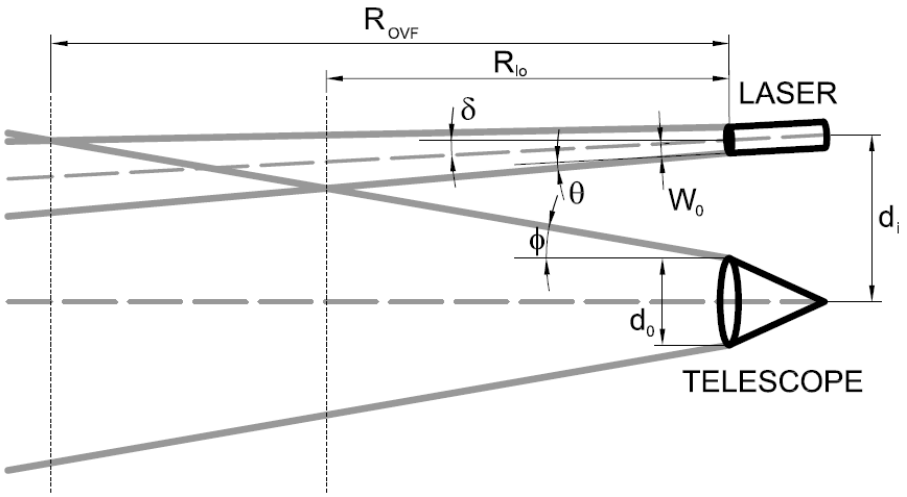

Fig. 3.1. Biaxial configuration scheme for a lidar ceilometer. R_{io} stands for the initial range at which partial overlap between the laser beam and the telescope's FOV begins. R_{OVF} is the starting range of full overlap.

The state-of-the-art technological values discussed so far are summarized in Table 3.1.

3.3 Performance assessment

In this section, a link-budget simulation has been developed to tune the ceilometer design parameters within the design intervals of Table 3.1. The simplified Mie/Rayleigh atmospheric model of Fig. 3.2, corresponding to a wavelength of 905 nm, has been used in the simulations, its main limitation being the use of a constant molecular background. This model assumes "standard-clear" atmospheric conditions (visibility equal to 23.5 km as in (Measures, 1992)) inside the boundary layer (0-3 km height). At this point, note that Fig. 3.2 represents total optoatmospheric parameters defined as

$$\alpha^{tot}(R) = \alpha^{aer}(R) + \alpha^{mol}(R), \tag{3.1}$$

$$\beta^{tot}(R) = \beta^{aer}(R) + \beta^{mol}(R), \tag{3.2}$$

where α and β stand respectively for extinction and backscatter, and superscripts *tot*, *aer* and *mol* are reminders of *total*, *aerosol* and *molecular* components.

PERFORMANCE		Max. detection range, R_{max}	7500 m
		Range resolution, ΔR	<30 m
EMITTER	Laser	Type	High repetition rate laser diode
		Wavelength, λ	905 nm
		Pulse energy, E_0	1-10 μJ
		Pulse duration, τ_l	10-150 ns
RECEIVER	Photodetector	Type	Silicon avalanche photodiode
		Intrinsic responsivity, R_{io}	0.30-0.62 A/W (QE : 40-85%)
		Gain, M	30-250
		Photosensitive diameter, d_D	0.25-5 mm
		Noise equivalent power, NEP_m	20-700 fW/$\sqrt{\text{Hz}}$
	Receiving optics	Primary lens diameter, d_0	100-200 mm
		Field of view, ϕ	1-5 mrad (half-angle)

Table 3.1. Intervals of acceptable values for the main ceilometer design parameters based on a state-of-the-art study.

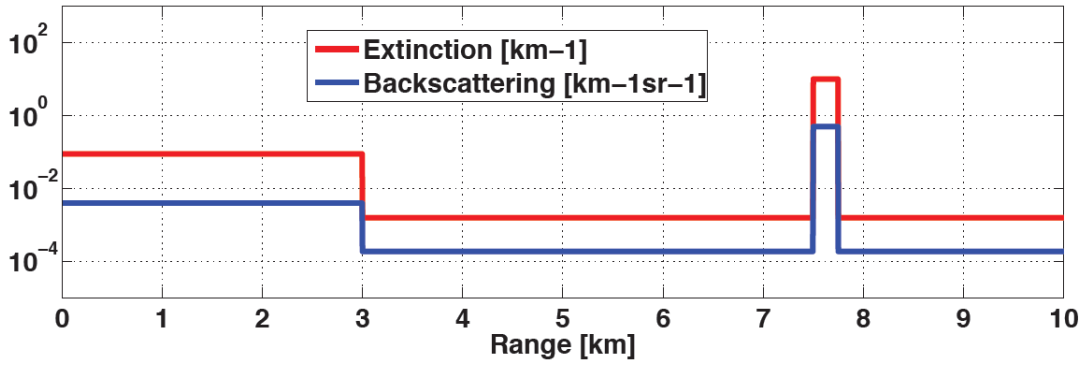

Fig. 3.2. Simplified opto-atmospheric model for the total extinction (*aerosol* + *molecular* components) and total backscatter parameters at a wavelength of 905 nm. The model (Measures, 1992; Collis and Russell, 1976) uses a "standard-clear" homogeneous atmosphere ($\alpha^{aer} = 0.087$ km^{-1}, $\beta^{aer} = 3.8\times10^{-3}$ km^{-1}sr^{-1}) inside the boundary layer (0-3 km height) and locates a light-water cloud ($\alpha^{cloud} = 10$ km^{-1}, $\beta^{cloud} = 0.5$ km^{-1}sr^{-1}) layer in the 7.5-7.75 km range. A constant molecular background ($\alpha^{mol} = 1.6\times10^{-3}$ km^{-1}, $\beta^{mol} = 1.9\times10^{-4}$ km^{-1}sr^{-1}) is also used.

3.3.1 Signal-to-Noise Ratio (SNR) Simulations

The expression of the signal-to-noise ratio for a typical APD and TIA combination is given by (Rocadenbosch et al., 1998)

$$SNR(R) = \frac{R_{io} M G_T \xi_0 P(R) \xi(R)}{\left[\sigma^2_{sh,s}(R) + \sigma^2_{sh,d} + \sigma^2_{th}\right]^{1/2} B_N^{1/2}}, \tag{3.3}$$

in units of [V/V], where R_{io} [A/W] is the APD current intrinsic responsivity, M is the APD multiplication factor, G_T [Ω] is the receiver transimpedance gain, ξ_0 is the total transmission

factor of the receiving optics at the design wavelength λ_0 ($\xi_0 = \xi(\lambda_0)$), $P(R)$ [W] is the backscattered signal power, $\xi(R)$ is the overlap factor, $\sigma^2_{sh,s}$, $\sigma^2_{sh,d}$ and σ^2_{th} are the photo-induced shot noise, the dark-shot noise and the thermal noise, respectively [V^2Hz^{-1}] and B_N [Hz] is the equivalent noise bandwidth at reception.

These noise spectral densities are computed as follows (Measures, 1992; Rocadenbosch, 1998),

$$\sigma^2_{sh,s}(R) = 2qG_T^2 FM^2 R_{io}\left(P(R)\xi(R) + P_{back}\right)\xi_0 , \tag{3.4}$$

$$\sigma^2_{sh,d} = 2qG_T^2\left(I_{ds} + FM^2 I_{db}\right), \tag{3.5}$$

$$\sigma^2_{th} = i_T^2 G_T^2 , \tag{3.6}$$

all in units of [V^2Hz^{-1}], where F is the excess noise factor, P_{back} [W] is the background radiance power, I_{ds} [A] is the APD surface dark current, I_{db} [A] is the APD bulk dark current, i_T [$A/\sqrt{Hz}$] is the amplifier input noise current density and q [C] is the electron charge. The other variables have already been presented.

The return power component is computed from the well-known single-scattering form of the elastic lidar equation (Eq. 2.10) that is rewritten as

$$P(R) = K_s U_s(R) , \tag{3.7}$$

with

$$U_s(R) = \frac{\beta(R)}{R^2}\exp\left[-2\int_0^R \alpha(r)dr\right], \tag{3.8}$$

where $\beta(R)$ [$m^{-1}sr^{-1}$] is the total atmospheric volume backscattering coefficient, R [m] is the range, $\alpha(r)$ [m^{-1}] is the total atmospheric volume extinction coefficient. The system constant K_s [$W{\cdot}m^3$] is a key parameter for determining the performance of a lidar system and allowing easy comparison with other instruments, and is given by

$$K_s = \frac{E_0 A_r c}{2} , \tag{3.9}$$

where E_0 [J] is the energy emitted per laser pulse, A_r [m^2] is the effective receiver area and c [ms^{-1}] the speed of light.

The background-radiance power component accepted by the receiving optics is computed as (Measures, 1992)

$$P_{back} = L_b K_b , \tag{3.10}$$

where L_b [$W{\cdot}m^{-2}{\cdot}nm^{-1}{\cdot}sr^{-1}$] is the sky background spectral radiance and K_b [$m^2{\cdot}nm{\cdot}sr$] is defined here as the background-radiance system constant given by

$$K_b = A_r \Omega_r \Delta\lambda , \tag{3.11}$$

where Ω_r [sr] is the receiver-system acceptance solid angle ($\Omega_r = \pi \sin^2(\phi) \approx \pi\phi^2$ (i.e. $\phi << 0$), (Möller, 1988)) and $\Delta\lambda$ [nm] is the interference filter bandwidth.

The noise equivalent power of the photoreceiver module is computed as (Hamamatsu,1998)

$$NEP_m = \frac{\left(\sigma_{sh,d}^2 + \sigma_{th}^2\right)^{1/2}}{R_{io} M G_T}, \tag{3.12}$$

in units of [$W/\sqrt{Hz}$], where all the variables have already been presented.

Substituting Eqs. (3.4), (3.7), (3.10) and (3.12) into Eq. (3.3) and operating, the following expression is obtained for the *SNR*,

$$SNR(R) = \frac{\xi_0 K_s U_s(R)}{\left[\frac{2qF}{R_{io}}\left(K_s U_s(R) + K_b L_b\right)\xi_0 + NEP_m^2\right]^{1/2} B_N^{1/2}}, \tag{3.13}$$

where a full overlap factor $\xi(R) = 1$ has been assumed.

After averaging N signal pulses, the SNR improves by a factor $N^{-1/2}$ provided that the noise realizations are independent and the atmosphere stationary within the integration time. That is,

$$SNR(R) = \frac{K_s' U_s(R) S_p}{\left[\frac{2qF}{R_{io}}\left(K_s' U_s(R) + K_b' L_b\right) + NEP_m^2\right]^{1/2}}, \tag{3.14}$$

where $K_s' = \xi_0 K_s$, $K_b' = \xi_0 K_b$, and S_p is a scaling parameter that is computed as

$$S_p = \left(\frac{N}{B_N}\right)^{1/2}, \tag{3.15}$$

where N is the number of integrated pulses and B_N the noise-equivalent bandwidth in reception. In Eq. (3.14) the SNR is expressed as a function of 5 parameters, where K_s' and K_b' are characteristic constants of the lidar system while NEP_m, R_{io} and F are variables that only depend on the receptor module used. It is worth to note that in order to increase the SNR one can increase the number of integrated pulses but one can also decrease the noise-equivalent bandwidth.

As stated in Section 3.2, the photodetector module in this prototype is a combination of a Si-APD and a TIA. The photosensitive surface typically has a diameter (d_D) ranging between 0.25 to 5 mm (Table 3.1). The equivalent bandwidth B_N of the photodetector module must be greater than 2.5 MHz in correspondence with the specified range resolution $\Delta R < 30$ m (Table 3.1), assuming a pulse duration of $\tau_l \geq 10$ ns (Table 3.1) and a sampling frequency of $f_s = 2B_N$ (Nyquist criterion).

The chosen photodetector module is the Hamamatsu C5331-04 model (Hamamatsu, 2007), with photosensitive diameter $d_D = 3$ mm, noise equivalent power (NEP_m) of 400 fW/$\sqrt{\text{Hz}}$ and intrinsic responsivity (R_{io}) equal to 0.327 A/W. The excess noise factor (not specified by the manufacturer) is estimated at $F = 2.77$, where the empirical formula $F = M^n$ (Hamamatsu, 2004) has been applied, with $M = 30$ being the gain (Hamamatsu, 2007) and $n = 0.3$ the excess noise index (Hamamatsu, 2005). The commercial photodetector module has a bandwidth of 80 MHz. As the SNR is inversely proportional to the square root of the bandwidth (Eqs. 3.14 and 3.15) one can improve the SNR by applying a low-pass digital filter to the receiver output signal. In the simulations presented next, a filter cuf-off frequency, $f_c = 3$ MHz is used, which yields a noise-equivalent bandwidth, $B_N = 3$ MHZ in Eq. (3.15). Similar bandwidths are used by other commercial ceilometers (Vaisala, 2004).

From Eq. (3.15), a scaling parameter $S_p = 0.224$ is obtained with $B_N = 3$ MHz and $N = 150000$ signal pulses averaged. The latter value corresponds to an observation time equal to 30 s (temporal resolution used by the ceilometer network of the German Meteorological Service (Heese et al., 2010)), and a typical PRF equal to 5 kHz. A spectral radiance of $L_b = 10^{-2}$ $\text{W}\cdot\text{m}^{-2}\cdot\text{nm}^{-1}\cdot\text{sr}^{-1}$ at 905-nm wavelength, corresponding to the diffuse component of typical background radiance, has been assumed (Measures, 1992).

In the SNR simulations presented below the system constant K_s' and the background-radiance system constant K_b' have been tuned according to the variants shown in Table 3.2. The system constant (K_s') takes values ranging from 0.5 to 20 $\text{W}\cdot\text{m}^3$, where in Eq. (3.9) pulse energies (E_0) between 1 and 10 μJ (Table 3.1) are assumed as well as receiving diameters d_0 ranging from 100 to 200 mm (Table 3.1). The background-radiance system constant K_b' takes two values, $K_b' = 2.5\cdot10^{-5}$ and $2\cdot10^{-7}$ $\text{m}^2\cdot\text{nm}\cdot\text{sr}$, which correspond respectively to configurations with low and moderate rejection of background radiation. Receiving diameters of $d_0 = 200$ and 150 mm, half-angle FoV of $\phi = 5$ and 1 mrad, and interference filter widths of $\Delta\lambda = 25$ and 10 nm are assumed respectively for each configuration in Eq. (3.11). A higher drop in K_b' would not entail significant improvements in the SNR since for $K_b' \leq 2\cdot10^{-7}$ $\text{m}^2\cdot\text{nm}\cdot\text{sr}$ the dark-shot and the thermal noise terms are predominant over the photo-induced noise variance (Eqs. 3.4-3.6). A typical receiving optics transmission factor $\xi_0 = 0.4$ is assumed in all the variations.

Variant number	System constant K_s' [$\text{W}\cdot\text{m}^3$]	Background-radiance system constant K_b' [$\text{m}^2\cdot\text{nm}\cdot\text{sr}$]
1	20	$2\cdot10^{-7}$
2	2	$2\cdot10^{-7}$
3	0.5	$2\cdot10^{-7}$
4	20	$2.5\cdot10^{-5}$
5	2	$2.5\cdot10^{-5}$
6	0.5	$2.5\cdot10^{-5}$

Table 3.2. Parameters considered in the SNR simulations.

Figure 3.3(a) shows the simulations of the SNR for variants 1 to 6 of Table 3.2. Also represented is the value $SNR_{goal} = 5$. This threshold has been considered sufficient to apply an automatic cloud detection algorithm. For example, the STRAT algorithm (Morille et al., 2007) uses a SNR threshold equal to 3 to determine where the signal is strong enough to extract information. It can be seen that for all variants the SNR progressively decreases over the 0-3 km range, corresponding to the planetary boundary layer (PBL). At the end of the PBL, a sharp fall in SNR can be observed as result of the disappearance of Mie backscattering, with only the component of molecular origin remaining. Likewise, the SNR peaks can be observed at an altitude of 7.5 km, corresponding to the light water cloud located at this range. These peaks can be seen in greater detail in Fig. 3.3(b).

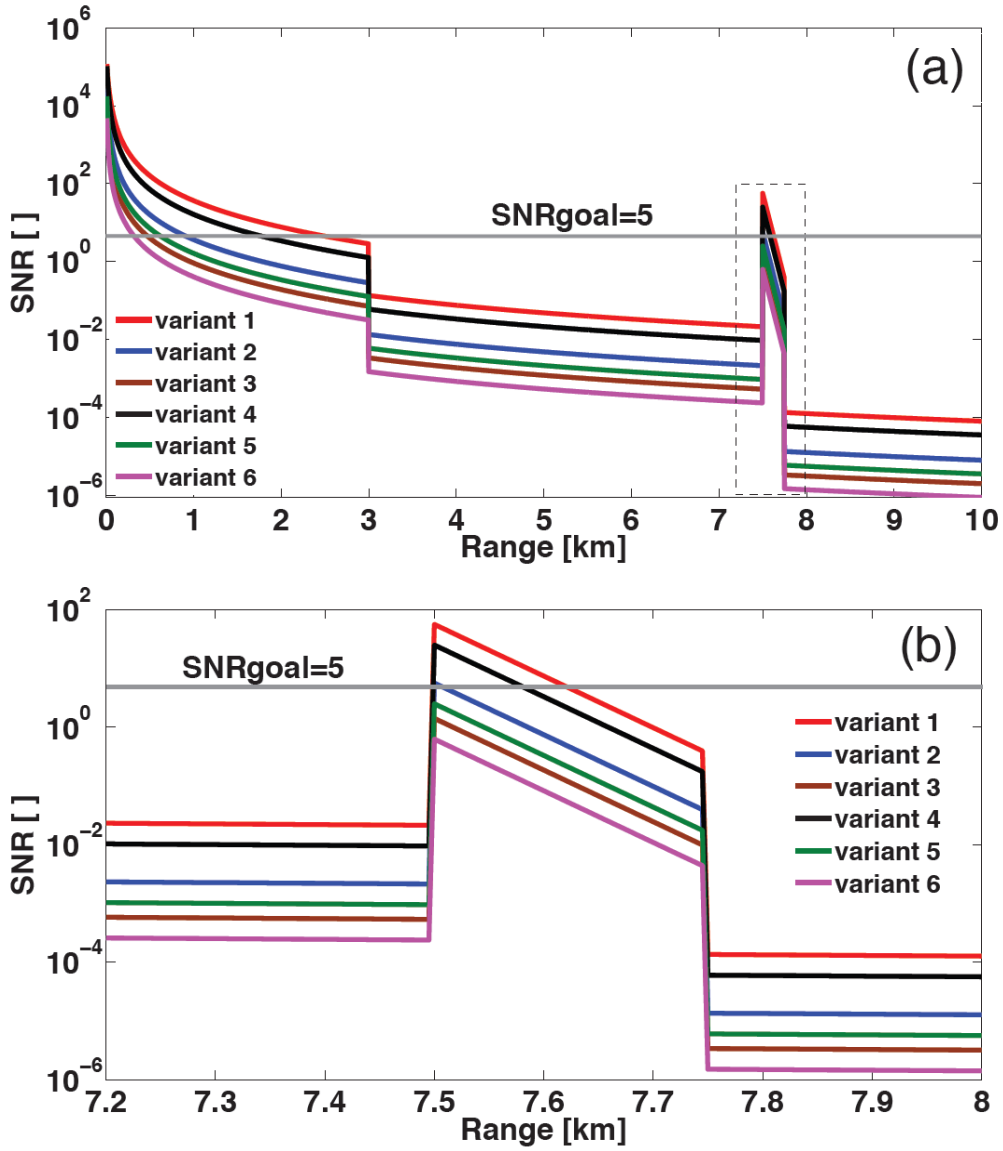

Fig. 3.3. Signal-to-noise ratio simulations under Mie/Rayleigh atmospheric model. (a) Signal-averaged range-dependent SNR. (b) Signal-averaged range-dependent SNR due to light-water cloud layer in the 7.5-7.75 km range (zoom of Fig. 3.3 (a)) for variants 1 to 6 (Table 3.2).

A clear correlation can be observed in Fig. 3.3(b) between the SNR peak due to the cloud and the system constant K_s'. Therefore, when the system constant takes low values, $K_s' = 0.5$ W·m^3 (variants 3 and 6), the threshold $SNR_{goal} = 5$ is not reached, while for high values, $K_s' = 20$ W·m^3 (variants 1 and 4), the cloud is detected. For $K_s' = 2$ W·m^3 (variants 2 and 5) it can be seen how the SNR value approaches 5 as background-radiation rejection improves (K_b' decreases). For variant 2 a SNR equal to 5.66 is achieved (equivalent to a SNR of 3 considering an observation time of 10 s).

From the above results, it can be concluded that the system constant K_s' must be of the order of 2 W·m^3, since for lower values, $K_s' = 0.5$ W·m^3, the required detection sensitivity is not reached, and for higher values, $K_s' = 20$ W·m^3, the system would become unnecessarily oversized and expensive. For eye-safety reasons in the developed prototype, the energy emitted per laser pulse was limited to $E_0 = 1.76$ μJ (Section 3.4), and a receiving diameter of $d_0 = 150$ mm was used to ensure the specified system constant $K_s' = 2$ W·m^3.

3.3.2 Overlap Factor (OVF) Simulations

The overlap factor (OVF) is defined as the fraction of the illuminated atmospheric cross-section at a distance *R* that is viewed by the receiving optics (Measures, 1992),

$$\xi(R) = \frac{A\{r_T(R), W(R); d(R)\}}{\pi W^2(R)}, \tag{3.16}$$

where A [m^2] is the area overlap function, $r_T(R)$ [m] is the radius of the receiver-optics FOV in the target plane, $W(R)$ [m] is the radius of the laser pulse in the target plane and $d(R)$ [m] is the separation of the emission and reception axes in the target plane. It is worth to note that the overlap factor has been calculated by taking into account only geometrical factors on the illuminated atmospheric target plane. In this reasoning it has been assumed that the entrance pupil of the telescope is the telescope aperture (i.e., the imaging properties of the receiving optics do not affect the OVF or, in other words, the OVF can indistinctly be computed at the atmosphere plane or at the detector plane. See also Sect. 3.4.2, Fig. 3.7).

By following (Measures, 1992), the overlap factor can be expressed as a function of geometrical and optical parameters of the lidar system,

$$\xi(R) = f(\phi, \theta, \delta, r_0, W_0, d_i), \tag{3.17}$$

where all the parameters have been presented in Section 3.2 and Fig. 3.1.

The geometry of a biaxial lidar is shown in Fig. 3.4 when the emission and reception axes are divergent ($\delta < 0$) and convergent ($\delta > 0$). It can easily be deduced that to achieve full overlap the following expression must be satisfied

$$-(\phi - \theta) \le \delta \le \phi - \theta, \tag{3.18}$$

from which it is clear that the half FOV, ϕ must be greater than the laser beam divergence, θ and that they can only take equal values when the two axes are parallel.

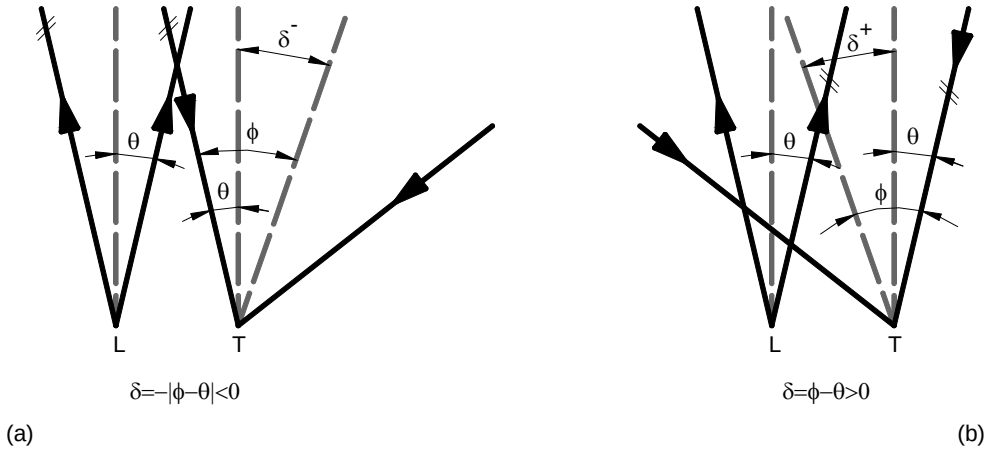

Fig. 3.4. Geometry of a biaxial lidar where "L" stands for laser and "T" stands for telescope. (a) Laser and telescope axes are divergent. (b) Laser and telescope axes are convergent.

In the following simulations a study is carried out on the variation of the overlap factor, Eq. (17), with the receiving FOV ϕ, the laser beam divergence θ and the tilt angle δ according to the values given in Table 3.3. Values ranging from $\phi = 1$ to 5 mrad (Table 3.1) are considered for the FOV. Similarly, laser beam divergences (θ) between 0.75 and 4.75 mrad are assumed, though in all the variants $\phi > \theta$ is met. For the tilt angle δ, the cases of parallel ($\delta = 0$ *mrad*), and convergent ($\delta = 1$ *mrad*), optical axes are considered. The case of divergent optical axes is not considered, as it is clear from Fig. 3.4 that the range of full overlap R_{OVF} is lower when the axes converge than when they diverge.

Variant number	Field of view ϕ [mrad]	Laser divergence θ [mrad]
1'	5	4.75
2'	5	2.75
3'	5	0.75
4'	3	2.75
5'	3	0.75
6'	1	0.75

Table 3.3. Parameters considered in the OVF simulations for tilt angles $\delta = 0$ and 1 mrad.

For all variants an effective radius of the receiving optics of $r_0 = 75$ mm (Section 3.3.1) is assumed, as well as a distance between axes of $d_i = 150$ mm and a transmitter output laser beam radius of $W_0 = 150$ μm, which is a standard value in laser diodes. The value of the distance between axes d_i is taken bearing in mind that, on one hand, minimizing this distance is of interest because the range of full overlap R_{OVF} lowers when d_i decreases (Measures, 1992). On the other hand, d_i must be greater than the sum of the radii of the receiving optics $r_0 = 75$

mm (Section 3.3.1) and emission optics $r_e = 25$ mm (Section 3.4). To regulate this distance a translational platform is used in the designed ceilometer prototype.

Figure 3.5 represents the OVF simulations which correspond to totally parallel emission and reception optical axes (i.e. $\delta = 0$ mrad). In this case, full overlap is achieved provided the FOV is greater than the laser-beam divergence, $\phi > \theta$, as established for all the variants considered. When the value of the divergence approaches to the FOV (variants 1', 4' and 6'), full overlap is achieved at further altitudes, between 200 and 300 m. The lowest range of full overlap, $R_{OVF} = 20$ m, is achieved for the combination of a wide FOV, $\phi = 5$ mrad, with a narrow laser beam divergence, $\theta = 0.75$ mrad (variant 3').

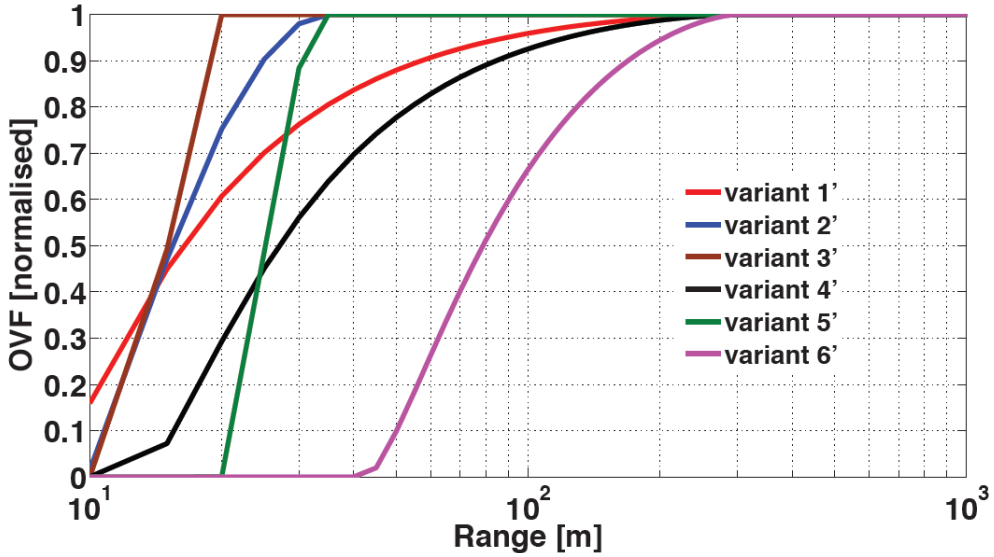

Fig. 3.5. Normalized overlap factor (OVF) versus range for variants 1' to 6' (Table 3.3). Tilt angle $\delta = 0$ mrad (parallel axes).

Figure 3.6 shows the OVF simulations when the optical axes have a misalignment, $\delta = 1$ mrad (i.e., convergent axes). For variants 1', 4' and 6' the difference between the FOV and laser beam divergence is $\delta > \phi - \theta$ and Eq. (3.18) is not satisfied. In these cases, full overlap is only achieved for an interval of ranges of between approximately 60 and 200 m, while at further ranges the overlap is partial. For the remaining variants ($\delta < \phi - \theta$) full overlap occurs at closer ranges than when the optical axes are totally parallel ($\delta = 0$ mrad), with the most favourable case being variant 3' ($\phi = 5$ mrad, $\theta = 0.75$ mrad), in which $R_{OVF} = 15$ m.

To select the most adequate FOV ϕ, it needs to be borne in mind that low FOV values allow a reduction of the background radiation, whereas high values in combination with narrow laser divergences, allow low ranges of full overlap. In addition, for high FOV figures it is possible to use large-area APD's, an option that is preferred in order to avoid high-precision focusing onto the receiving detector. For the above reasons, a relatively high FOV (around 5 mrad) is chosen to permit low-range operation, while background radiation rejection is achieved by using a narrow-band interference filter. The laser divergence has to be minimized ($\theta < 2.75$ mrad) to

reduce the height of full overlap, but considering the trade-off that this parameter was on the eye-safety considerations discussed in Section 3.4. As in the previous simulations, it is obtained that the lowest range of full overlap corresponds to a tilt angle of $\delta = 1$ mrad. In the prototype a gimbal device has been implemented to adjust this angle (Table 3.4).

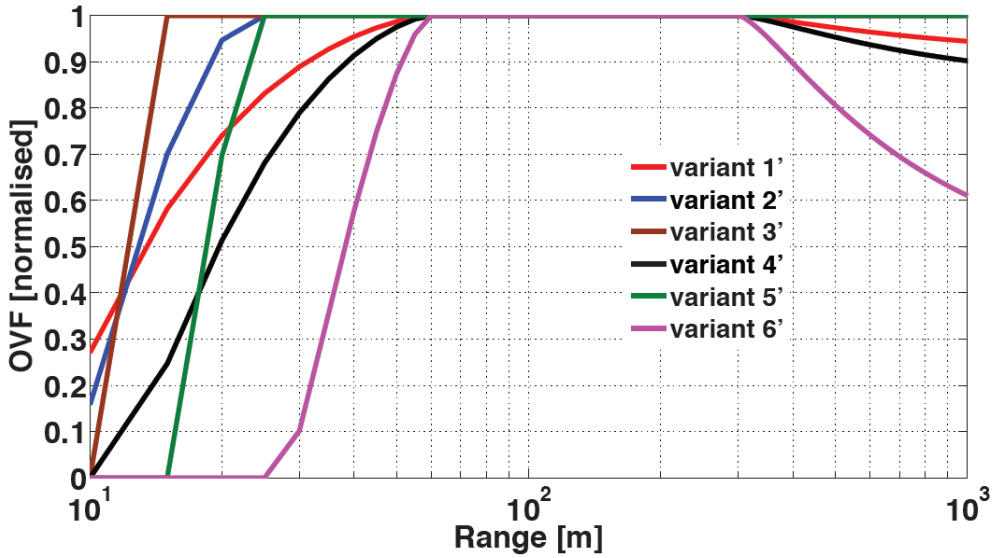

Fig. 3.6. Normalized overlap factor (OVF) versus range for variants 1' to 6' (Table 3.3). Tilt angle $\delta = 1$ mrad (convergent axes).

3.4 Opto-mechanical overview

The opto-mechanical configuration of the lidar ceilometer prototype developed by the authors is presented below. The final specifications of this configuration correspond to the results of the parametric simulations discussed in Section 3.3.

3.4.1 Emission subsystem

The emission source used is a 3B-class InGaAs 905 nm wavelength, 1.76 μJ-pulse energy, 5-kHz rep. rate laser diode characterized by a high divergence. In order not to overspill emission power, a convergent lens has been used at the laser output to reduce the emission divergence down to 2.27 mrad, a lower figure than the receiver FOV ($\phi = 4.92$ mrad, Table 3.4). To ensure an eye-safe system this convergent lens has been selected in accordance with IEC-60825 standard. Considering the conservative hypothesis of a point laser source, the output laser beam must meet the following three requirements in order not to exceed the Maximum Permissible Exposure (MPE) value:

- Human eye exposure to any laser pulse must be no higher than the MPE level for a single pulse,

$$MPE_{single} = 5 \times 10^{-3} \times C_4 = 12.9 \frac{\text{mJ}}{\text{m}^2}, \tag{3.19}$$

where the correction factor is $C_4 = 2.54$ for $\lambda = 905\,\text{nm}$ in IEC-60825 standard.

- Mean exposure to laser pulse train of duration T must be no higher than the MPE level for a single pulse of duration T ,

$$MPE_T = 18 \times T^{-0.25} \times C_4 = 260 \frac{\text{J}}{\text{m}^2}, \tag{3.20}$$

where a typical value $T = 10\,\text{s}$ has been used (IEC-60825). So, the exposure for a single pulse is

$$MPE_{single,\,mean} = \frac{MPE_T}{N} = 5.2 \frac{\text{mJ}}{\text{m}^2}, \tag{3.21}$$

where $N = 5 \times 10^4$ is the number of pulses for a duration T assuming $PRF = 5 \times 10^3$ Hz (Table 3.4).

- Exposure to any single pulse of the pulse train must be no higher than the MPE level for a single pulse multiplied by a correction factor $N^{-0.25}$. Factor $N^{-0.25}$ is aimed at correcting the threshold for high repetition rates. That is,

$$MPE_{train} = MPE_{single} \times N^{-0.25} = 0.859 \frac{m\text{J}}{\text{m}^2}, \tag{3.22}$$

From Eqs. (3.19)-(3.22) above, it is obvious that Eq. (3.22) gives the most restrictive MPE (energy density threshold). Combining this MPE threshold with the 1.76 μJ laser output energy (Table 3.4), it is found that the output laser-beam aperture radius must be greater than 25.5 mm. The ceilometer uses a standard-size convergent lens of 50 mm diameter placed at $f_e = 75\,\text{mm}$ from the diode laser window as the effective emission aperture. Therefore, the laser spot size on the effective emission aperture is

$$r_{se} = f_e \tan(\theta_\perp) = 27.3 \;\; mm, \tag{3.23}$$

where r_{se} is the laser spot radius on the convergent lens (effective emission aperture), $f_e = 75$ mm (Table 3.4) is the convergent lens focal distance and $\theta_\perp = 20^\text{o}$ is the laser beam maximum divergence. The resultant system is therefore eye-safe although, since a standard size of lens has been chosen, slight energy losses occur in transmission as the laser beam section is slightly larger than the selected lens. It should be mentioned that since the transverse distribution of the laser light is Gaussian, losses will be lower than the nominal ones predicted assuming uniform illumination (~16%).

3.4.2 Receiving subsystem

Figure 3.7 is a sketch of the designed receiving optical system, which is used to focus the backscattered light onto the photodetector surface, a Hamamatsu C5331-04 silicon APD module (Table 3.4). A Fresnel lens (L_1) is used as the system objective as it is a low-cost solution characterized by a low *f* number and reduced absorption. Another recent application of Fresnel lenses in lidar systems can be found in De Young and Barnes (2010). L_1 is followed in the receiving system by the divergent collimating lens (L_2) so as to ensure that the incoming light rays are incident in the normal direction on the 10 nm interference filter (FILT) surface, otherwise detuning of the spectral response of the filter occurs. Next, convergent lens (L_3) is used to focus filtered light onto the APD.

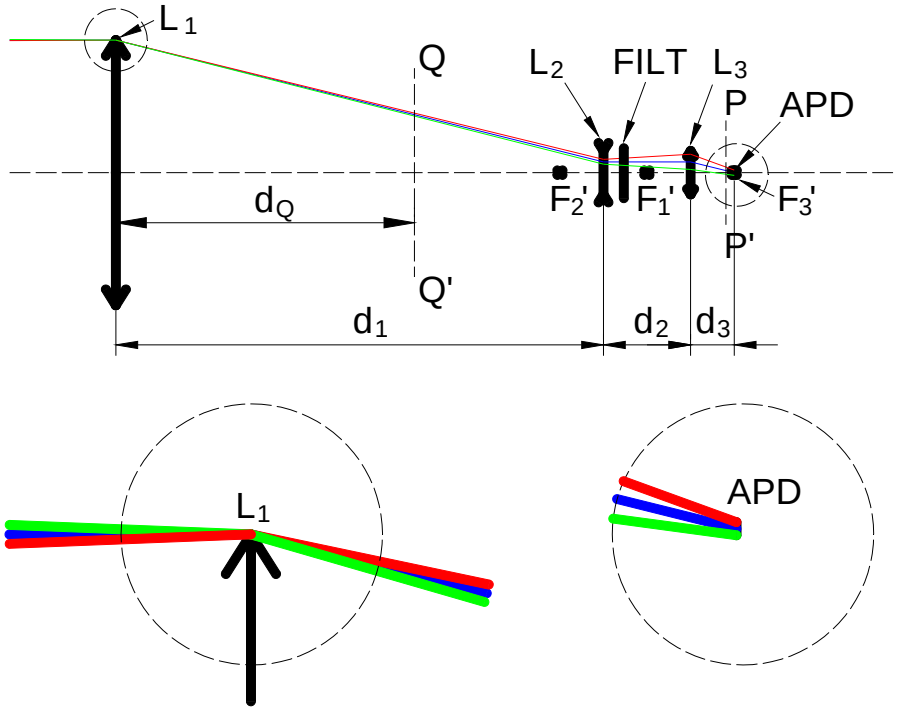

Fig. 3.7. Ceilometer optical receiving chain scheme (see also Table 3.4). (L_1) Primary lens (Fresnel), (L_2) divergent lens, (FILT) interference filter, (L_3) convergent lens, (APD) photodetector active area. Distances d_1 (user adjustable), d_2 and d_3 (user adjustable) show the confocal arrangement of the set up, that is L_1, primary-lens image focal point, F_1', and L_2 object focal point, F_2, coincide ($F_1' \equiv F_2$). Likewise, the photodetector is represented as placed in L_3 image focal plane ($d_3 = |f_3|$). Joint block L_2-FILT-L_3-D-APD (see Fig. 3.8) can be displaced together in relation to L_1 by adjusting d_1. Red and green rays correspond to the maximum FOV accepted by the telescope.

Though practical implementation of the receiving system enables adjustment of distances d_1 and d_2 in Fig. 3.7, their nominal setting is the confocal arrangement $d_1 = |f_1| - |f_2|$, $d_2 = |f_2| + |f_3|$ and $d_3 = |f_3|$. Using matrix ray-propagation analysis (Möller, 1988), it is possible to derive the equivalent focal length of the receiving optical system as

$$f_{eq} = \frac{f_1 \cdot f_3}{f_2}, \tag{3.24}$$

where f_{eq} is the equivalent focal length, f_1 is the primary convergent lens focal length (L_1: Fresnel), f_2 is the divergent lens focal length (L_2) and f_3 is the convergent lens focal length (L_3).

If, as is the case, the design condition $f_2 = f_3$ is imposed, the receiving FOV ϕ becomes

$$\phi = \frac{r_D}{f_{eq}} = \frac{r_D}{f_1} = 4.92 \quad mrad\,, \tag{3.25}$$

where $r_D = 1.5$ mm is the APD radius.

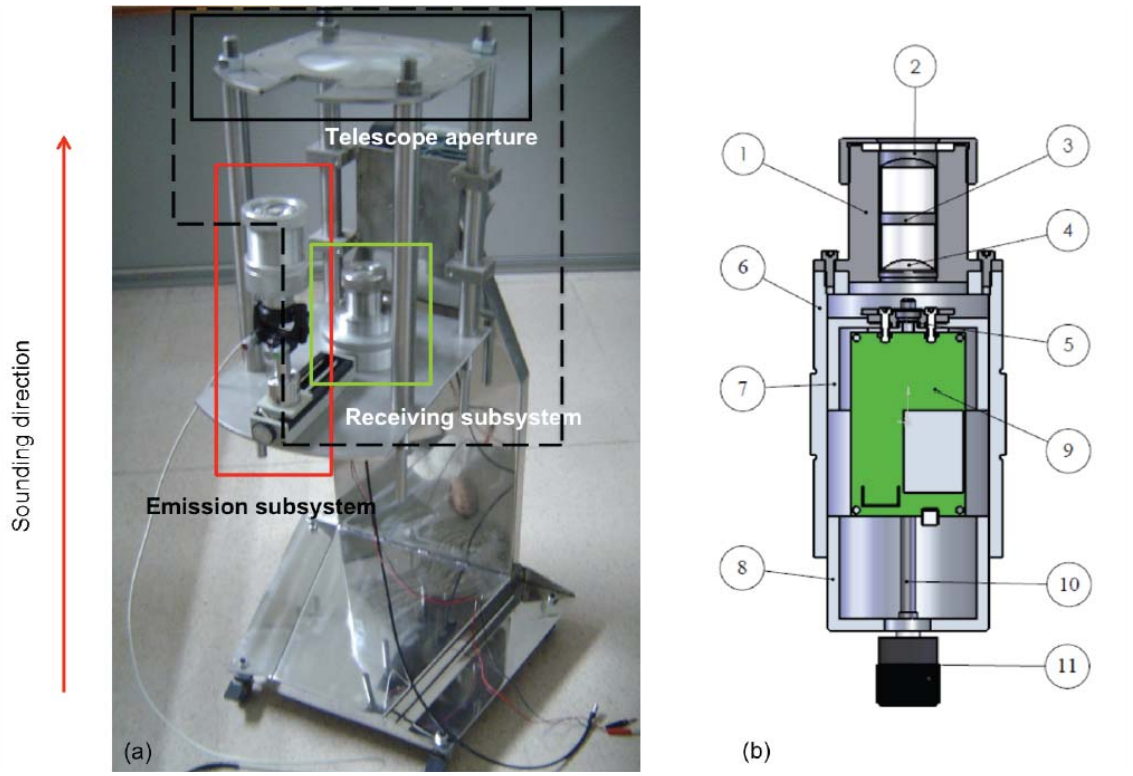

Fig. 3.8. Emission/Receiving opto-mechanical configuration. (a) Picture of the ceilometer prototype showing the emission (red box) and receiving (black dashed box) subsystems. (b) Cross-view showing the APD-to-focal-plane regulator mechanism (marked with a green box in (a)). Main components are: (1) receiving lens housing assembly (L_2-FILT-L_3), (2) divergent lens L_2, (3) Interference filter (FILT), (4) convergent lens L_3, (5) photodetector surface, (6) opto-electronic receiver support, (7) APD receiver module support frame, (8) receiver opto-mechanical lower cover, (9) Si-APD receiver module, (10) convergent-lens focal-distance regulation axis, (11) focal distance regulation knob. See extensive details in Gregorio et al. (2006).

As an introduction to the designed prototype, Fig. 3.8(a) shows the mechanical structure containing the optical systems presented above. The cross-section of the receiving opto-mechanical system is depicted in Fig. 3.8(b). The blocks (2), (3) and (4) correspond to the block L_2-FILT-L_3 in Fig. 3.7. The opto-mechanical structure features regulation capacity by means of the knob (element 11). Adjustment of the APD-to-focal-plane distance d_3 (i.e., L_3-to-APD distance) and its operation is as follows: by turning the focal distance regulator knob (element 11), the focal distance regulator axis (element 10) screws into the APD support frame (element

7) and causes vertical movement of the APD receiver module (element 9). As a result, the photodetector surface (element 5) varies its distance to convergent lens L_3. This regulator allows precise positioning of the photodetector surface at L_3 focal plane, thus offsetting any focal-length tolerance.

3.5 Preliminary prototype

A first preliminary low-cost prototype has been developed for remote sensing of cloud-base heights as a cooperative sensor for forecasting storm initiation. This initial experimental prototype is aimed at studying and identifying the critical parameters of the system with a view to a more refined prototype. The constructed lidar ceilometer (Fig. 3.8) has a high number of degrees of freedom (i.e., many adjustable parts), including amongst others: adjustment of emission and reception optical elements, adjustment of the distance and misalignment angle between optical emission and reception axes by means a translational platform and gimbal device, and instrument aim control by means of reducing gear.

The experimental results obtained by the lidar ceilometer are exposed below. Section 3.5.1 briefly reports the procedure used to detect a topographic target and Sect. 3.5.2 shows preliminary test measurements for cloud detection, advertising that the system is able to detect atmospheric echoes at highs up to 7 km in height with acceptable likelihood as claimed in the link budget simulations.

3.5.1 Measurement of a topographic target

To ensure that the lidar ceilometer measures appropriately it was aimed nearly horizontally and pointing to a mountain located at ~1.2 km (Fig. 3.9(a)). This measurement was used to adjust the receiving optics and to align the optical axes. Figure 3.9(b) plots the backscattered power $P(R)$ vs distance and shows a very clear peak located at the distance of the topographic target.

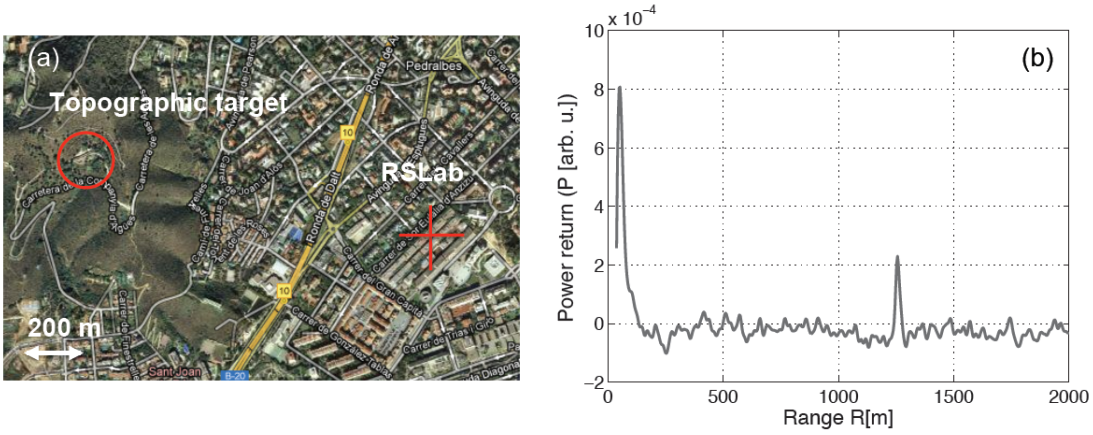

Fig. 3.9. Detection of a topographic target with the lidar ceilometer placed at the UPC premises in North Campus (Barcelona). (a) Satellite view of the ceilometer location, as well as location of the mountain. (b) Backscattered power $P(R)$ vs distance. The spatial resolution is 3.75 m and observation time 10 s. The peak located at ~200 m is a detection artefact caused by the rising edge of the OVF (overlap factor smaller than 1), and therefore, not all backscattered light is collected by the photodetector.

3.5.2 Cloud detection

Figure 3.10 presents initial atmospheric measurements obtained with the constructed prototype. In order to enhance the SNR, raw data provided by the photodetector module has been filtered with a 3 MHz cut-off frequency according to the noise-equivalent bandwidth discussed in Sect. 3.3.1. A 3 MHz low-pass FIR filter based on the Parks-McClellan algorithm (2005) has been used as spatial smoothing. These kinds of linear phase filters are optimal to minimize the maximum error between the desired frequency response and the actual frequency response.

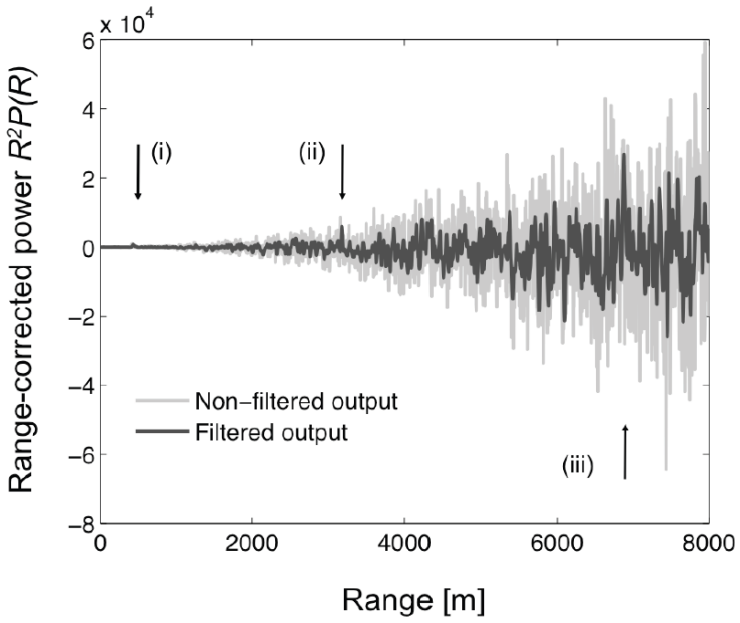

Fig. 3.10. Preliminary test measurement showing detection of a storm low cloud (*i*) and two possible high clouds (*ii*) and (*iii*). Unfiltered (gray solid line) and filtered (black solid line) range-corrected power return, $R^2 \cdot P(R)$ vs distance. The spatial resolution is 3.75 m and the observation time 10 s.

Figure 3.10 compares the range-corrected received power before (gray solid line) and after applying the smoothing filter (black solid line). In both representations a cloud storm located at ~400 m can be clearly distinguished but only in the filtered output two small peaks (not observed in the non-filtered data) located at 3200 m and 6900 m are evidenced. It is worth to note that after applying the filter the SNR has increased but at the expense of a lower spatial resolution.

Figure 3.11 shows in better detail the range-corrected peaks detected with the ceilometer. The estimated SNR at the cloud peak located at ~400 m is SNR=25.6, value that has been estimated by computing the ratio between the intensity at the cloud peak (420 m) and the noise-standard deviation in its vicinity. The noise standard deviation has been computed by assuming Gaussian statistics and by averaging the 6-σ noise amplitude (equivalently, ±3-σ noise amplitude) at the approximate cloud base (350 m). Details of the piece-wise SNR estimator can be found in Reba et al. (2007). The estimated SNR for the peak located at 3200 m is 5.8 and has a qualitatively small false-alarm probability (Skolnik, 2001) while for the peak at 6900 m the estimated SNR is 4.7 and the associated false alarm probability can comparatively be considered moderate/moderate-to-high.

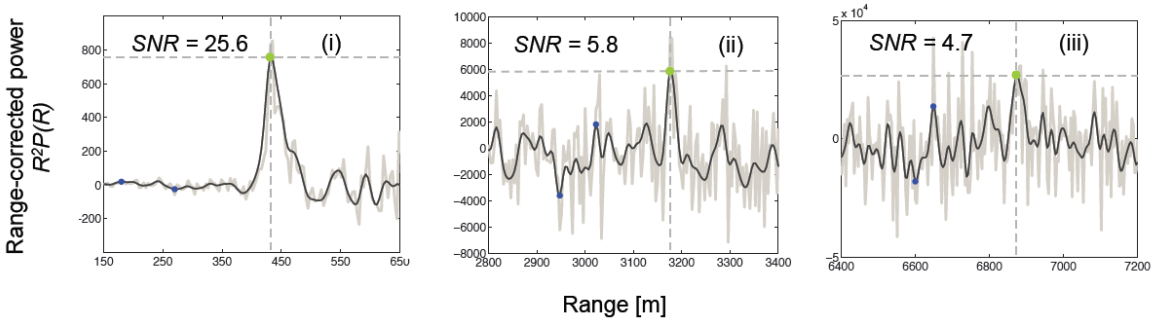

Fig. 3.11. Range-corrected power, $R^2 \cdot P(R)$ vs distance. Panels (*i*), (*ii*) and (*iii*) show the detected peaks in better detail. Green dots mark the absolute maximum of the peak, and the blue dots the relative maximum and minimum of the background noise in the vicinity of the peak.

The system specifications of the ceilometer prototype are summarized in Table 3.4.

PERFORMANCE		Max. detection range, $R_{\max}$	7500 m
		Range resolution, ΔR	3.75 m
		Eye safety	Class 1M IEC/EN60825-1
EMITTER	Laser	Model	Laser Components IRLM-080-010-4S12
		Wavelength, λ	905 nm (InGaAs)
		Pulse energy, E_0	1.76 μJ
		Pulse duration, τ_l	10.1 ns
		Pulse repetition frequency, *PRF*	≤ 5 kHz
	Optics	Lens diameter, d_e	50 mm
		Focal length, f_e	75 mm
		Output beam divergence, θ	2.27 mrad (half-angle)
RECEIVER	Optics	Primary lens diameter, d_0	152.4 mm
		Equivalent focal length, f_{eq}	304.8 mm
		Focal number, $f_n = \frac{f_{eq}}{d_0}$	2
		Field of view, ϕ	4.92 mrad (half angle)
	Interference Filter	Centre wavelength, λ	905 nm
		Full width at half maximum, $\Delta\lambda$	10 nm
	APD	Model	Hamamatsu C5331-04
		Active area diameter, d_D	3 mm
		Spectral response range	400 to 1000 nm
		Responsivity, R_i	9.81 A/W (905 nm)
		Noise Equivalent Power, NEP_m	400 fW/$\sqrt{\text{Hz}}$
		Internal gain, M	30
TILTING REGULATOR	Gimbal	Model	Edmund Optics 25.0MM ID
		Azimuthal travel / knob rotation	8.33 mrad
		Elevation travel / knob rotation	6.41 mrad

Table 3.4. Main characteristics of the designed prototype.

3.6 Conclusions

Design methodology of an eye-safe 905 nm wavelength, 1.76 μJ-energy, 5 kHz rep. rate, APD-based ceilometer prototype for cloud-base detection has been achieved using parametric simulation. The method uses a convenient analytical reformulation of the range dependent SNR in a backscatter lidar, Eqs. (3.14) and (3.15), and simulation of the laser/telescope overlap function in terms of Eqs. (3.17) and (3.18). The modified SNR formulation of Eq. (3.14) expresses the SNR in terms of the equivalent lidar system constant (K_s') and background radiance constant (K_b'), a choice of the opto-electronic receiver (parameter subset given by the receiver (NEP_m), intrinsic responsivity (R_{io}) and excess-noise-factor (F), and specs on the required observation time and spatial resolution (equivalently, the noise equivalent bandwidth) via Eq. (3.15). Ceilometer characteristic parameters (including a review of optoelectronic receiver parameters) from the technological state of the art at 905 nm are summarized in Table 3.1. Future refinements of the prototype will simplify the mechanical solution presented, hence reducing the degrees of freedom of the adjustable parts presented here (deliberately large for testing purposes). In the Appendix of this PhD thesis it is proposed the implementation of a spatial filter in order to improve the background power rejection of the ceilometer prototype.

4

Measurement of spray drift using passive collectors and a UV lidar system

As it has been seen in Chapter 2, conventional methods applied in drift measurement are based on the use of point collectors which are unable to obtain information concerning the temporal or spatial evolution of the pesticide cloud. Such methods are also costly, labour-intensive, and require a considerable amount of time.

In this chapter an analysis will be undertaken of the results obtained from an experimental campaign involving multiple ground spray tests. A lidar system and two types of passive collectors (nylon strings and water-sensitive paper sheets) were used simultaneously to measure the drift. The lidar allowed monitoring the temporal evolution of the pesticide cloud with high range resolution (1.5 m) without the need for subsequent chemical analyses. A high linear correlation ($R^2 \approx 0.90$) was observed between the lidar signal and the tracer mass captured by the nylon strings. It is concluded that an advantageous alternative is offered with lidar technology in comparison with current drift monitoring methods.

4.1 Introduction

As reviewed in Section 2.3.1, lidar systems, principally the elastic type ones, have been used in a number of studies for pesticide drift monitoring in both aerial and, though to a lesser extent, ground spray treatments. In most cases the lidar was used to study the movement and dispersion of the pesticide plumes at a qualitative level. However, key questions such as the application of the lidar to quantify droplet concentration in the pesticide clouds or determine spray drift flux (performance of mass balance) have scarcely been addressed (Hiscox et al., 2006; Khot et al., 2011).

In this chapter, an analytical and experimental study is undertaken on the relationship between spray drift measurements obtained with an elastic-backscatter lidar system and those made using passive collectors, in this case nylon strings and water-sensitive paper sheets.

This chapter is organised into five sections. Section 4.1 comprises this introduction. A theoretical model is proposed in Section 4.2 which relates the information obtained with the passive collectors and the lidar signal. This model takes into account the meteorological and application conditions. Section 4.3 offers a description of the materials and methods employed during the experimental campaign. Section 4.4 presents and compares the results with the theoretical model. Finally, the conclusions are given in Section 4.5.

4.2 Model analysis

A model is firstly proposed in this section which relates the lidar signal to the parameters of the monitored plume drift. Secondly, a model is considered which relates the collector measurements (nylon strings and water-sensitive paper) to the spray drift. Finally, based on the two aforementioned models, the relationship that exists between the measurements of the two sensor types is established. The experimental consistency of this model is studied in Sections 4.4.3 and 4.4.4.

4.2.1 Spray drift retrieval model of data obtained from a lidar sensor

Lidar measurements are based on the well-known single-scattering form of the elastic lidar equation (Collis and Russell, 1976), presented in Section 3.3.1 (Eqs. 3.7 and 3.8) and which is reproduced here for better understanding of subsequent analytical developments. The return power component $P(R)$ [W] received by the lidar and due to a spray drift cloud located at a range R [m] is computed as

$$P(R) = \frac{E_0 A_r c}{2} \frac{\beta(R)}{R^2} \exp\left[-2 \int_0^R \alpha(r) dr \right], \tag{4.1}$$

where E_0 [J] is the energy emitted per laser pulse, A_r [m^2] is the effective receiver area, c [ms^{-2}] is the speed of light, $\beta(R)$ [$m^{-1}sr^{-1}$] is the total atmospheric volume backscattering coefficient and $\alpha(r)$ [m^{-1}] is the total atmospheric volume extinction coefficient.

The received backscattered signal [V] is given by

$$V(R) = R_i G_T P(R) \xi_0, \tag{4.2}$$

where R_i [A/W] is the photodetector current responsivity, G_T [Ω] is the receiver transimpedance gain, and ξ_0 is the total transmission factor of the receiving optics. A full overlap factor $\xi(R) = 1$ has been assumed.

Substituting Eq. (4.1) into (4.2), the range-corrected signal $S(R)$ [Vm^2] is obtained, given by Eq. (4.3),

$$S(R) = R^2 V(R) \approx K \beta(R), \tag{4.3}$$

where K [Vm^3] is a constant characteristic of the system given by Eq. (4.4),

$$K = \frac{R_i G_T E_0 A_r c \xi_0}{2}, \tag{4.4}$$

and $\beta(R)$ is the total atmospheric volume backscattering coefficient, given by Eq. (4.5). For greater simplicity, atmospheric extinction has been disregarded in the calculation of Eq. (4.3). This approximation is valid when the clouds to be monitored are near-field clouds and their transmittance takes values close to the unit (reduced optical depth). Both conditions are met in the measurements presented in this chapter.

$$\beta(\lambda, m, R) = \int_0^\infty \sigma_B(r_p, \lambda, m, R) N'_p(r_p, R) dr_p, \tag{4.5}$$

where $\sigma_B(r_p, \lambda, m, R)$ [m^2/particle] is the backscattering cross-section of a particle of radius r_p [m] and complex refractive index m when illuminated by light of wavelength λ. $N'_p(r_p, R)$ [particles/m^3] is the particle number concentration, defined as the number of particles per unit volume with radius between r_p and $r_p + dr_p$. In what follows the dependency of the backscatter coefficient with λ and m will be disregarded for notational simplicity. The backscattering cross-section can be written as

$$\sigma_B(r_p, \lambda, m, R) = \pi r_p^2 Q_B(x, m, R), \tag{4.6}$$

where $Q_B(x, m, R)$ is the backscattering efficiency, defined as the ratio of particulate backscattering cross-section to the geometric cross-section, and x is the size parameter, defined as

$$x = 2\pi r_p / \lambda \,. \tag{4.7}$$

For high values of x, the backscattering efficiency tends to an asymptotic value given by the Fresnel reflection coefficient (McDonald, 1962),

$$\lim_{x\to\infty} Q_B(x,m) = \left|\frac{m-1}{m+1}\right|^2 . \tag{4.8}$$

According to Miller (1993), the droplets that make up the drift clouds have a volumetric mean diameter (*VMD*) ranging between 18 and 93 μm. So, applying Eq. (4.7) and considering a wavelength of 355 nm (Table 4.2), it is found that x takes values ranging between 159 and 823.

Figure 4.1 shows that for these size parameters the backscattering efficiency of the water displays highly oscillatory behaviour. This behaviour is because the imaginary component of the water refractive index, $m = 1.36 - 2.42 \cdot 10^{-9} i$ (Segelstein,1981), has a very low value (Deirmendjian, 1969).

It should be noted that in the spray tests the liquid that was applied was not pure water but rather an aqueous tracer solution (Section 4.3.1), whose refraction index is unknown. In the absence of this information and in view of Fig. 4.1, it is concluded that the backscattering efficiency cannot be approximated by the ordinary reflection coefficient of pure water ($Q_B \approx 0.151$).

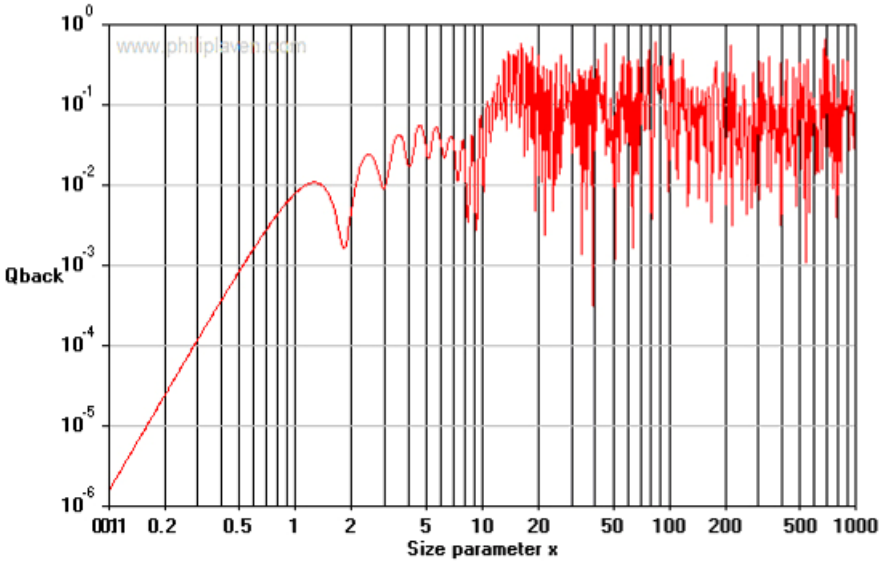

Fig. 4.1. Dependence of backscattering efficiency Q_B on the size parameter x for water. This simulation was performed using software MiePlot v.4.2 (Laven, 2011) for $m = 1.36 - 2.42 \cdot 10^{-9} i$.

Equation (4.9) is obtained from Eqs. (4.5-4.7). In this equation, the total atmospheric volume backscattering coefficient is expressed as a function of particle size. It is also considered that the lidar emits at a specific wavelength and it is assumed that, for each test, the drift droplets have similar refractive index values.

$$\beta(R) \approx \pi \int_0^\infty r_p^2 Q_B(r_p, R) N_p'(r_p, R) dr_p . \tag{4.9}$$

So, the range-corrected lidar signal will be given by

$$S(R) \approx \pi K \int_0^\infty r_p^2 Q_B(r_p, R) N_p'(r_p, R) dr_p . \tag{4.10}$$

Equation (4.10) can be expressed as

$$S(R) \approx \frac{K}{4} a_e(R), \tag{4.11}$$

where $a_e(R)$ is the modified surface area concentration [m^2/m^3], given by

$$a_e(R) = 4\pi \int_0^\infty r_p^2 Q_B(r_p, R) N_p'(r_p, R) dr_p . \tag{4.12}$$

The term "modified" accounts for inclusion of the backscattering efficiency, Q_B in Eq. (4.12), which is in contrast to the classic definition of the "effective surface area concentration" in the literature (Ansmann and Müller, 2005). The "modified" definition of Eq. (4.12) can be interpreted as the "backscatter cross-section area concentration".

In order to compare the lidar measurements with those obtained from the passive collectors, it is necessary to add together the signals received by the lidar system during the time interval t_{int} over the course of which the drift cloud is detected. The range-corrected and time-integrated lidar signal $IS(R)$ is calculated as

$$IS(R) \approx \sum_{i=1}^{N} S_i(R), \tag{4.13}$$

where $S_i(R)$ is the range-corrected signal corresponding to the measurement i and N is the total number of lidar measurements made during the time interval t_{int}, given by

$$N = \frac{t_{\text{int}}}{T_f}, \tag{4.14}$$

where T_f [s] is the pulse repetition time of the lidar system. Through Eqs. (4.13) and (4.14), the following expression for the time-integrated lidar signal is obtained

$$IS(R) \approx \frac{t_{\text{int}}}{T_f} \frac{K}{4} \overline{a_e}(R), \tag{4.15}$$

where $\overline{a_e}(R)$ is the time-average modified surface area concentration during the integration time, t_{int}. In doing this average it is assumed that the range-dependent particle size distribution and related cross-section are nearly time invariant.

4.2.2 Spray drift retrieval model from passive tracer collectors

The spray liquid volume collected by a nylon string (passive collector) located at a range *R* can be expressed as

$$V_d(R) = V_{air}(R)\overline{\rho_d}(R), \tag{4.16}$$

where $V_{air}(R)$ [m^3 air] is the effective air volume sampled by that collector segment and $\overline{\rho_d}(R)$ [m^3 spray liquid/m^3 air] is the average total volume concentration of spray liquid during the integration time. An upper bar indicates "averaged" over the integration time. The total volume concentration ρ_d is defined by Ansmann and Müller (2005) as

$$\rho_d(R) = \frac{4\pi}{3}\int_0^\infty r^3 N_p'(r,R)dr\,. \tag{4.17}$$

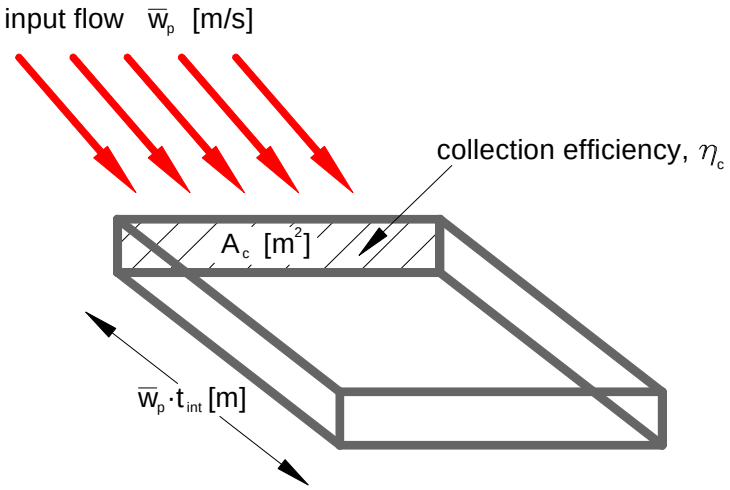

Fig. 4.2. Volume of air sampled by a collector segment of cross-section A_c and efficiency η_c over an integration time t_{int} and considering a plume speed $\overline{w_p}$.

The effective air volume sampled by the collector segment (Fig. 4.2) is given by

$$V_{air}(R) = A_c \overline{w_p} \eta_c t_{int}\,, \tag{4.18}$$

where A_c [m^2] is the projected area of the collector segment, $\overline{w_p}$ [m/s] is the average speed of the plume or the average speed at which the droplets reach the collector, η_c is the collector efficiency (defined in Section 2.1.1) during the test and t_{int} has been previously presented.

Substituting Eq. (4.18) in (4.16), the following expression is obtained for the spray liquid volume $V_d(R)$ [m^3 spray liquid drift] captured by a collector segment

$$V_d(R) = A_c \overline{w_p} \eta_c t_{int} \overline{\rho_d}(R)\,. \tag{4.19}$$

Equation (4.19) indicates that the spray liquid volume captured over a time t_{int} by each string collector segment is determined by the average volume concentration $\overline{\rho_d}(R)$ of airborne spray liquid over this time.

4.2.3 Relationship between lidar signal and deposition on linear passive collectors

The modified effective radius r_{eff} (surface-area-weighted mean radius) at a given range R from the lidar is defined as

$$r_{eff}(R)=\frac{\int_0^{\infty} r_p^3 N_p'(r_p,R)dr}{\int_0^{\infty} r_p^2 Q_B(r_p,R)N_p'(r_p,R)dr_p}=3\frac{\rho_d(R)}{a_e(R)}. \tag{4.20}$$

This redefinition differs from the classical definition of Ansmann and Müller (2005) in that the backscatter efficiency Q_B is included in the denominator. Main advantage of this redefinition is that allows the formulation of a lidar-to-passive collector relationship.

Dividing Eqs. (4.19) and (4.15) and carrying out the operation, we obtain

$$V_d(R)=\frac{4T_f A_c}{3K}\overline{w_p}\eta_c\overline{r_{eff}}IS(R). \tag{4.21}$$

In order to simplify the above expression, the constant C is defined as

$$C=\frac{4T_f A_c}{3K}, \tag{4.22}$$

from which the following is obtained

$$V_d(R)=C\overline{w_p}\eta_c\overline{r_{eff}}IS(R). \tag{4.23}$$

The spray liquid volume deposited on a collector segment is related to the tracer mass m_t [kg] captured by this collector segment by

$$m_t(R)=V_d(R)\rho_{m,f}, \tag{4.24}$$

where $\overline{\rho_{m,f}}$ [kg/m^3] is the mean tracer concentration in the droplets which strike the collector.

Considering an integration time t_{int} in the test and substituting Eq. (4.23) in (4.24) the following is obtained

$$m_t(R)=C\overline{w_p}\eta_c\overline{\rho_{m,f}}\,\overline{r_{eff}}IS(R). \tag{4.25}$$

Equation (4.25) is presented as a theoretical model which allows the prediction of the tracer mass deposited on the nylon strings from the backscattered lidar signal integrated over a time t_{int} ($IS(R)$) and the physical parameters ($\overline{w_p}$, η_c, $\overline{\rho_{m,f}}$, $\overline{r_{eff}}$) which define the drift cloud when it reaches the sampling point. The model assumes time-invariant particle distribution, tracer concentration, efficiency and wind speed over the integration time of each spatial observation at a range R.

The parameters related to the droplets deposited on the sampling point are unknown. This is because the size distribution (and tracer concentration) of the airborne droplets are modified as a result of evaporation and sedimentation mechanisms. However, it can be considered that these unknown parameters are related to other variables that are known, as: $\rho_{m,i}$ [kg/m^3] initial tracer concentration in the tank and $\overline{d_{wsp}}$ [m] mean diameter of the impacts on the water-sensitive paper. Based on these concentrations, the tracer mass captured by a collector segment can be expressed as

$$m_t(R) = C'\overline{w_p}\eta_c\rho_{m,i}\overline{d_{wsp}}IS(R), \tag{4.26}$$

where C' is the product of the constant C and the factors which would relate $\rho_{m,i}$ to $\overline{\rho_{m,f}}$ and $\overline{d_{wsp}}$ with $\overline{r_{eff}}$. These relationship factors do not have to be constants, though for purposes of simplicity they are considered as such in Eq. (4.26).

4.3 Materials and methods

4.3.1 General description of field tests

Ten spray tests were performed between September 18 and 21, 2009, at a field owned by the Institut de Recerca i Tecnologia Agroalimentàries (IRTA) in Gimenells (lat. 41º39'11''N, long. 0º23'28''E, elev. 259 m) located 25 km from Lleida, Spain. Figure 4.3 shows a map of the field as well as the position of the instruments and machinery used during the trials. The field is flat and lies next to a dirt road. At the time of the trials no crops were being grown on the field.

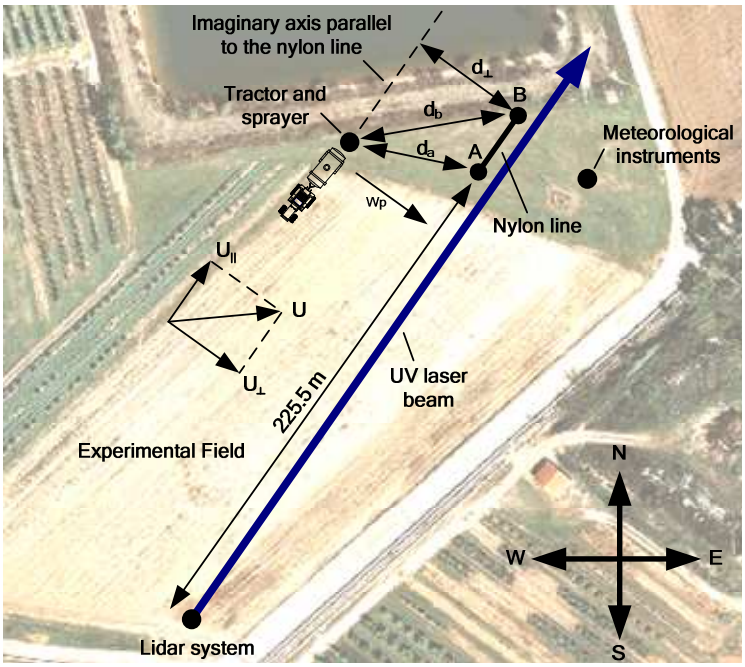

Fig. 4.3. Experimental field with sensor and operation locations. U is the wind speed and $U_\perp$ and $U_\parallel$ are, respectively, the wind components that are orthogonal and parallel to the nylon string. w_p is the component of the plume drift speed orthogonal to the nylon string.

The spray was generated by a cross-flow air-assisted sprayer (Ilemo Arrow F-1000, Ilemo/Hardi SA, Lleida, Spain) operating at 1 MPa. Three nozzle types were tested: 1) hollow cone (Albuz ATR Orange, Saint-Gobain, Evreux, France), 2) air injected anti-drift (Albuz TVI 80 02, Yellow), and 3) disc-core full cone nozzles (Teejet D3DC35, Spraying Systems Co., Wheaton, Illinois, USA). The use in each trial of different types and number of nozzles aims to increase the variability of application conditions. The sprayer was kept in a static position. The position of the sprayer was modified in the various tests depending on the wind direction in order to ensure that the plume drift would reach the collectors. The spray liquid comprised an aqueous solution of brilliant sulphoflavine (BSF, Biovalley, Marne La Vallée, France). This tracer was chosen because of its low solar degradation, high recovery rate, and its earlier successful use in previous experimental studies (Ganzelmeier et al., 1995; Solanelles et al., 2001).

Table 4.1 details the conditions of application of all the tests. For each test, the date the test was performed, the start time, the duration t_a of the spraying, the position of the hydropneumatic sprayer, the nozzle model employed, the number of open nozzles, the individual nozzle flow rate at a pressure of 1 MPa and the initial concentration, $\rho_{m,i}$, of BSF in the spray liquid, determined by fluorimetry of a sample taken from the tank are shown. The position of the sprayer is expressed with the terms d_a and d_b [m] which, as can be seen in Fig. 4.3, refer to the distances between the sprayer outlet and the posts A and B holding up the nylon string (described in Section 4.3.2). $d_\perp$ [m] is, as it can be seen in Fig. 4.3, the orthogonal distance between sprayer and string and is calculated from d_a and d_b.

Test	Date	Pulverization start time	t_a [s]	Sprayer position			Nozzles			$\rho_{m,i}$ [g/l]
				d_a [1] [m]	d_b [1] [m]	$d_\perp$ [1] [m]	Model	Number	Flow rate [l/min/ nozzle] [2]	
E1	9/18/09	14:44:40	40	26.85	37.45	26.84	Albuz ATR Orange	10	1.39	0.897
E2	9/18/09	16:01:10	34	26.85	37.45	26.84	Albuz ATR Orange	5	1.39	0.897
E3	9/20/09	13:29:30	30	27.95	32.95	27.12	Teejet D3DC35	10	2.0	0.907
E4	9/20/09	14:57:40	30	27.95	32.95	27.12	Teejet D3DC35	5	2.0	0.907
E5	9/20/09	16:21:30	30	27.95	32.95	27.12	Albuz TVI 80º Yellow	10	1.46	0.907
E6	9/21/09	11:36:40	30	26.30	37.55	26.27	Albuz TVI 80º Yellow	5	1.46	0.93
E7	9/21/09	14:50:07	30	26.30	37.55	26.27	Albuz ATR Orange	10	1.39	1
E8	9/21/09	15:08:44	30	26.30	37.55	26.27	Albuz TVI 80º Yellow	10	1.46	1
E9	9/21/09	16:47:11	33	22.90	44.70	16.24	Albuz ATR Orange	10	1.39	1
E10	9/21/09	17:06:13	31	22.90	44.70	16.24	Albuz ATR Orange	10	1.39	1

[1] d_a, d_b and $d_\perp$ refer to distances in Fig. 4.3. [2] Individual nozzle flow rate at an operating pressure of 1 MPa.

Table 4.1. Description of the experiments.

4.3.2 Passive collectors

Two types of collectors were used in each test: 2 mm diameter nylon string (reference drift collection system in ISO 22866 (2005)) 25.5 m long and 16 water-sensitive paper sheets 26×76 mm (Water-Sensitive Paper, Spraying Systems Co.). The nylon string was positioned horizontally 1.7 m above the ground and was held up at its two ends by posts which remained in

the same position throughout all the tests (A and B in Fig. 4.3). The water-sensitive paper sheets were attached to the nylon string with pegs (Fig. 4.4(a)), at a distance from each other of 1.5 m (Fig. 4.4 (b)) matching the range resolution of the lidar system (Table 4.2).

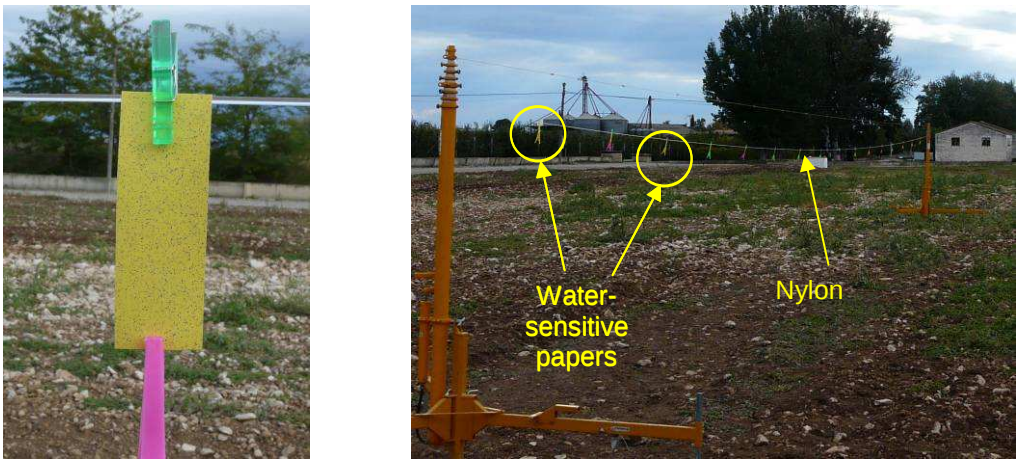

(a) **(b)**

Fig. 4.4. (a) Detail of a water-sensitive paper sheet attached by peg to the nylon string. (b) Nylon string with water-sensitive sheets attached each 1.5 m.

4.3.3 Lidar measurements

A 355-nm 16-mJ polarization lidar system (ALS 300, Leosphere, Orsay, France) was used for pesticide spray drift monitoring. Lidar system specifications (Leosphere, 2009) are listed in Table 4.2.

Wavelength, λ	354.7 nm (tripled Nd:YAG)
Pulse repetition frequency, *PRF*	20 Hz
Pulse energy, E_0	16 mJ (±5% pulse by pulse)
Laser emission divergence	< 0.25 mrad
Receiving diameter, d_0	150 mm
Interference filter width, $\Delta\lambda$	0.3 nm
Detector	Photomultiplier (PMT)
Range resolution, ΔR	1.5 m
Temporal Resolution, t_{int}	1 s (used in these tests)

Table 4.2. Lidar system specifications.

The lidar system was positioned in the southeast corner of the field 225.5 m from post A (Fig. 4.3). This distance ensured there would be no energy loss due to partial overlap (the range of full overlap was configured around 80 metres). As can be seen in Fig. 4.5, the lidar was pointed horizontally with its laser beam aligned with the nylon string. This was done to enable comparison of the measurements obtained by both sensors. The alignment was achieved thanks to the fluorescent effect which is produced when the UV beam strikes a moving cardboard

target. It should be mentioned that in all the tests the separation between laser beam and nylon string was less than 30 cm.

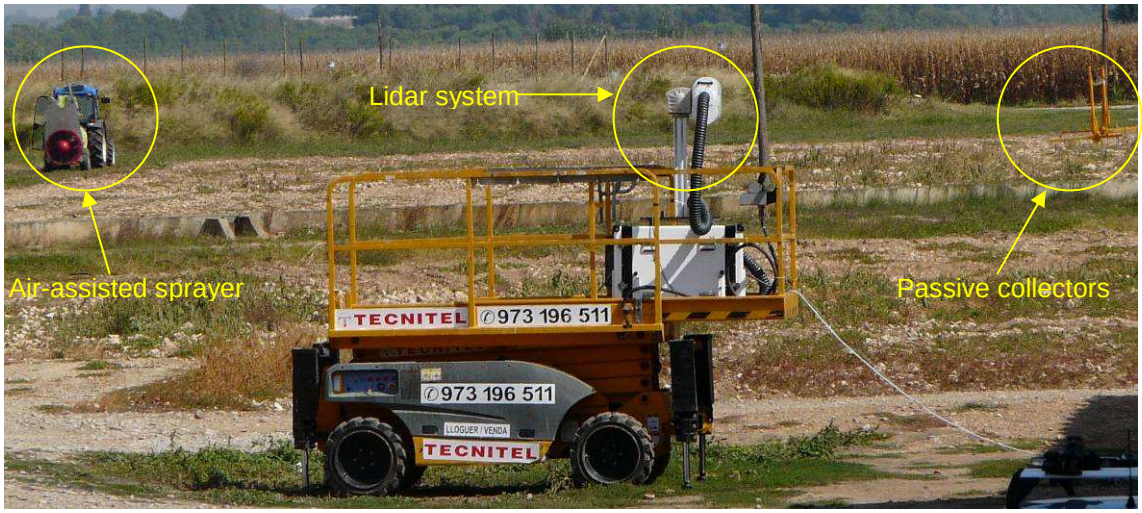

Fig. 4.5. Relative position of the lidar system (foreground), posts holding up the nylon string (right-hand side background) and the hydropneumatic sprayer (left-hand side background).

4.3.4 Meteorological measurements

A portable weather station was used equipped with a temperature and humidity sensor (EE20 Series, E+E Electronik Ges.m.b.H., Engerwitzdorf, Austria) and a pyranometer (SKS 1110, Skype, Powys, UK). The portable station was positioned at a height of 4 m and took one measurement each minute. The streamwise (u), cross-stream (v) and vertical (w) wind components were measured by a 3-axis ultrasonic anemometer (WindMaster, Gill Instruments Ltd, Lymington, UK) at an output rate of 10 Hz. The anemometer was also positioned at a height of 4 m.

Test	Temperature [ºC]	Relative Humidity [%]	Solar radiation [W/m^2]	$U_{\parallel}$ [m/s]	$U_{\perp}$ [m/s]	U [m/s]
E1	16.5	75	199	2.235	2.427	3.299
E2	17.7	65	183	0.919	1.430	1.700
E3	22.4	45	714	1.022	1.494	1.810
E4	23.5	45	452	0.191	0.967	0.986
E5	24.2	44	166	-0.558	0.863	1.028
E6	21.5	54	690	0.540	2.495	2.553
E7	25	39	529	N/A	N/A	N/A
E8	24.9	36	457	N/A	N/A	N/A
E9	25.1	36	142	1.821	0.762	1.974
E10	24.8	39	71	1.083	1.177	1.599

$U_{\parallel}$ is the wind component parallel to the nylon string (positive when it moves away from the lidar system), $U_{\perp}$ is the wind component perpendicular to the nylon string, and U is the wind speed modulus. *N/A* stands for not available.

Table 4.3. Meteorological conditions during the tests.

Table 4.3 shows the prevailing micrometeorological conditions during the performance of the tests. Temperature, relative humidity and solar radiation measurements were provided by the portable weather station and correspond to the minute in which the spraying was carried out. The wind speed U was calculated from three components (u,v,w) measured by the sonic anemometer and by averaging the resulting vector during the 60 s after the start of the spraying operation. A 60 s averaging period was chosen bearing in mind that the lidar system did not detect a signal after this time in any of the tests due to drift. The parallel $U_{\parallel}$ and cross $U_{\perp}$ wind components with respect to the nylon string, whose orientation during the tests was known, were calculated from the averaged wind speed and direction values.

4.3.5 Estimation of drift deposition on passive collectors

Nylon strings

Once the nylon string had been impregnated with the spray liquid it was cut in all the tests into 1.5 m long segments, corresponding to the range resolution of the lidar system used (Table 4.2). Each segment was placed in a plastic bag for its transfer to the laboratory where 50 ml of deionised water were added to each bag for tracer extraction (BSF). Determination of BSF concentration was carried out directly from the bags using a fluorescence spectrophotometer (LS 30 Luminescence Spectrometer, Perkin Elmer, Waltham, Massachusetts, USA) at a wavelength of 425 nm for excitation and 510 nm for emission. The total BSF mass deposited on each 1.5 m long collector segment was calculated by applying

$$m_t = \rho_t V_w, \tag{4.27}$$

where m_t [g] is the BSF mass on each collector segment, ρ_t [g/l] is the concentration of BSF in the water extract and V_w is the water volume used in the extraction (0.05 l).

Water-sensitive papers

Water-sensitive papers (*WSP*) were photographed at the laboratory and these images were analysed with specific software (Matrox Inspector, version 2.2, MatroxTM, Dorval, Canada) following the methodology described by Chueca et al. (2010). The images were taken with 20 pixels/mm resolution. Objects in the image comprising one single pixel were considered as noise and thus removed. Therefore, impacts less than $2.5 \cdot 10^{-3}$ mm^2 were not detected. In each image, the program measured coverage (percentage of surface covered by all the objects present in the image) and the area of all the objects (deposited droplets) and assessed their size, which was assumed to be the diameter of a circle having the same area as the object. Finally it calculated the average diameter.

Because WSP are much easier to handle and analyse than nylon strings, it is also important to assess whether they can be used as appropriate collectors in field experiments. For this reason, the relationship between total BSF-deposited mass, m_t, and coverage (%) of water-sensitive papers (WSP_{cov}) was studied using Simple Regression Analysis (SRA).

4.3.6 Estimation of the mean cross-plume velocity

Lidar data were used to obtain range-time intensity plots (RTI) of the pesticide plume and to calculate the time-integrated lidar signal. To generate RTI plots, lidar data was range-corrected and background subtracted. To obtain the background signal, time-averaged measurements were used in each test taken a few seconds before the start of the spraying operation (pre-calibration measurements). In some tests, measurements were also used taken after spray application, once the signal due to the pesticide plume had completely disappeared (post-calibration measurements). All the measurements have a time resolution of 1 s (Table 4.2).

Estimation of the mean cross-plume velocity, $\overline{w_p}$ in Section 4.2.2, was carried out from RTI plots. $\overline{w_p}$ is an estimation of the component of the speed of the pesticide cloud orthogonal to the direction of the nylon string (Fig. 4.3). For each RTI plot the time t_m [s] corresponding to the mid-point of the cloud is calculated and it is assumed that at this time half of the spraying has been performed (Fig. 4.7). The value of t_m is given by

$$t_m = t_i + \frac{t_f - t_i}{2} \quad , \tag{4.28}$$

where t_i [s] is the time elapsed between the start of the spraying operation and the moment when the plume begins to be detected by the lidar and t_f [s] is the time elapsed between the start of the spraying and the time instant when the plume ceases to be detected by the lidar.

The mean cross-plume velocity $\overline{w_p}$ is computed as

$$\overline{w_p} = \frac{d_\perp}{t_m - \frac{t_a}{2}}, \tag{4.29}$$

where $d_\perp$ [m] (Fig. 4.3) is the orthogonal distance between sprayer and nylon string and t_a [s] is the duration of the application. Substituting Eq. (4.28) in (4.29) the following is obtained

$$\overline{w_p} = \frac{2 \cdot d_\perp}{t_i + t_f - t_a}. \tag{4.30}$$

The values of the orthogonal distance $d_\perp$ and the duration of the spray application t_a are shown in Table 4.1, while t_i and t_f are determined from the RTI plots (Table 4.5).

4.3.7 Calculation of the time-integrated lidar signal

The time-integrated lidar signal $IS(R)$ was calculated adding together the range-corrected background subtracted lidar data throughout all the measurement period. The accumulated (not averaged) lidar signal is obtained with distance resolution, suitable for comparison with passive collector data. All lidar signal processing was performed using numerical computing software (Matlab® version 7.3, MathWorks Inc., Natick, Massachusetts, USA).

4.3.8 Study of the proposed model

The models proposed in Section 4.2.3 were studied using the test results. This study was divided into two parts:

1) Using Eq. (4.25), Simple Regression Analysis (SRA) is applied to analyse whether there exists a linear relationship (coefficient of determination R^2) between the time-integrated lidar signal, IS, and the BSF mass, m_t, deposited on each nylon string segment.

2) Multiple Regression Analysis (MRA) was used to study the consistency of the theoretical model of Eq. (4.26), which relates the tracer mass, m_t, with the observed time-integrated lidar signal, IS, the mean cross-plume velocity, $\overline{w_p}$, the initial tracer concentration $\rho_{m,i}$ in the spray tank and the average diameter $\overline{d_{wsp}}$ of the impacts on the WSP.

It is assumed that the efficiency of the collector, η_c, included in Eq. (4.26), takes a constant value since the same type of collector was used in all the tests. So, the tracer mass, m_t, deposited on the nylon strings is expressed by

$$m_t = C\overline{w_p}\eta_c\overline{\rho_{m,f}}\,\overline{r_{eff}}IS = f(IS, \overline{w_p}, \rho_{m,i}, \overline{d_{wsp}}), \tag{4.31}$$

where, for notational simplicity, distance dependency is not indicated.

In this study, MRA models were iteratively generated starting with a complete model with all the variables and removing the less significant variables (higher p-value) in each step, until the model was left with only significant variables ($p-value < 0.05$).

In all MRA studies described here, normal probability plots and Shapiro-Wilk tests (1965) were used to check the assumption of the normality of errors. All calculations were carried out with commercial statistical software (Statgraphics® Plus version 5.1, StatPoint Technologies Inc., Warrenton, Virginia, USA).

4.4 Results

4.4.1 Relationship between nylon string and WSP measurements

In this section a comparison is made of the data obtained with both passive collector types. It should be remembered that the nylon strings provide information about the amount of spray liquid (tracer) that reaches them while the water-sensitive paper sheets offer descriptive information about how this spray liquid was deposited. Moreover, since the nylon string catches 1.5 m of the spray plume and the WSP only represents a very small point along this length, it is expected that the nylon string will obtain more drift information than the WSP. Given the above, Eq. (4.32) describes the relationship between tracer mass, m_t [µg], collected for each nylon string segment and the coverage on water-sensitive paper sheets WSP_{cov} (percentage of the total surface covered by the strikes), with a coefficient of determination $R^2 = 0.90$

($p-value<0.0001$) (Table 4.4). See Navidi (2006) for a description of the statistical indicators presented in this section.

$$m_t = 0.934 + 1.889 WSP_{cov} \tag{4.32}$$

Figure 4.6 shows that the relationship between both variables can be considered linear. The model shows a strong dependency between WSP and nylon string data and admits the possibility of substituting nylon strings with simpler to handle and analyse WSP collectors in future field works. This relationship also allows comparison with previous studies carried out with any of these collectors.

Parameter	Estimate	Standard Error	$p-value$
Constant	0.934	0.307	0.0028
W_{cov}	1.889	0.050	<0.0001

Table 4.4. Regression coefficients of the SRA equation for tracer mass m_t as a function of the coverage on WSP ($R^2 = 0.90$).

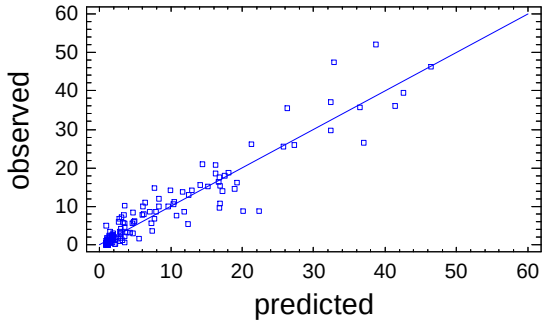

Fig. 4.6. Measured versus SRA model-predicted tracer mass values, m_t [µg], Eq. (4.32).

4.4.2 Range-time evolution of the spray drift

Figure 4.7 shows the RTI plots of the pesticide plumes corresponding to four of the tests that were performed (E2, E6, E7 and E8). The plume behaviour in the remaining trials is analogous to that shown in this figure. The backscattered lidar signal with parallel polarisation (left) and the cross-polarised lidar signal (right) are represented for each test. In all cases a high correlation between both signals can be noted.

Test	E1	E2	E3	E4	E5	E6	E7	E8	E9	E10
t_i **[s]**	8	10	N/A	24	17	6	13	22	11	8
t_f **[s]**	67	51	N/A	57	41	37	53	49	53	52
$\overline{w_p}$ **[m/s]**	1.534	1.988	N/A	1.064	1.937	4.042	1.459	1.281	1.048	1.120

Table 4.5. Cloud detection start time t_i, cloud detection end time t_f and mean cross-plume velocity $\overline{w_p}$ during the tests.

Table 4.5 shows the values obtained for the plume velocity, as well as the detection start and end times with the lidar. It can be seen that in almost all the tests, $\overline{w_p}$ differs from the

orthogonal wind component $U_{\perp}$ (Table 4.3). It is considered that this is because, on the one hand, the plume velocity is not only dependant on the wind speed but is also influenced by the sprayer fan, the droplet output pressure, friction between these two elements and the air, etc., and on the other because, due to atmospheric turbulence and the short duration of the tests, wind speed measurement at the anemometer position may not coincide with the real values in the position of the drift cloud.

4.4.3 Consistency of the proposed model (I): Time-integrated measurements

This section aims to validate the Eq. (4.25) model. A comparison is made in Fig. 4.8 for the same tests as in Fig. 4.7 of the backscattered signal received by the lidar system with the measurements taken with the passive collectors. The left-hand column shows as a function of range the lidar signal integrated in time S_i, in both channels (parallel-polarisation and cross-polarisation), the tracer mass m_t deposited on the nylon string and the percentage of coverage, WSP_{cov}, of the water-sensitive paper sheets. A clear linear relationship can be observed between the lidar-based measurements and the passive collector measurements. It should be remembered that the passive collectors only measured the drift for distances ranging between 225.5 and 251 m, which is where the support posts were positioned (Fig. 4.3). This entails a disadvantage with respect to the lidar system which enables monitoring of the whole pesticide plume. This can be clearly seen in Fig. 4.8(d), where the passive collectors are only able to detect a small fraction of the plume while the peak of the plume is detected at around 200 m by the lidar system.

The right-hand column of Fig. 4.8 shows for each test the measurement of the tracer mass m_t deposited on each nylon string segment (1.5 m) versus the time-integrated lidar signal IS (parallel polarised channel) corresponding to the same segment. A high linear correlation can be observed in all the tests between both variables (coefficient of determination $R^2 \approx 0.90$) in accordance with the linear formulation – in first approximation – proposed by the model of Eq. (4.25). In the remaining tests, not represented in Fig. 4.8, similar correlations have been obtained. The theoretical relation between passive collector captured tracer mass and the integrated lidar signal is, according to Eq. (4.25), a function of 4 parameters ($\overline{w_p}$, η_c, $\overline{\rho_{m,f}}$, $\overline{r_{eff}}$) which depend on the weather and application conditions. For a given test, the average meteorological conditions to which the drift droplets which reach the different collector segments are subjected to will be very similar, while the application conditions are the same.

Therefore, the spray drift radii distribution $\overline{r_{eff}}$, the mean cross-plume velocity $\overline{w_p}$, the final concentration of tracer $\overline{\rho_{m,f}}$ and the collector efficiency η_c are spatially and time invariant on a given test experiment. So, Eq. (4.25) can be rewritten in a simplified form as

$$m_t(R) = CK_t IS(R), \tag{4.33}$$

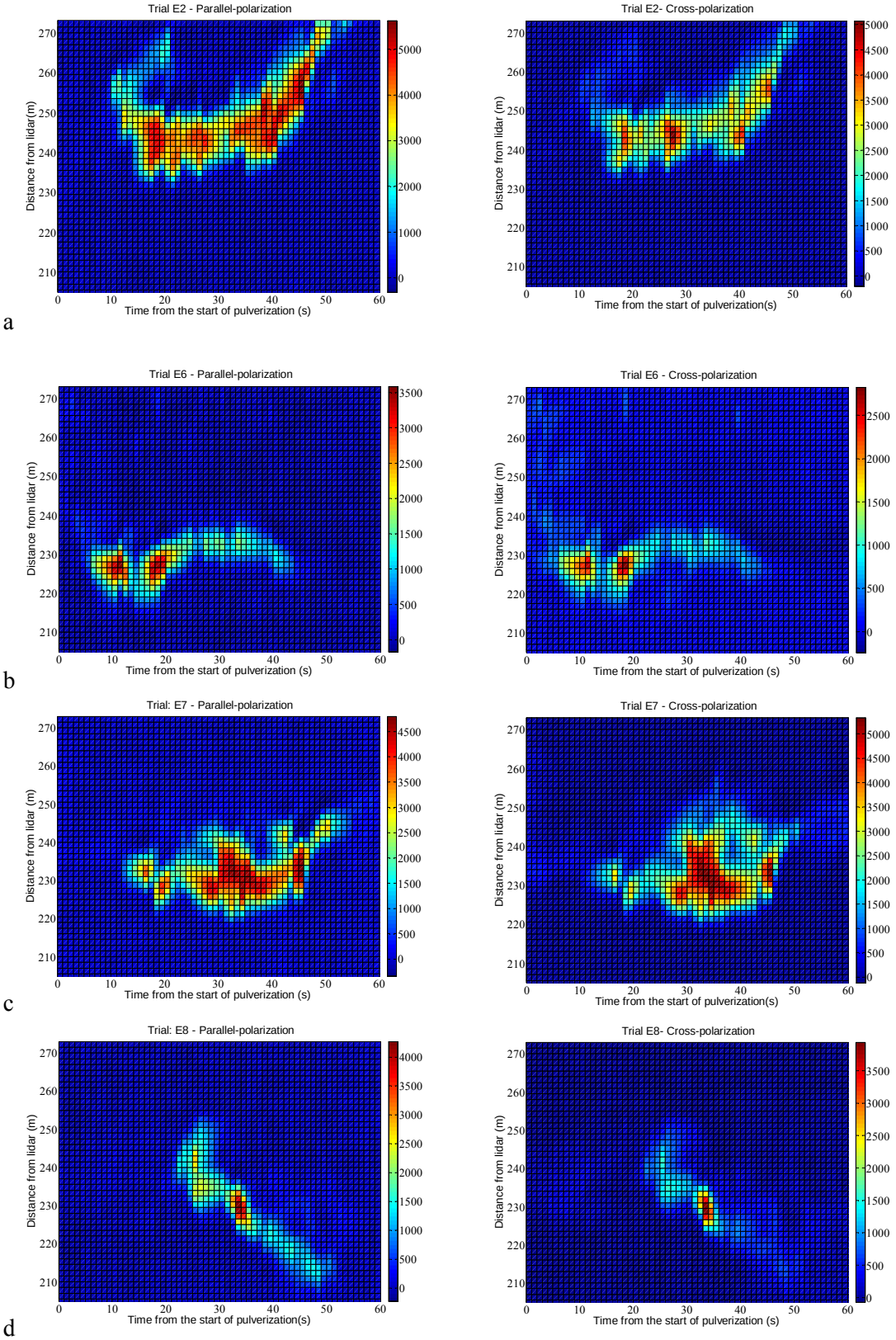

Fig. 4.7. Range-corrected background-subtracted lidar signal (arbitrary units) for the parallel-polarized channel (left) and for the cross-polarized channel (right). Temporal resolution is 1 s and range resolution is 1.5 m. (a) Test E2. (b) Test E6. (c) Test E7. (d) Test E8.

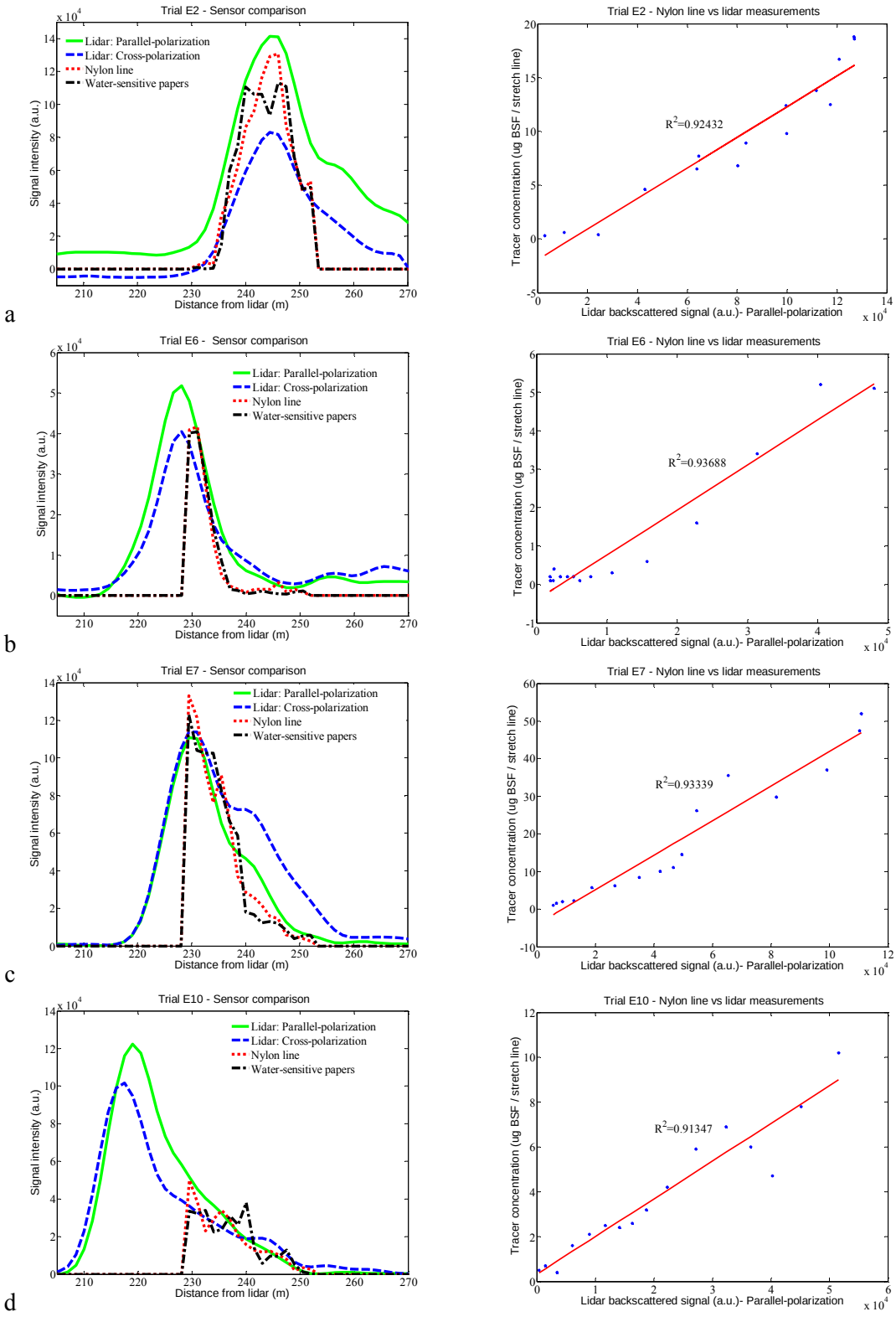

Fig. 4.8. (left) Range profiles of time-integrated lidar signals (parallel and cross-polarized channels), tracer mass captured by nylon strings and spray coverage on the water-sensitive papers. All units are arbitrary and plots are scaled for representation purposes. (right) Tracer mass [µg] deposited on each nylon string segment vs backscattered lidar signal in parallel polarised channel. (a) Test E2. (b) Test E6. (c) Test E7. (d) Test E10.

where K_t is the characteristic constant of the test given by the meteorological and application conditions of that test and is defined as

$$K_t = \overline{w_p}\,\eta_c\,\overline{\rho_{m,f}}\,\overline{r_{eff}}\,. \tag{4.34}$$

It is deduced from Eq. (4.33) that for a given test there exists a linear relationship between the tracer mass deposited on the different nylon string segments and the corresponding time-integrated lidar measurements. This theoretical relationship concurs with the test results shown in Fig. 4.8 (right).

4.4.4 Consistency of the proposed model (II): MR Analysis

This section aims to validate Eq. (4.26) considering together the results of all the tests. Equation (4.35) shows the relationship between the deposited tracer mass m_t [µg] and the product of the variables time-integrated lidar signal IS [10^{-4} Vm^2], mean cross-plume velocity $\overline{w_p}$ [m/s], initial tracer concentration $\rho_{m,i}$ [g/l] and mean impact diameter $\overline{d_{wsp}}$ [µm] with a coefficient of determination $R^2 = 0.64$ ($p - value < 0.0001$).

$$m_t = 0.411 + 7.783 \cdot 10^{-6}\,\overline{w_p}\,\rho_{m,i}\,\overline{d_{wsp}}\,IS \tag{4.35}$$

MRA showed a significant influence on m_t of the product of the variables IS, $\overline{w_p}$, $\rho_{m,i}$ and $\overline{d_{wsp}}$, since the coefficient of this product is statistically significant (Table 4.6).

Parameter	Estimate	Standard Error	$p - value$
Constant	0.411	0.641	0.522
$\overline{w_p}\rho_i\overline{d_{wsp}}S_i$	$7.783 \cdot 10^{-6}$	$0.491 \cdot 10^{-3}$	<0.0001

Table 4.6. Regression coefficients of the multiple regression equation for tracer mass m_t as a function of the product between the time-integrated lidar signal IS, the plume velocity $\overline{w_p}$, the initial tracer concentration in the spray liquid $\rho_{m,i}$ and the mean impact diameter $\overline{d_{wsp}}$ ($R^2 = 0.64$).

The plot of the observed versus predicted values shows that the points are mostly symmetrically distributed around a straight line (Fig. 4.9).

Using linear regression analysis of the deposited tracer mass m_t and each of the variables IS, $\overline{w_p}$, $\rho_{m,i}$ and $\overline{d_{wsp}}$, it is clear that the correlation in Eq. (4.35) is basically due to the existence of a strong relationship between m_t and the time-integrated lidar signal IS (coefficient of determination $R^2 = 0.67$).

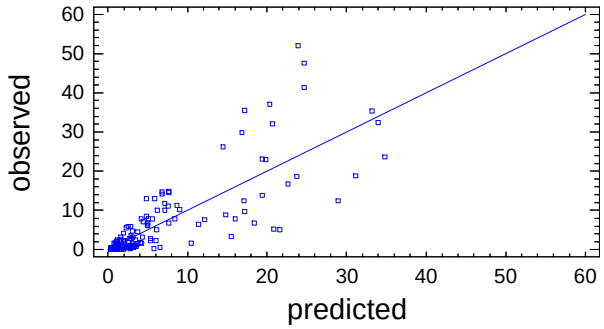

Fig. 4.9. Plot of the observed versus predicted values of the multiple regression model for tracer mass m_t as a function of the product between the time-integrated lidar signal IS, the plume velocity $\overline{w_p}$, the initial tracer concentration in the spray liquid $\rho_{m,i}$ and the mean impact diameter $\overline{d_{wsp}}$.

In view of these results a conclusion cannot be drawn about the consistency of the model presented in Eq. (4.26). A greater number of tests would be required for model validation, increasing the range of values which the independent variables take. By way of example, it can be seen that $\overline{w_p}$ takes similar values in all the tests analysed (Table 4.5). Also, the error that is introduced on considering a linear relationship between the initial, $\rho_{m,i}$, and final, $\overline{\rho_{m,f}}$, tracer concentrations, and between the mean impact diameter on the WSP, $\overline{d_{wsp}}$, and the effective droplet radius, $\overline{r_{eff}}$, is not known. So, it would be necessary to measure the parameters $\overline{\rho_{m,f}}$ and $\overline{r_{eff}}$ to validate the model.

4.5 Conclusions

In this chapter it has been shown that the lidar is an appropriate technique for measuring the pesticide drift as it has been possible to relate the lidar measurements to those obtained via conventional sampling techniques. The advantages of the lidar system have been highlighted in terms of their monitoring capacity (range and time-resolved information in RTI plots) and the lower amount of time required. Additionally, the lidar system enables estimation of the plume speed, and its comparison with the anemometer measured wind speed.

It has been shown that exists a strong linear correlation ($R^2 \approx 0.90$) for each of the tests between the lidar measurements and those obtained with the passive collectors. In accordance with Eq. (4.25), this is due to the fact that $\overline{r_{eff}}$, $\overline{w_p}$, $\overline{\rho_{m,f}}$ and η_c are spatially and time-invariant for a given trial experiment. When the meteorological or application conditions vary, these parameters cannot be considered invariant. This explains why, when jointly processing the results of all the tests, the correlation between the lidar signal and the measurements of the collectors is appreciably lower ($R^2 = 0.67$). Validation of the proposed model would require further testing in the future under contrasting conditions and measurement of all the independent variables that affect the model.

5

Design of a specific lidar system for spray drift measurement

Chapter 4 demonstrated experimentally the feasibility of using an elastic backscatter lidar system to measure pesticide drift. Unlike *in-situ* measurement techniques, lidar systems allow remote and real-time monitoring of a pesticide plume, attaining a high distance resolution. Despite these advantages, the fact that no lidar instrument suitable for such an application is presently available has appreciably limited its practical use.

The design of a specific lidar system for the monitoring of pesticide clouds is presented in this chapter. Firstly, a detailed description is given of the specifications that such an instrument must satisfy. An assessment is then made of the eye safety level required for the different wavelengths under consideration. In the following section, the principal design parameters including wavelength, pulse energy, reception area, etc., are established via simulation. The chapter continues by presenting the different components that will comprise the emitter and receiver. Finally, a summary is provided of the experimental tasks that have been performed so far and future lines of work that will need to be undertaken are discussed.

5.1 Initial design specifications

Currently existing lidar systems are instruments designed for the tropospheric study of the atmosphere and their configuration is little suited for drift measurement, as was concluded in Chapters 2 and 4. There is therefore a clear need for the development of a new lidar system designed for pesticide drift monitoring. Details are given below of the design specifications which, following the author's criteria, such an instrument needs to satisfy. To a large extent, these specifications are the consequence of the experience acquired during the experimental campaign which was presented in Chapter 4. Design specifications:

- Compact and economic system. An easily transportable instrument suitable for field work is required.

- Near-field and distance resolution measurement capabilities. The system to be developed should allow monitoring of drift plumes generated by ground sprayers. These clouds have relatively low dimensions, commonly just a few metres thick. For appropriate characterisation, the lidar system must have a high range resolution, not greater than 1 m. A maximum reach of 500 m is considered sufficient.

- Scanning and temporal resolution capabilities. Pesticide plumes are highly dynamic (due to meteorological factors, applied spraying technology, etc.), with rapid variations in their shape and concentration. In order to characterise these clouds, the lidar system must be capable of complete scans of them at high frequencies. It was experimentally shown in Chapter 4 that a time resolution of 1 s (complete 2D scan) is suitable for the monitoring of plumes resulting from ground-based spray applications.

- Eye safety. The drift clouds generated by ground-based applications are usually suspended at a low height above the sprayed crop. Miller et al. (2003) scanned the spray drift at several heights (from 3 to 20 m) above an orange orchard using an elastic backscatter mini-lidar. They found that most of the plume was near the canopy top and only a little was at 18 m above the canopy. Therefore, monitoring pesticide drift with terrestrial lidar systems implies a quasi-horizontal sounding, increasing the risk of accidentally impinge on bystanders. It is therefore concluded that the instrument must be eye-safe (class I).

5.2 Maximum permissible exposure for different wavelengths

Wavelength is one of the key parameters in the design of any lidar system. Dependant on this parameter are the laser emitters and photodetectors that can be used, the mechanisms of interaction with the atmosphere and the eye safety level that will be required. As the design

starting-point, a comparative analysis will be conducted in this section of the maximum permissible exposure (MPE) to the following wavelengths:

- $\lambda = 355$ nm. Typical of UV lidars (Gimmestad et al., 2003), corresponding to the third harmonic of the Nd:YAG solid state laser.
- $\lambda = 523$ nm. Visible radiation used by the Micro Pulse Lidar (Spinhirne, 1993).
- $\lambda = 905$ nm. Commonly applied in lidar ceilometry (Gregorio et al., 2012), corresponding to the InGaAs laser diode.
- $\lambda = 1064$ nm. IR radiation (Rocadenbosch et al., 2001) generated by the Nd:YAG laser (fundamental frequency).
- $\lambda = 1550$ nm. Used in eye safe systems (Mayor and Spuler, 2004).

5.2.1 Interaction of laser radiation with biological tissue

The eyes and the skin are the organs that are most susceptible to laser radiation damage (Henderson and Schulmeister, 2004). A summary is provided in Table 5.1 of the principal pathologies caused by excessive exposure to light.

Spectral region	Eye	Skin
Ultraviolet C (180-280 nm)	Photokeratitis	Erythema (sunburn) Skin aging Increased pigmentation
Ultraviolet B (280-315 nm)		
Ultraviolet A (315-400 nm)	Photochemical cataract	Pigment darkening Photosensitive reactions Skin burn
Visible (400-780 nm)	Photochemical and thermal retinal damage	
Infrared A (780-1400 nm)	Cataract, retinal burn	Skin burn
Infrared B (1.4-3.0 µm)	Aqueous flare, cataract, corneal burn	
Infrared C (3.0 µm-1 mm)	Only corneal burn	

Table 5.1. Pathological effects associated with excessive exposure to light. Adapted from IEC 60825 (2007).

Details are given below of the mechanisms of interaction with biological tissue for each of the spectral ranges considered in this study.

Near ultraviolet (UV-A): 315-400 nm

UV-A radiation incident on the human eye is absorbed mainly by the lens, to the extent that only a small fraction reaches the retina. Skin and eye safety levels are similar and much higher than for visible and near infrared light. However, photons in the UV-A region are very energetic and can generate photochemical alterations at molecular or atomic level and initiate adverse biological processes: skin erythemas, photochemical cataracts, DNA alterations and long-term effects (premature skin aging, skin cancer). These doses are additive in periods of less than 24 hours and so the duration that needs to be considered will be equal to the total exposure time,

bearing in mind that for repeated exposure on successive days the permitted daily limit (10 $kJ \cdot m^{-2}$) will have to be reduced by a factor of 2.5 (ICNIRP, 1996).

Visible (VIS): 400-780 nm

Sensitivity of the eye to visible light is high and the main danger lies in retinal damage, with thermal mechanisms predominating when the exposure is for less than 10 s and photochemical mechanisms for more prolonged exposures. A light aversion time (palpebral reflex) of 0.25 s is used to determine the MPE level (ICNIRP, 1996).

Near Infrared (IR-A): 780-1400 nm

Thermal effects predominate in the near infrared regardless of the duration of the exposure and, as with visible light, the main danger is retinal damage. There is no palpebral response in this spectral band and exposure duration of 10 s is considered for computing purposes, taking into account the protection given by natural eye movement (ICNIRP, 1996). For these wavelengths, if the source is an extended one (as opposed to a point source) and in accordance with IEC 60825 (2007), a higher exposure duration time would be taken of 100 s. However, this increase in exposure time will not result in more restrictive limits since the extended source hypothesis relaxes the MPE thresholds. In this study, the more conservative hypothesis is assumed, consisting of point source and exposure duration equal to 10 s.

Middle Infrared (IR-B): 1.4-3 µm

The ocular medium is opaque to IR-B radiation which therefore does not reach the retina. The main danger to the eye is corneal damage due to thermal or thermomechanical mechanisms. For these wavelengths, the MPE level for the skin is similar to that for the eye when the radiation is incident on areas smaller than 0.01 m^2. However, for larger areas and when the duration of the exposure extends beyond 10 s, there is a decrease in the permissible exposure limit. Following IEC 60825 (2007), to calculate the MPE an exposure time of 10 s is considered and the most restrictive criterion is assumed corresponding to incidence areas larger than 0.1 m^2.

5.2.2 Single pulse exposure

The MPE corresponding to a pulsed laser source must not exceed the most restrictive of the criteria that appear in this section (exposure to a single pulse) and Section 5.2.3 (pulse train exposure). The laser in this study is considered as a point source (conservative hypothesis), defined by IEC 60825 (2007) as a source in which the subtended angle is less than 1.5 mrad.

Table 5.2 shows the MPE values corresponding to a single pulse (MPE_{single}) for the wavelengths under consideration. Standard lidar pulse durations are assumed, ranging between 1 and 100 ns. For UV radiation, the MPE_{single} value depends on the pulse duration (τ_l). Otherwise, for the remaining wavelengths, the maximum exposure takes constant values.

λ	355 nm	523 nm	905 nm	1064 nm	1550 nm
MPE_{single} [J·m^{-2}]	$5600 \cdot \tau_l^{\,0.25}$	0.005	0.01285	0.050	10000

Table 5.2. Maximum Permissible Exposure of a single pulse (MPE_{single}) for the studied wavelength.

5.2.3 Pulse train exposure

The MPE for a pulse train is determined on the basis of the most restrictive of the following criteria:

Criterion 1

Exposure to a pulse train over a time T must not exceed the MPE level corresponding to a single pulse of the same duration.

The MPE value for a pulse train (MPE_T) is averaged by the number of pulses emitted ($N = T \cdot PRF$) over the time T , enabling comparison with the radiant exposure due to a single pulse.

$$MPE_{single,mean} = \frac{MPE_T}{T \cdot PRF}, \tag{5.1}$$

where $MPE_{single,mean}$ [J·m^{-2}] is the maximum permissible exposure for a single pulse in a pulse train, MPE_T [J·m^{-2}] is the maximum permissible exposure for an exposure duration T [s] and PRF [Hz] is the pulse repetition frequency.

Table 5.3 shows, for the different wavelengths under consideration in this study, the different expressions for calculating the maximum permissible exposure for a single pulse in a pulse train ($MPE_{single,mean}$). These expressions are obtained from Eq. (5.1), taking the MPE_T values set out in IEC 60825 (2007) for exposure durations of time T considered in Section 5.2.1. As expected, in all cases the $MPE_{single,mean}$ value is inversely proportional to the emission frequency (PRF) of the laser source. As stated in Section 5.2.1, for $\lambda = 355$ nm the duration T will be equal to the total time of the exposure.

λ	355 nm	523 nm	905 nm	1064 nm	1550 nm
$MPE_{single,mean}$ [J·m^{-2}]	$\frac{10000}{T \cdot PRF}$ for $T \geq 10$ s	$\frac{25.5}{PRF}$	$\frac{25.7}{PRF}$	$\frac{50}{PRF}$	$\frac{100}{PRF}$

Table 5.3. MPE of a single pulse in a train of pulses for the studied wavelength (criterion 1).

Criterion 2

For wavelengths longer than 400 nm (retinal risk zone), the radiant exposure of each pulse cannot exceed the MPE value corresponding to a single pulse (Section 5.2.2) multiplied by a correction factor $N^{-0.25}$, being N the number of pulses during the exposure time T .

Table 5.4 shows the expressions which allow calculation of the MPE values corresponding to this criterion. To obtain these expressions the same exposure durations T as in criterion 1 and standard lidar system repetition frequencies (PRF) are considered.

According to IEC 60825 (2007), for $\lambda = 1550\,\text{nm}$ the number of pulses N is calculated by counting as a single pulse all those pulses which appear within a period $T_i = 10$ s. The MPE level of T_i is divided by the real number of pulses in this period to obtain MPE_{train}, a value which can be compared to the radiant exposure of the individual pulse.

λ	≤400 nm	532 nm	905 nm	1064 nm	1550 nm
MPE_{train} [J·m^{-2}]	This criterion does not apply	$\frac{0.005}{(0.25\cdot PRF)^{0.25}}$ for $PRF < 55$ kHz	$\frac{0.01285}{(10\cdot PRF)^{0.25}}$ for $PRF < 55$ kHz	$\frac{0.050}{(10\cdot PRF)^{0.25}}$ for $PRF < 20$ kHz	$\frac{1000}{PRF}$ for $PRF < 0.1$ Hz

Table 5.4. MPE of a single pulse in a train of pulses for the studied wavelength (criterion 2).

5.2.4 Maximum permissible exposure for a pulsed laser

Figure 5.1 shows the maximum permissible exposure for a single pulse as a function of the pulse repetition frequency. This graph was generated considering for each wavelength and emission frequency the most restrictive of the criteria presented in Tables 5.2, 5.3 and 5.4.

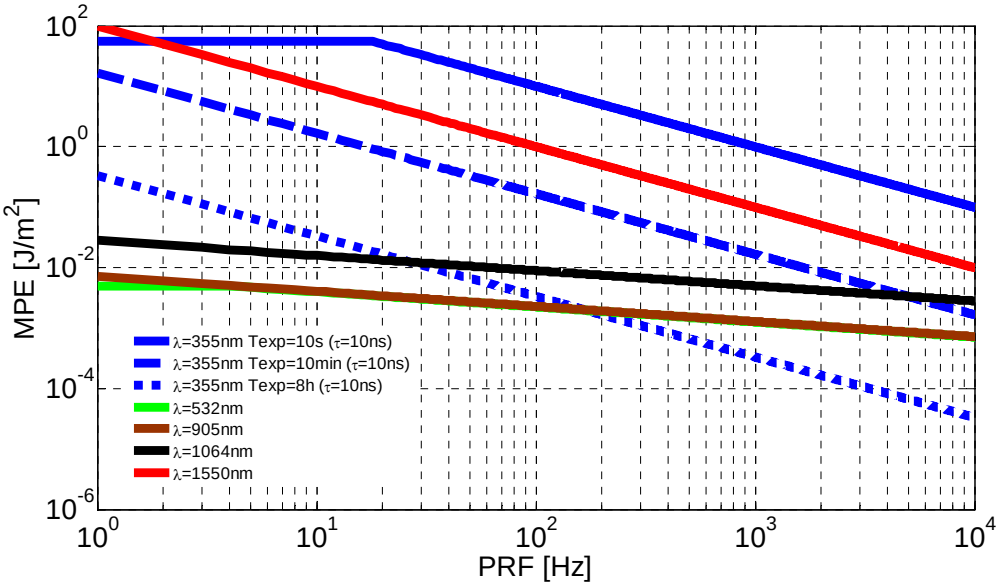

Fig. 5.1. MPE for an individual pulse vs pulse repetition frequency (PRF).

It can be seen that at 355 nm the safety level varies substantially with the exposure time. So, for exposures of 10 s this is the safest wavelength, whereas for more prolonged exposures (and high

PRFs) it is one of the most dangerous. As explained in Section 5.2.1, this behaviour is due to the UV-A radiation doses being additive.

At 532 and 905 nm the MPEs are very similar, while for 1064 nm the safety threshold is approximately twice as high. The 1550 nm wavelength is known to be eye-safe, though this condition depends on the emitted radiant exposure. In Fig. 5.1 it can be seen that at 1550 nm, permissible exposure is appreciably higher than in the visible or near infrared. In addition, unlike in the ultraviolet, there are no additive photochemical effects in the IR-B.

5.3 Performance assessment

In this section, the interval of values is determined in which the system constant K_s must be found to satisfy the initial specification of pesticide cloud measurement at a distance of 500 m.

For this purpose, simulations of the signal-to-noise ratio (SNR) were conducted for three wavelengths: 905, 1064 and 1550 nm. Emission at 355 nm was not considered since, as was seen in Section 5.2, the doses are additive in the UV-A region and consequently the safety level falls drastically for prolonged exposures. Another drawback of UV-A radiation is that it requires special optical material, since optical glass is not transparent and molecular backscatter in the ultraviolet range is very high (Gimmestad and Roberts, 2004). Emission at 523 nm was also disregarded as it has MPE values similar to at 905 nm (Section 5.2.4), but at this latter wavelength solar radiation (background noise) and atmospheric extinction are lower.

5.3.1 Atmospheric model

As explained in Section 5.1, the lidar system sounding of the atmosphere will be horizontal and so a homogenous atmospheric model is considered in the SNR simulations. Clear atmospheric conditions are assumed in this model (15 km visibility) and, as in Section 3.3 (Eq. 3.1 and 3.2), the total extinction and backscatter coefficients, α^{tot} and β^{tot} respectively, are obtained as the sum of the components due to aerosols (α^{aer}, β^{aer}) and molecules (α^{mol}, β^{mol}). The calculation of each of these components is given below.

Molecular (Rayleigh) opto-atmospheric parameters

The molecular extinction coefficients at different wavelengths are obtained by applying the following expression,

$$\alpha^{mol}(\lambda) = \left(\frac{550}{\lambda[nm]} \right)^4 \alpha^{mol}_{550}, \tag{5.2}$$

where $\alpha_{550}^{mol} = 0.0116 \ \ km^{-1}$ is the molecular extinction at 550 nm (Collis and Russell, 1976).

The molecular backscatter coefficient is a constant multiple of the coefficient of extinction and is given by the relationship,

$$\beta^{mol} = \frac{3}{8\pi}\alpha^{mol}. \tag{5.3}$$

Particulate (Mie) opto-atmospheric parameters

With known atmospheric visibility V_M [km], the Mie extinction coefficient α_{550}^{aer} [km^{-1}] at 550 nm is calculated by applying Koschmieder's equation (1924),

$$\alpha_{550}^{aer} = \frac{3.91}{V_M}. \tag{5.4}$$

At different wavelengths, extinction due to aerosols is given by,

$$\alpha^{aer} = \alpha_{550}^{aer}\left(\frac{550}{\lambda[nm]}\right)^{1.3}. \tag{5.5}$$

As can be seen in Fig. 5.2, the Mie backscatter coefficient β_{550}^{aer} [$km^{-1}sr^{-1}$] at 550 nm is a known value for different atmospheric visibility conditions. At other wavelengths, the backscatter coefficient is calculated by applying,

$$\beta^{aer} = \beta_{550}^{aer}\frac{550}{\lambda[nm]}. \tag{5.6}$$

Total opto-atmospheric parameters

Table 5.5 gives, for each of the wavelengths under consideration, the total coefficients of atmospheric extinction α^{tot} and backscatter β^{tot}, calculated through Eqs. (5.2-5.6). The values of the diffuse component of solar radiation L_b (Measures, 1992) are also shown.

λ	905 nm	1064 nm	1550 nm	Spray drift cloud (Fig. 5.2)
α^{tot} [km^{-1}]	0.138	0.111	0.068	10
β^{tot} [$km^{-1}sr^{-1}$]	5.813×10^{-3}	4.883×10^{-3}	3.306×10^{-3}	0.5
L_b [$Wcm^{-2}nm^{-1}sr^{-1}$]	10^{-6}	4×10^{-7}	4×10^{-8}	-

Table 5.5. Opto-atmospheric parameters and solar background radiance for the studied wavelengths.

In the SNR simulations, the presence of a pesticide cloud located at 500 m is considered. In the few studies carried out in which lidar systems have been used to measure drift (Section 2.3.1), the author has been unable to find extinction coefficient values α^{cloud} or backscatter coefficient

values β^{cloud} which are characteristic of this type of cloud. For this reason, standard values for light-water clouds ($\alpha^{cloud} = 10\ \mathrm{km}^{-1}$, $\beta^{cloud} = 0.5\ \mathrm{km}^{-1}\mathrm{sr}^{-1}$, Fig. 5.2) have been used in this study, this being a conservative approximation.

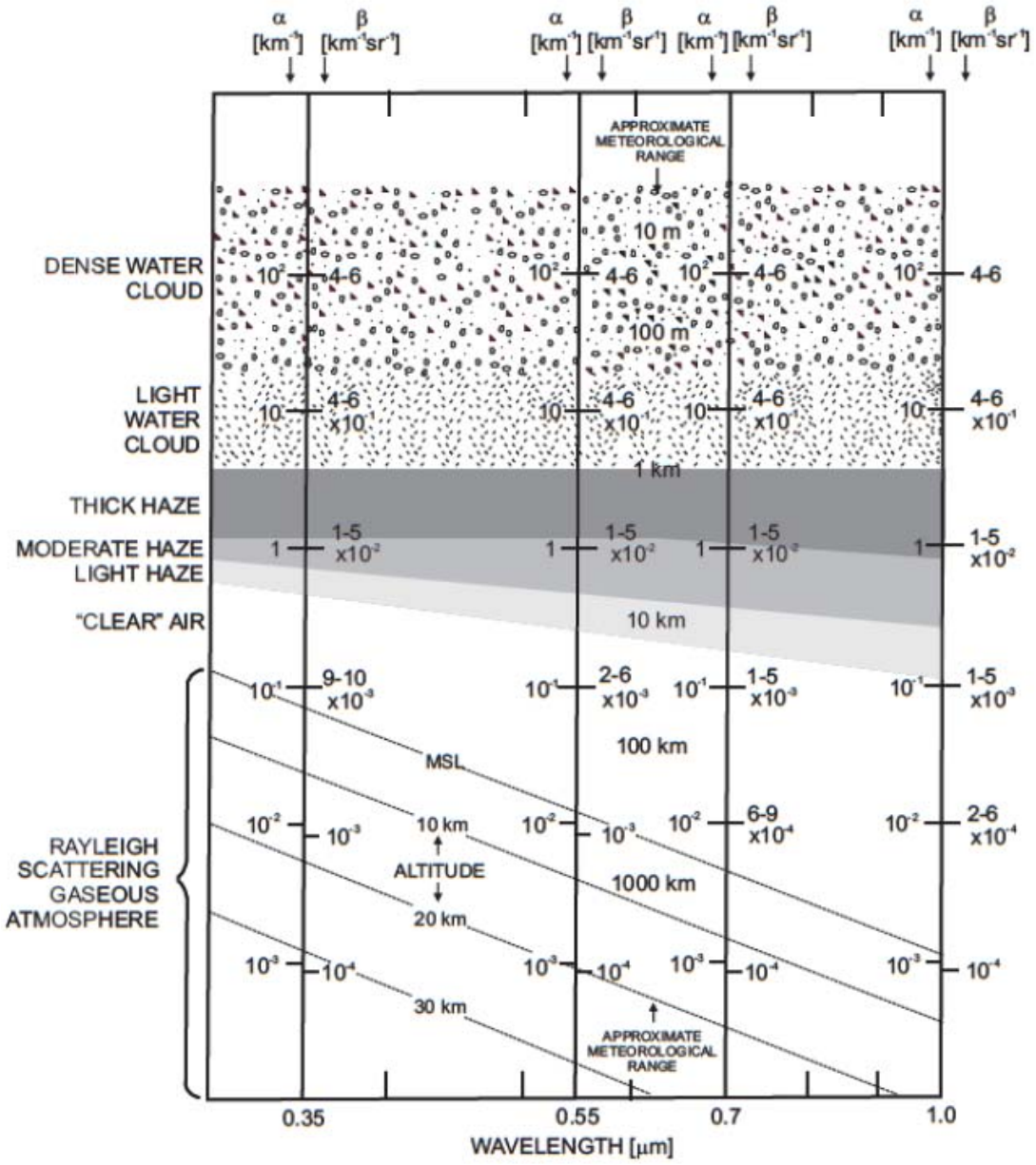

Fig. 5.2. Variation of extinction and backscattering coefficients with wavelength and atmospheric conditions (Collis and Russell, 1976).

5.3.2 Signal-to-noise ratio

A study is undertaken in the simulations of how the SNR varies with the system constant K_s [Wm^3]. The aim is to find the values of K_s which allow SNRs higher than 5 to be reached, the threshold which is considered sufficient for the application of automatic detection algorithms (Morille et al., 2007).

Since the lidar system must be capable of high frequency scanning (Section 5.1), performing pulse integration is not feasible unlike with the ceilometer (Eqs. 3.14 and 3.15). The required SNR values must be obtained with a single pulse.

The expression corresponding to a single pulse SNR was deduced in Section 3.3.1 (Eq. 3.13) and is reproduced here to aid the reader's understanding (Rocadenbosch et al., 1998).

$$SNR(R) = \frac{\xi_0 K_s U_s(R)}{\left[\frac{2qF}{R_{io}}\left(K_s U_s(R) + K_b L_b\right)\xi_0 + NEP_m^2\right]^{1/2} B_N^{1/2}}, \tag{5.7}$$

where K_s [W·m^{-3}] (Eq. 3.9) is the system constant, K_b [m^2·nm·sr] (Eq. 3.11) is the background-radiance system constant, $U_s(R)$ [m^{-3}] is the backscattered signal from range R [m] as defined by Eq. 3.8, ξ_0 is the optics transmission factor, R_{io} [A/W] is the photoreceiver current intrinsic responsivity, q [C] is the electron charge, F is the excess noise factor, NEP_m [W/Hz$^{1/2}$] is the noise equivalent power of the photoreceiver module, and B_N [Hz] is the equivalent noise bandwidth at reception.

5.3.3 Signal-to-noise ratio simulations at 905 nm

In the SNR simulations which are presented below, various photodetector types have been considered and the value of the transmission factor ξ_0 and of the background-radiance system constant K_b has been tuned, as shown in the variants of Table 5.6.

Variant number	Photodetector	R_{io} [A/W]	M	F	NEP_m [pW/$\sqrt{\text{Hz}}$]	ξ_0	K_b [m^2·nm·sr]	Required K_s [Wm^3]
1	Silicon APD	0.62	100	4	0.105	0.5	$6.17\cdot10^{-9}$	16.33
2	Silicon APD	0.62	100	4	0.105	0.25	$6.17\cdot10^{-9}$	32.65
3	Silicon APD	0.62	100	4	0.105	0.1	$6.17\cdot10^{-9}$	81.58
4	Silicon PIN	0.62	1	1	10.484	0.5	$6.17\cdot10^{-9}$	852.3
5	Silicon PIN	0.62	1	1	10.484	0.25	$6.17\cdot10^{-9}$	1705
6	Silicon PIN	0.62	1	1	10.484	0.1	$6.17\cdot10^{-9}$	4261
7	Silicon APD	0.62	100	4	0.105	0.5	$6.17\cdot10^{-6}$	28.9
8	Silicon APD	0.62	100	4	0.105	0.25	$6.17\cdot10^{-6}$	47.51
9	Silicon APD	0.62	100	4	0.105	0.1	$6.17\cdot10^{-6}$	98.89
10	Silicon PIN	0.62	1	1	10.484	0.5	$6.17\cdot10^{-6}$	852.3
11	Silicon PIN	0.62	1	1	10.484	0.25	$6.17\cdot10^{-6}$	1705
12	Silicon PIN	0.62	1	1	10.484	0.1	$6.17\cdot10^{-6}$	4261

Table 5.6. Required system constant for various parameters at 905 nm.

Photodetector modules considered

At wavelengths of 905 and 1064 nm there are three photodetector options: silicon PIN photodiodes, silicon avalanche photodiodes (APD) and photomultiplier tubes (PMT). In this design it was decided to use photodiodes given their superior quantum efficiency in comparison with PMTs.

A PIN photodetector module and an APD module were considered in the simulations that were performed. Both modules are comprised of a photodiode and transimpedance amplifier (TIA), with the latter being the element which limits the bandwidth B_N of the receiver. The specified distance resolution $\Delta R \leq 1m$ (Section 5.1) requires a bandwidth greater than 107 MHz, a value which is obtained when applying Eq. (2.11). In this calculation, a pulse duration $\tau_l \leq 2ns$ is assumed and a detection time given by $\tau_d = 1/2B_N$, where B_N is the noise-equivalent bandwidth in reception. In a photodiode-based (APD/PIN) optoelectronic receiving chain, B_N is the transimpedance amplifier (TIA) bandwidth because its bandwidth is much smaller than that of the photodiode (typically, a few GHz). At the receiver output, the signal must be sampled at a frequency, $f_s \geq 2B_N$ according to Nyquist's criterion (that is, $f_s \geq 215$ MHz considering the example figures given).

It is assumed that both receiver modules are comprised of a TIA with a bandwidth of 200 MHz and an input noise current $i_T = 6.5$ pA/$\sqrt{\text{Hz}}$. These specifications are similar to those of model 313A of Analog Modules (2002).

For the APD receiver module, intrinsic responsivity $R_{io} = 0.64$ A/W at 905 nm and a gain $M = 100$ are considered, values similar to the Perkin Elmer C30955EH model (2008). An excess noise factor $F = 4$ is estimated, with application of the empirical formula $F = M^n$, where $n = 0.3$ is the excess noise index for an Si-APD (Perkin Elmer, 2010). A noise equivalent power NEP_m of 0.105 pW/$\sqrt{\text{Hz}}$ is assumed for the APD module. This value is obtained from the equation (Kovalev and Eichinger, 2004),

$$NEP_m = \frac{i_{Noise}}{M \cdot R_{io}}, \tag{5.8}$$

where i_{Noise} [pA/$\sqrt{\text{Hz}}$] is the total input noise-current spectral density. The transimpedance amplifier nearly always generates much more noise than the photosensitive diode and, therefore, the approximation $i_{Noise} \approx i_T$ has been considered.

Intrinsic responsivity $R_{io} = 0.64$ A/W at 905 nm is also considered for the PIN module. In this case, there is no gain ($M = 1$) and so the excess noise factor is $F = 1$. The noise equivalent power is 10.484 pW/$\sqrt{\text{Hz}}$, a value calculated through Eq. (5.8).

Considered configurations of the system

Three values for the transmission factor were simulated, corresponding to high ($\xi_0 = 0.5$), moderate ($\xi_0 = 0.25$) and low ($\xi_0 = 0.1$) optical transmissivity.

For the background-radiance system constant K_b, values of $6.17 \cdot 10^{-9}$ and $6.17 \cdot 10^{-6}$ $m^2 \cdot nm \cdot sr$ are assumed. These parameters were calculated by applying Eq. (3.11), taking, respectively, reception diameters of 100 and 50 mm, fields of vision of 5 and 1 mrad and interference filter widths of 10 and 1 nm.

Simulation results

In Fig. 5.3, the signal-to-noise ratio is simulated as a function of the system constant K_s considering a background-radiance system constant K_b of $6.17 \cdot 10^{-9}$ $m^2 \cdot nm \cdot sr$ (variants 1 to 6 in Table 5.6). It can be seen that when using an APD module (in red, Fig. 5.3), it is possible to achieve an SNR of 5 with system constants (K_s between 16.33 and 81.58 Wm^3 in Table 5.6) two orders of magnitude lower than those required when using a PIN module (K_s between 852.3 and 4261 Wm^3 in Table 5.6).

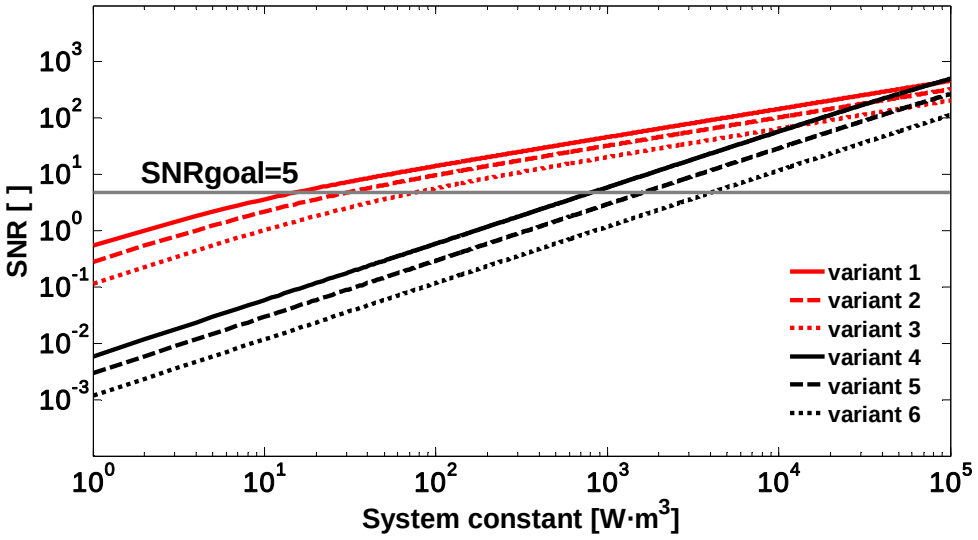

Fig. 5.3. SNR vs system constant due to a drift cloud located at 500 m for variants 1 to 6 (Table 5.6).

The simulations in Fig. 5.4 correspond to a background-radiance system constant K_b of $6.17 \cdot 10^{-6}$ $m^2 \cdot nm \cdot sr$ (variants 7 to 12 in Table 5.6). The increase in K_b means that a higher background radiation reaches the photodetector, so there is some deterioration of the SNR. Using the APD module, an SNR of 5 is achieved for K_s values ranging between 28.9 and 98.89 Wm^3 (Table 5.6). With the PIN, module values of K_s are obtained similar to in the case of $K_b = 6.17 \cdot 10^{-9}$ $m^2 \cdot nm \cdot sr$. This is due to the fact that with the PIN, the dark-shot and the thermal noise are dominant over the photo-induced signal noise.

So, at 905 nm and using an Si-APD module, the constant K_s of the system must take values between 16.33 and 98.89 Wm^3. As the system must be compact, assuming reception diameters d_0 of between 50 and 100 mm and applying Eq. (3.9), it is concluded that the required pulse energy must be between 14 and 336 μJ.

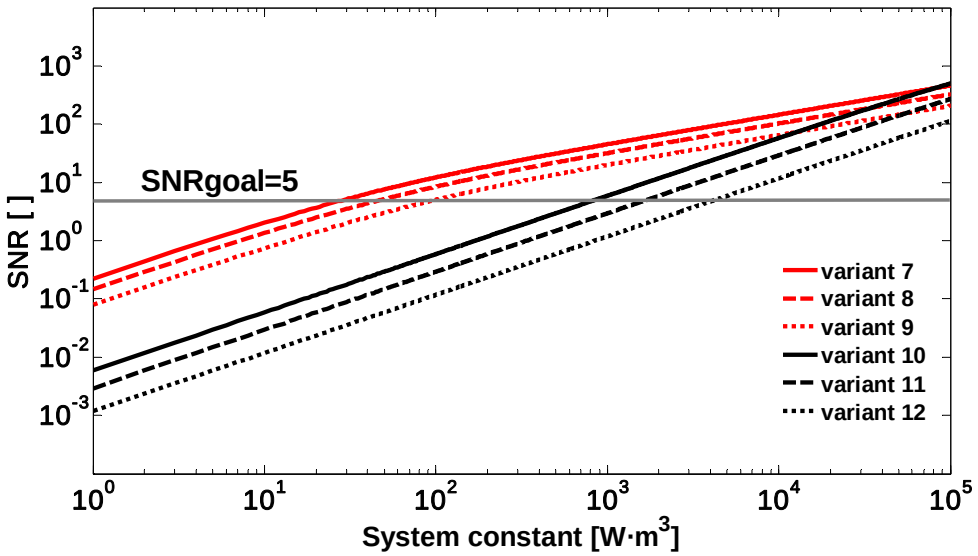

Fig. 5.4. SNR vs system constant due to a drift cloud located at 500 m for variants 7 to 12 (Table 5.6).

5.3.4 Signal-to-noise ratio simulations at 1064 nm

The same photodetector modules, transmission factors and background-radiance system constant as for the 905 nm simulations were considered in the simulations at 1064 nm. It should be noted that at 1064 nm, the intrinsic responsivity R_{io} of the photodiodes is 0.34 A/W (Perkin Elmer, 2008). Applying Eq. (5.8), a NEP_m of 0.191 and 19.118 pW/$\sqrt{\text{Hz}}$ is obtained for the APD and PIN modules, respectively.

Variant number	Photodetector	R_{io} [A/W]	M	F	NEP_m [pW/$\sqrt{\text{Hz}}$]	ξ_0	K_b [m²·nm·sr]	Required K_s [Wm³]
13	Silicon APD	0.34	100	4	0.191	0.5	$6.17\cdot10^{-9}$	28.95
14	Silicon APD	0.34	100	4	0.191	0.25	$6.17\cdot10^{-9}$	57.88
15	Silicon APD	0.34	100	4	0.191	0.1	$6.17\cdot10^{-9}$	144.7
16	Silicon PIN	0.34	1	1	19.118	0.5	$6.17\cdot10^{-9}$	1513
17	Silicon PIN	0.34	1	1	19.118	0.25	$6.17\cdot10^{-9}$	3027
18	Silicon PIN	0.34	1	1	19.118	0.1	$6.17\cdot10^{-9}$	7568
19	Silicon APD	0.34	100	4	0.191	0.5	$6.17\cdot10^{-6}$	35.62
20	Silicon APD	0.34	100	4	0.191	0.25	$6.17\cdot10^{-6}$	65.07
21	Silicon APD	0.34	100	4	0.191	0.1	$6.17\cdot10^{-6}$	152.3
22	Silicon PIN	0.34	1	1	19.118	0.5	$6.17\cdot10^{-6}$	1513
23	Silicon PIN	0.34	1	1	19.118	0.25	$6.17\cdot10^{-6}$	3027
24	Silicon PIN	0.34	1	1	19.118	0.1	$6.17\cdot10^{-6}$	7568

Table 5.7. Required system constant for various parameters at 1064 nm.

Figure 5.5 shows the signal-to-noise ratio versus the system constant for $K_b = 6.17 \cdot 10^{-9}$ m^2·nm·sr (variants 13 to 18 in Table 5.7). As at 905 nm, it can be seen that using APD modules system constants are required (K_s between 28.95 and 144.7 Wm^3 in Table 5.7) some two orders of magnitude lower than if a PIN module is applied (K_s between 1513 and 7568 Wm^3 in Table 5.7).

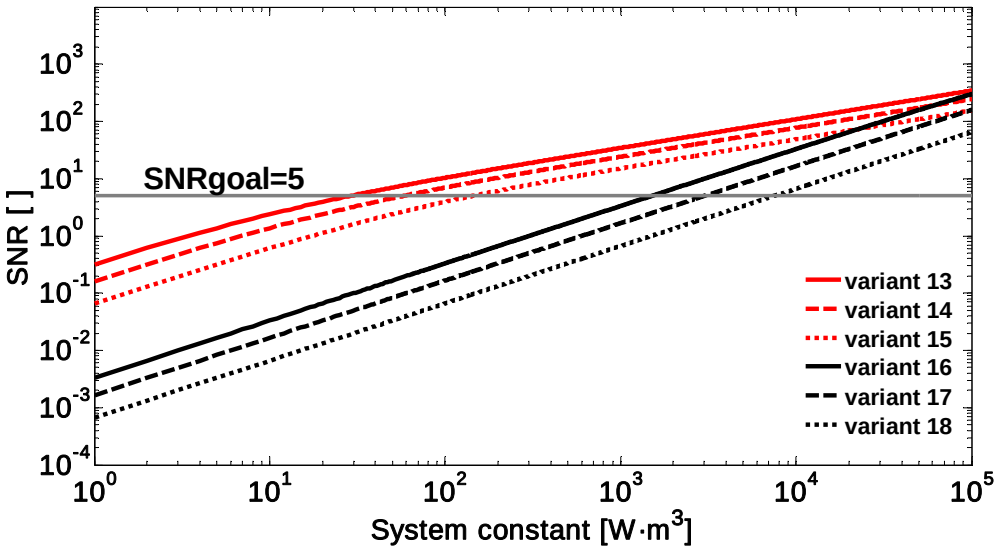

Fig. 5.5. SNR vs system constant due to a drift cloud located at 500 m for variants 13 to 18 (Table 5.7).

The simulations shown in Fig. 5.6 are analogous to those in Fig. 5.5, but considering $K_b = 6.17 \cdot 10^{-6}$ m^2·nm·sr (variants 19 to 24 in Table 5.7). As at 905 nm, when an APD module is used, as K_b increases higher values of K_s are required (between 35.62 and 152.3 Wm^3 in Table 5.7). In contrast, if a PIN module is used, the values of K_s do not vary.

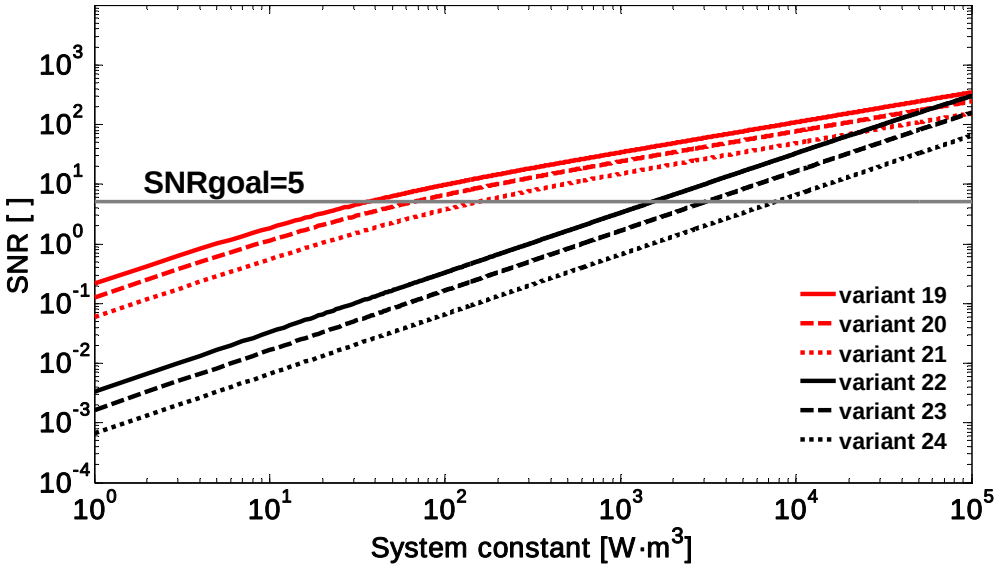

Fig. 5.6. SNR vs system constant due to a drift cloud located at 500 m for variants 19 to 24 (Table 5.7).

It is concluded that at a wavelength of 1064 nm a system constant is required between 1.2 and 1.8 times higher than for 905 nm. This is due to the fall in intrinsic responsivity of the silicon photodiodes, with a reduction in quantum efficiency from 85 to 40% (Perkin Elmer, 2008). Using an APD module, the constant of the system will have to be within the range of 28.95 and 144.7 Wm^3, which entails pulse energies (assuming $d_0 = 50 - 100$ mm) of between 25 and 492 μJ.

5.3.5 Signal-to-noise ratio simulations at 1550 nm

InGaAs or Germanium photodiodes are commonly used at 1550 nm. Though InGaAs photodiodes are more expensive, they have higher bandwidth and less noise than the Germanium type. In this section, an APD photodetector module and a PIN module are simulated, both based on InGaAs diodes.

Variant number	Photodetector	R_{io} [A/W]	M	F	NEP_m $\left[\text{pW}/\sqrt{\text{Hz}}\right]$	ξ_0	K_b [m^2·nm·sr]	Required K_s [Wm^3]
25	InGaAs APD	0.93	10	5.5	0.7	0.5	$6.17 \cdot 10^{-9}$	58.29
26	InGaAs APD	0.93	10	5.5	0.7	0.25	$6.17 \cdot 10^{-9}$	116.6
27	InGaAs APD	0.93	10	5.5	0.7	0.1	$6.17 \cdot 10^{-9}$	291.5
28	InGaAs PIN	0.93	1	1	7	0.5	$6.17 \cdot 10^{-9}$	530.7
29	InGaAs PIN	0.93	1	1	7	0.25	$6.17 \cdot 10^{-9}$	1061
30	InGaAs PIN	0.93	1	1	7	0.1	$6.17 \cdot 10^{-9}$	2654

Table 5.8. Required system constant for various parameters at 1550 nm.

Standard values of intrinsic responsivity $R_{io} = 0.93$ A/W, gain $M = 10$ and excess noise factor $F = 5.5$ (Perkin Elmer, 2010) are assumed for the APD module. The same intrinsic responsivity is assumed for the PIN module, but in this case there is no gain ($M = 1$) and so, $F = 1$. It is assumed that these photodetector modules incorporate a TIA with the same characteristics as those stated in Section 5.3.3 ($B_N = 200$ MHz, $i_T = 6.5$ pA/$\sqrt{\text{Hz}}$). Applying Eq. (5.8) a NEP_m of 0.7 and 7 pW/$\sqrt{\text{Hz}}$ is obtained for the APD and PIN modules, respectively.

Three optical transmissivity values are also considered: $\xi_0 = 0.5$, 0.25 and 0.1. However, unlike the simulations at 905 and 1064 nm, for 1550 nm the value of the background-radiance system constant will not be tuned. This is because the background radiation is very low and so modification of this constant does not significantly alter the signal-to-noise ratios obtained.

It can be seen in the simulations of Fig. 5.7 that with an APD module an SNR of 5 is achieved for values of K_s (between 58.29 and 291.5 Wm^3 in Table 5.8) one order of magnitude lower than when using a PIN module (K_s between 530.7 and 2654 Wm^3 in Table 5.8).

For a wavelength of 1550 nm and using InGaAs APD modules, system constants between 2 and 3.6 times higher are required when compared with the simulations at 905 nm. Assuming values of $d_0 = 50 - 100$ mm, it is concluded that the required pulse energies range between 50 and 1000 μJ.

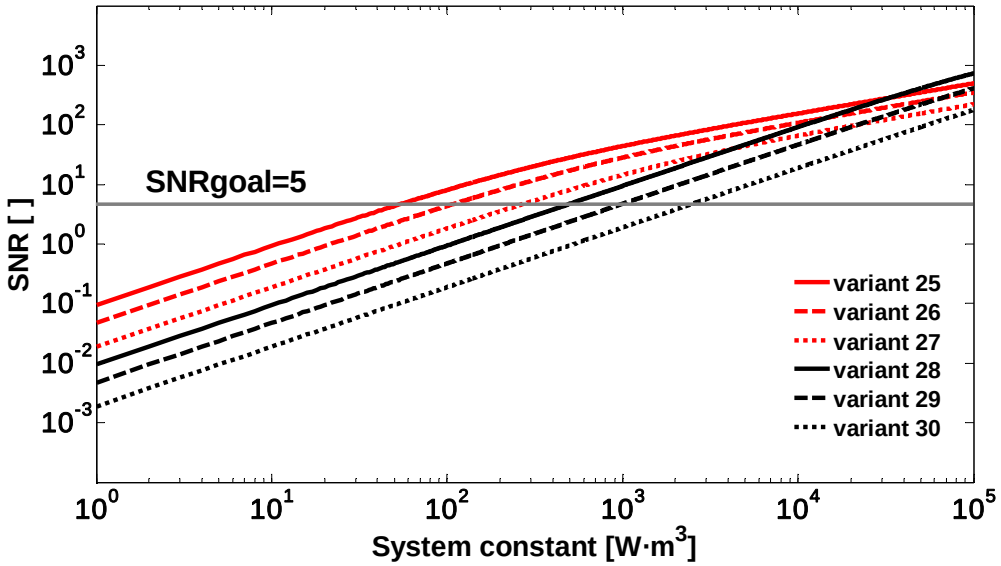

Fig. 5.7. SNR vs system constant due to a drift cloud located at 500 m for variants 25 to 30 (Table 5.8).

5.3.6 Selection of the wavelength

This section will determine for each wavelength what expansion of the laser beam is required for the system to be eye-safe. The starting point for this involves the pulse energy intervals calculated in Sections 5.3.3, 5.3.4 and 5.3.5, and the MPE levels presented in Section 5.2.

Wavelength	**905 nm**			**1064 nm**			**1550 nm**		
Pulse energy	**15 μJ**	**75 μJ**	**350 μJ**	**25 μJ**	**100 μJ**	**500 μJ**	**50 μJ**	**200 μJ**	**1 mJ**
100 Hz	91	204	442	60	120	268	8	16	36
1 kHz	122	273	589	80	160	357	25	50	113
10 kHz	163	364	785	106	213	476	80	160	357

Table 5.9. Required beam diameters (in mm) at several repetition rates for the studied wavelengths and pulse energies.

Figure 5.8 shows, for a wavelength of 905 nm, how the radiant exposure evolves with the laser beam diameter for different pulse energies within the interval of values (14-336 μJ) set out in Section 5.3.3. The horizontal lines represent the MPE levels for pulse repetition frequencies (PRF) of 0.1, 1 and 10 kHz.

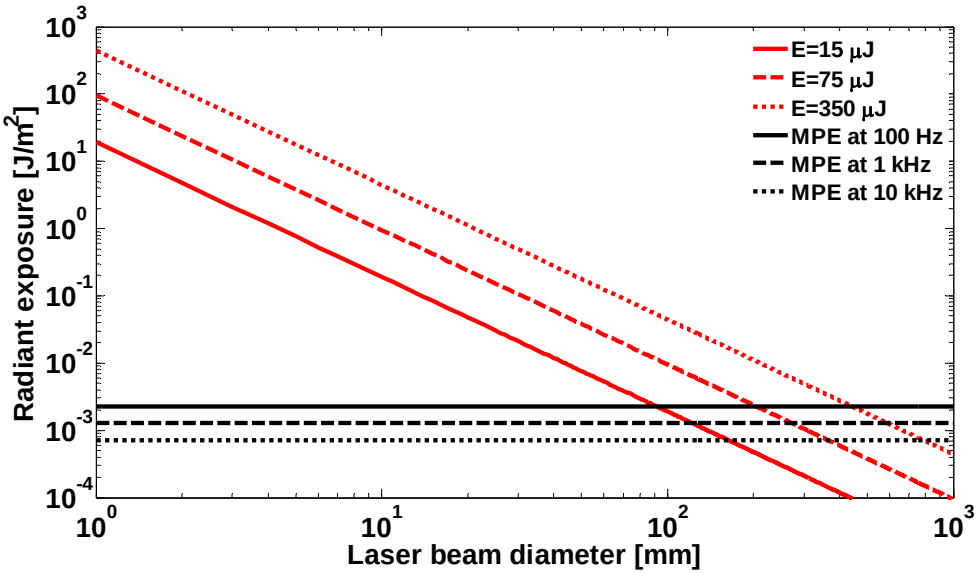

Fig. 5.8. Radiant exposure vs laser beam diameter for several pulse energy values. Horizontal lines represent MPE at a wavelength of 905 nm for various repetition rates.

The PRF values have been taken considering that, as specified in Section 5.1, the system must be capable of scanning pesticide plumes with a spatial and temporal resolution lower than 1 m and 1 s, respectively. Bearing in mind that the dimensions of the clouds to be monitored are typically in several tens of metres, a minimum PRF of 100 Hz is established. The higher the PRF, the higher the spatial and temporal resolution, though the eye safety level will be lowered. At 905 nm, except in the case of minimum energy and PRF (15 μJ, 100 Hz), eye safety is only achieved for beam expansions greater than 100 mm (Table 5.9).

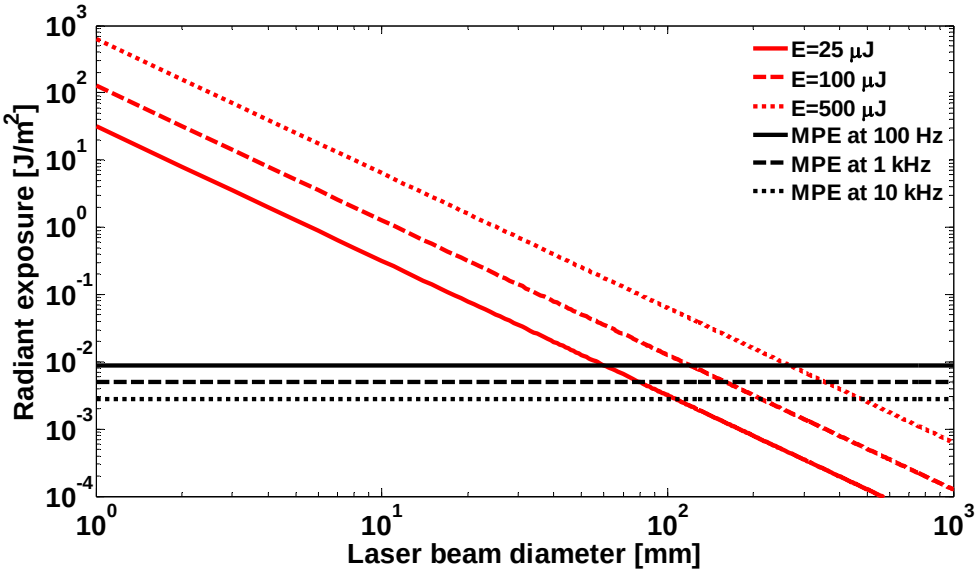

Fig. 5.9. Radiant exposure vs laser beam diameter for several pulse energy values. Horizontal lines represent MPE at a wavelength of 1064 nm for various repetition rates.

It can be seen in Fig. 5.9 that at 1064 nm the MPE values are reached with beam expansions slightly lower than those required at 905 nm. This is because of the higher eye safety level at this wavelength and despite the emission of higher pulse energies. At 1064 nm, beam diameters greater than 100 mm are required in all cases, except for low energy emissions and moderate PRF values (25 μJ and 0.1-1 kHz, Table 5.9).

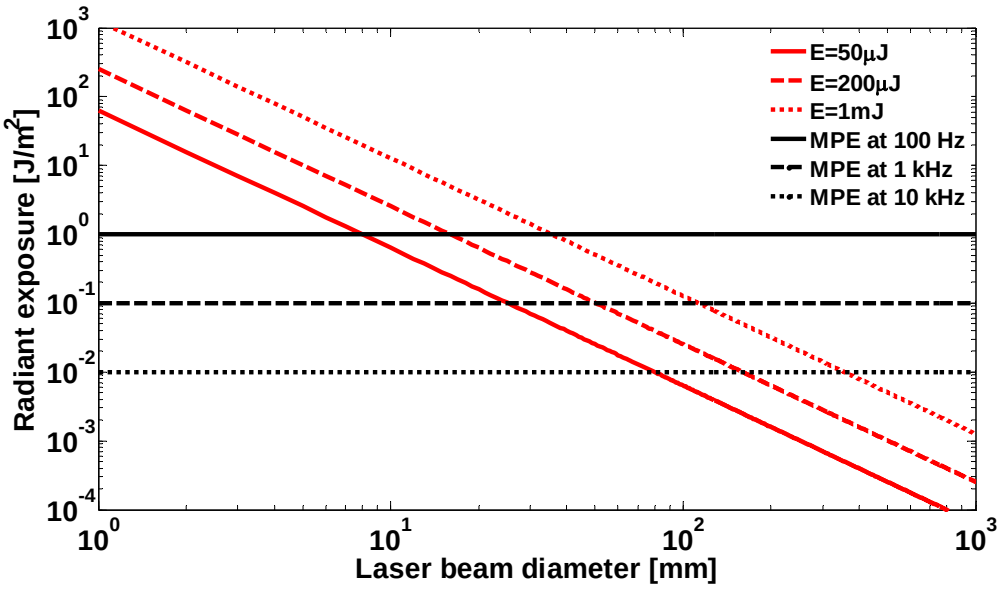

Fig. 5.10. Radiant exposure vs laser beam diameter for several pulse energy values. Horizontal lines represent MPE at a wavelength of 1550 nm for various repetition rates.

It can be seen in Fig. 5.10 that the beam expansions required at 1550 nm are significantly lower than those calculated for 905 and 1064 nm, especially when the PRFs are low or moderate. Table 5.9 shows that for PRF equal to 100 Hz, the eye-safety level is reached with beam diameters one order of magnitude lower, while at 1 kHz the required beam expansions are between 3 and 5 times lower. At 10 kHz, the required diameters are close to or greater than 100 mm, values similar to those obtained for 1064 nm.

Based on the above results, the chosen option was 1550 nm and repetition frequencies between 0.1 and 1 kHz. This allows emission of the required pulse energies, while at the same time meeting the compact design requirements specified initially. Apart from the advantages in terms of eye safety, at this wavelength background solar radiation is approximately one order of magnitude lower than at 1064 nm and the Rayleigh signal is small. One drawback that should be mentioned is that the InGaAs APDs available at 1550 nm have maximum diameters of just 200 μm. These small sizes limit the field of view and introduce greater demands on the optomechanical design. Despite this, 1550 nm wavelength emission constitutes, at the present time, one of the most promising alternatives for the development of eye-safe lidar systems (Gimmestad and Roberts, 2004).

5.4 Selection of components

The emitter and receiver subsystems of the microlidar are presented in this section. The different components were chosen on the basis of the parameters established in Section 5.3. It was decided with this prototype to opt for a biaxial configuration as, unlike a coaxial configuration, it does not require compensation systems for the internal optical cross talk, as was seen in Section 3.2.3.

5.4.1 Emitter subsystem

Laser sources at 1.5 µm

There are various options for generating pulsed laser energy at 1.5 µm: stimulated Raman scattering (SRS), optical parametric oscillators (OPO), erbium-doped glass lasers and InGaAsP laser diodes. While semiconductor diodes represent the simplest and most economical solution, their low power restricts their application to lidar ceilometers whose energy requirements are not very demanding (~1 µJ). Other drawbacks of laser diodes include their high divergence and low spectral purity.

Raman scattering has been used in several lidar systems to generate 1.5 µm radiation (Patterson et al., 1989; Carnuth and Trickl, 1994; Spinhirne et al., 1997; Mayor and Spuler, 2004). This method consists of passing Nd-YAG radiation through a cell containing methane or deuterium at high pressure to shift the 1.06 µm Nd-YAG output to 1.54 µm (Hecht, 2008). Using SRS, lidar pulse energies up to 225 mJ at 10 Hz of repetition rate have been achieved by Mayor et al. (2007). One of the drawbacks of such systems involves safety problems associated with the handling of high pressure cells.

Optical parametric oscillators (OPO) are based on the emission of a laser beam that is directed into a nonlinear crystal placed inside a resonant cavity. This interaction allows the conversion of light from a shorter to longer wavelength (Hecht, 2008). OPOs have been used by several authors as emission sources in eye-safe lidar systems (Harrell et al., 1995; Gong et al., 2007). In contrast with SRS techniques, OPO is a solid-state method which allows more compact designs and requires no handling of high-pressure cells. The high cost is its main disadvantage.

Erbium-doped glass lasers in the form of rods or optical fibres directly emit pulses at a wavelength of 1.5 µm. It was decided in this design to opt for a source of this type with its major advantages in terms of simplicity and cost in comparison with the OPOs. Their pulse energies vary from a few microjoules up to 40 mJ (Setzler et al., 2005). These values are lower than those obtained with SRS or OPOs but they are sufficient for our application. Other examples of lidar systems based on erbium-doped glass lasers can be found in Gaumet et al.(1998) and Lavrov et al. (2010).

Laser emitter

A Multiwave MOPA-L erbium-doped pulsed fibre laser model with a pulse energy of 25 μJ at 1550 nm (Multiwave, 2010) will be used as the emission source. The main advantage of this model over other pulsed fibre lasers is that it allows the combination of short pulse durations (<3.5 ns) with relatively low repetition frequencies (limited for eye safety reasons). This is possible because there is no amplified spontaneous emission (ASE) between the pulses. The chosen unit allows adjustment of the PRF from 1 Hz to 1 kHz, the maximum value established in Section 5.3.6.

The pulse energy is lower than the 50 μJ specified in Section 5.3, though this is compensated for because the chosen photodetector (Section 5.4.2) has lower noise values (NEP_m) and bandwidth than those considered in the SNR simulations described above.

The laser beam quality factor (M^2) (Saleh and Teich, 2007) is less than 1.1, with high spectral purity (0.25 nm) and with a divergence of less than 0.5 mrad (semiangle). The fibre pigtail ends with a collimator of 1.5 mm diameter and to ensure eye safety levels ($MPE = 0.1$ Jm^{-2} at $PRF = 1$ kHz, Section 5.2.4) the beam needs to be expanded to a diameter greater than 17.84 mm. A Thorlabs BE20M-C commercial beam expander model is used for this purpose with a power of 20X, allowing input beams of up to 2.25 mm diameter (Thorlabs, 2012a). At the expander output, the laser beam will have a diameter of 30 mm and a divergence of less than 25 μrad (Table 5.10.).

5.4.2 Receiver subsystem

Photodetector module

For the optoelectronic receiver the decision was taken to opt for the Thorlabs APD110C model which includes an InGaAsP APD photodiode with responsivity of 9 A/W ($M = 10$) and a transimpedance amplifier with a gain of 10^5 V/A (Thorlabs, 2009). The module has a bandwidth of 50 MHz, lower than the 107 MHz specified in Section 5.3. This model was chosen as the author was unable to find on the market any commercial InGaAsP APD module with a higher bandwidth. Applying Eq. 2.11, a distance resolution of 2 m is obtained.

The photosensitive surface of the APD has a diameter of just 200 μm and, therefore, its correct positioning requires the use of a precision 3-axis translation stage. The chosen model was a Thorlabs RB13M/M with a travel of 13 mm and an adjustment of 0.5 mm/rev (Thorlabs, 2012b). Similar solutions have been applied by Mayor and Supler (2004). The main characteristics of the photodetector module are shown in Table 5.10.

Receiver optics

An outline of the receiver optics of the microlidar is shown in Fig. 5.11. The backscattered energy is captured by a Meade ETX 80 reflector telescope (L_1) with an aperture of 80 mm and focal length f_1 equal to 400 mm (Meade, 2005). The light from the telescope must be collimated

to avoid detuning of the interference filter. The wavelength shift with angle is calculated as (Kovalev and Eichinger, 2004)

$$\frac{\lambda_{\varphi}}{\lambda_{normal}} = \left[\frac{m^2 - \sin^2 \varphi}{m^2} \right]^{1/2}, \tag{5.9}$$

where λ_{normal} [nm] is the centreline wavelength at normal incidence, λ_{φ} [nm] is the wavelength at an angle φ from the normal, and m is the index of refraction of the filter material.

Collimation is performed with a converging lens (L_2) confocally positioned (F_1'=F_2 in Fig. 5.11) with respect to the telescope. This gives rise to an inverted optical design, characterised by its having larger dimensions compared to the Galilean design (diverging lens) used in the lidar ceilometer (Fig. 3.7). In this case, using a diverging lens is not appropriate as it would need to be positioned in an initially inaccessible place of the telescope (between L_1 and F_1'), which would thus need significant modifications. The collimated light passes through an interference filter (10 nm bandwidth) whose function is selection of the wavelength of interest (1550 nm) and, following this, it is focussed by an aspheric lens (L_3) onto the photosensitive surface of the APD. Since aspheric lenses have larger numerical apertures (NA) and fewer aberrations than conventional spherical surfaces, they are commonly used in focussing and collimation applications.

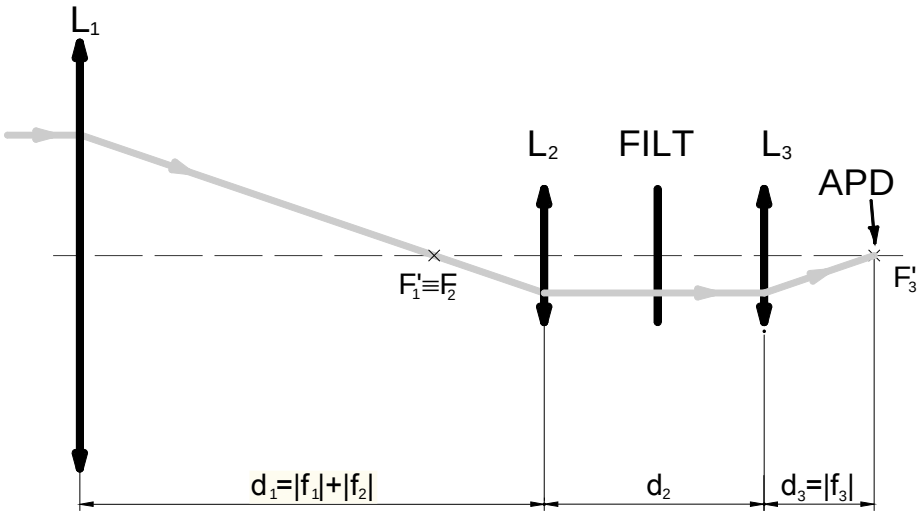

Fig. 5.11. Microlidar optical receiving scheme. (L_1) Telescope, (L_2) collimating lens, (FILT) interference filter, (L_3) focusing lens, (APD) photodetector active area.

As deduced from Eqs. (3.24) and (3.25) the focal lengths of the lenses L_2 and L_3 condition the value of the equivalent focal length of the system and, therefore, of its field of view ϕ. As explained in Section 3.3.2, the field of view is a key parameter on which the overlap factor depends. In Section 5.4.3 it is calculated that the minimum detection distance of the microlidar is 35 m and the need to achieve full overlap at a shorter distance in order to take maximum advantage of the detection range of the instrument is therefore clear.

Through simulation of the overlap factor (Eq. 3.16), it is concluded that the receiver system must have an equivalent focal length f_{eq} lower than or equal to 63 mm to ensure overlapping before 35 m. In this simulation, the values of divergence θ, of the diameter of the receiving optics d_0 and of the laser beam that are shown in Table 5.10. are considered. It is also assumed that the optical axes of reception and emission are parallel ($\delta = 0$ mrad) and that the separation d_i between the two is 80 mm. In any optical system, the effective diameter cannot exceed twice the focal distance (*f*-number technological limitation, see Smith, 2008), and therefore in this design the value of f_{eq} cannot be less than 40 mm. Knowing the interval of values that the equivalent focal length can take (63 mm $\leq f_{eq} \leq$ 40 mm), as well as the focal length of the telescope ($f_1 = 400$ mm) and applying Eq. (3.24), it is deduced that the focal lengths of lenses L_2 and L_3 must fulfil the following relationship,

$$6.35 \leq \frac{f_2}{f_3} \leq 10 . \tag{5.10}$$

An aspherical lens of 25 mm diameter and 15 mm focal length ($NA = 0.93$) was chosen for the focussing lens (L_3), with collimation (L_2) performed with a flat-convex lens of 25 mm diameter and focal length equal to 100 mm. So, the equivalent focal length is 60 mm (Eq. 3.24) and the field of vision (semiangle) is equal to 1.67 mrad (Eq. 3.25), a value much higher than the divergence of the laser beam. A wide field of vision such as this facilitates alignment of the emission and reception axes. Additionally, at 1550 nm background radiation is low (Table 5.5) and there is therefore no significant increase in the system noise. With the selected components, full overlap is reached at a distance of 33 m.

Data acquisition

The analogue signal from the photodetector module is digitalized using a Gage CompuScope 12502 analogue-digital converter (ADC) and transmitted to the processing unit (PC). The selected digitizer has 2 channels with a sampling rate of 500 MS/s and 12 bits of vertical resolution (Gage, 2011). This sampling rate is in accordance with the Nyquist criterion given a noise-equivalent reception bandwidth $B_N = 50$ MHz. The CompuScope also includes an on-board signal averaging method that allows the extraction of small signals from a noisy background (averages up to 1024 waveforms per session) with no CPU loading.

5.4.3 Microlidar detection range

The theoretical interval of distances in which the microlidar is able to measure drift clouds is calculated in this section. Knowing this range will allow verification of the correct operation of the instrument during the experimental stage.

Maximum detection distance

The maximum detection distance is determined by the most restrictive of the following conditions:

1) At this distance, the signal-noise ratio must take a value equal to or greater than 5, this being the minimum threshold established in Section 5.3.2. Applying Eq. (5.7), it is found that, for the design set out in Sections 5.4.1 and 5.4.2, $SNR = 5$ is achieved when the clouds are at a maximum distance of 500 m.

In this simulation, a system constant K_s of 18.85 Wm^3 and a background-radiance system constant K_b equal to $4.39 \cdot 10^{-7}$ $m^2 \cdot nm \cdot sr$ are considered, values calculated from the data shown in Table 5.10. The following values are considered for the photodetector module: $NEP_m = 0.47$ pW/$\sqrt{\text{Hz}}$, $R_{io} = 0.9$ A/W, $F = 5.5$ and $B_N = 50$ MHz (Thorlabs, 2009). The same atmospheric model as in Table 5.5 for $\lambda = 1550$ nm is considered. An optical transmission factor ξ_0 equal to 0.5 is estimated.

2) The single-pulse backscattered power (i.e. without pulse integration) from a cloud at the maximum detection range $R_{\max}$ must be capable of exciting at least one bit of the ADC card. This power is known as the minimum detectable power $P_{\min}$ and is given by the following expression (Rocadenbosch, 1996),

$$P_{\min} = \left(\frac{2V_{sat}}{2^{bits} - 1} \right) \frac{1}{\xi_0 R_i G_T} = 614 \quad pW \,, \tag{5.11}$$

where $V_{sat} = 100$ mV is the minimum voltage range of the digitizer and $bits = 9.5$ is the effective number of bits (ENOB) of the digitizer (Gage, 2011). The rest of the variables and their values have been previously presented.

The minimum detectable power $P_{\min}$ is related to the maximum detection range $R_{\max}$ through the elastic lidar equation (Eq. 3.7 and 3.8),

$$P_{\min} = P(R_{\max}) = K_s U_s \left(R_{\max} \right) \tag{5.12}$$

Resolving Eq. (5.12), a maximum range $R_{\max}$ of 3100 m is obtained.

So, criterion (1), corresponding to the signal-noise ratio, is the most restrictive, and it is concluded that the microlidar has a maximum range of 500 m. This value meets the initial design specification set out in Section 5.1.

Minimum detection distance

When the target is near the lidar system, the backscattered power is usually high and can even saturate the receiver. This saturation power or maximum detectable power $P_{\max}$ is given by the following expression (Rocadenbosch, 1996),

$$P_{\max} = \frac{V_{\max}}{\xi_0 R_i G_T} = 8 \quad \mu\text{W} \tag{5.13}$$

where $V_{max} = 3.6\,V$ is the maximum output voltage of the photodetector module (Thorlabs, 2009). In the present configuration, the photodetector module is the element which saturates first as the ADC card allows output voltages of up to ±5 V.

As in the case above, the maximum power P_{max} is related to the minimum detection distance R_{min} by the expression,

$$P_{max} = P(R_{min}) = K_s U_s(R_{min}) \tag{5.14}$$

Resolving Eq. (5.14), a minimum detection distance of 35 m is calculated. This value is considered appropriate since, in the actual drift tests, the passive collectors are usually positioned at a similar distance with respect to the spray zone.

PERFORMANCE		Measurement range Range Resolution, ΔR Eye safety	35 - 500 m 2 m Class 1M IEC/EN60825-1
EMITTER	Laser	Model Centre wavelength, λ Spectral width Pulse energy, E_0 Pulse duration, τ_l Pulse repetition frequency, *PRF*	Multiwave MOPA-L Series 1550 nm (Er-doped fibre laser) 0.25 nm 25 μJ < 3.5 ns 1 Hz – 1 kHz (adjustable)
	Beam Expander	Model Input beam diameter Output beam diameter Beam expansion Output beam divergence, θ	Thorlabs BE20M-C 1.5 mm 30 mm 20X < 25 μrad (semiangle)
RECEIVER	Telescope	Model Primary lens diameter, d_0 Equivalent focal length, f_{eq} Field of view, ϕ	Meade ETX80 80 mm 400 mm 1.67 mrad (semiangle)
	Interference filter	Centre wavelength, λ Full width at half maximum, $\Delta\lambda$	1550 nm 10 nm
	APD Module	Model Active area diameter, d_D Spectral response range Responsivity, R_i Noise Equivalent Power, NEP_m CW Saturation Power Photodiode damage threshold APD gain, M Transimpedance gain, G_T Output bandwidth (3 dB), B_N	Thorlabs APD110C 0.2 mm 900 to 1700 nm 9 A/W (1500 nm) 460 fW/$\sqrt{\text{Hz}}$ 4.2 μW 1 mW 10 10^5 V/A DC-50 MHz
	Digitizer	Model Sampling rate Resolution	GaGe CompuScope 12502 500 MS/s 12 bits

Table 5.10. System Specifications.

5.5 Experimental work

The manufacture of the prototype has been divided into two stages. In the first of these, a pulsed laser diode module at 1550 nm is used as the emission source and a PIN photodetector module as receiver. Using these low cost components will facilitate familiarisation with this wavelength and adjustment of the optomechanical components. These components will be replaced in the second phase with the laser emitter and APD module specified in Section 5.4.

The first manufacturing stage is underway at the present moment. For this, a Laser Components LS5-80-8-S10-00 pulsed laser module has been acquired comprised of 4 InGaAsP diodes which emit a total energy of 0.64 μJ per pulse at a maximum frequency of 7 kHz (Laser Components, 2009). The emitted beam has a high divergence (12º x 30º) and, moreover, it is not eye-safe. In order to obtain the required eye safety level ($MPE = 14.3\ \mathrm{mJ/m^2}$ at 7 kHz, Section 5.2.3) and reduce the divergence, a customised beam expander has been designed and implemented (Fig. 5.12). This expander consists of an optical tube of adjustable focal length and a 50 mm diameter aspherical lens of focal length equal to 100 mm. The expander output beam has a theoretical divergence of 1.75 mrad (semiangle). Adjustment of the emitter system (laser + expander) was carried out in the laboratory with the aid of an IR sensitive CCD camera (Fig. 5.12).

A Menlo Systems FPD510-F InGaAs PIN photodetector model was chosen for the receiver with a responsivity of 0.95 A/W, gain of 4×10^4 V/A and bandwidth equal to 200 MHz (Menlo Systems, 2012). The telescope and ADC card specified in Section 5.4 were also acquired. The optics system comprising L_2-FILT-L_3 as shown in Fig. 5.11 is presently under development. The photosensitive surface has a diameter of 300 μm, so the field of view will be 2.5 mrad (semiangle), a value higher than the divergence of the laser beam. With simulation it has been determined that full overlap will be reached at a distance of 30.4 m, assuming a slope of 0.75 mrad (converging) between the emitter and receiver axes.

This initial prototype has a very low system constant ($K_s = 0.482\ \mathrm{Wm^3}$) and, additionally, the PIN photodetector has lower sensitivity and higher noise level ($NEP_m = 3.2\ \mathrm{pW}/\sqrt{\mathrm{Hz}}$) than the APD module chosen in Section 5.4. As a result, pulse averaging needs to be performed so that the system is capable of detecting drift plumes located at several tens of metres (Eq. 3.14 and 3.15). The system will have a distance resolution of 1.6 m (Eq. 2.11), a value which is limited by the length of the laser pulses (8 ns).

5.6 Conclusions and future work

The key parameters (wavelength, pulse energy, emission frequency, reception area, etc.) have been determined in this chapter for the design of a microlidar for the detection of pesticide clouds. The methodology used is based on the use of SNR simulations and on the study of the MPE for different wavelengths. Conservative hypotheses have been assumed throughout the

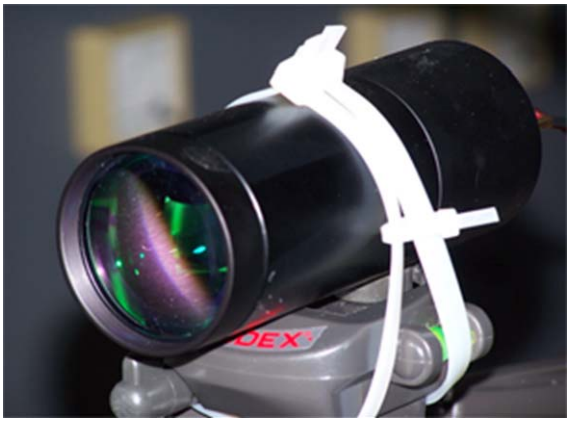

Front view of the emitter system, comprising a pulsed laser diode module and a beam expander.

Detail of the infrared camera used to record the image of the laser beam section when striking the translucent paper screen.

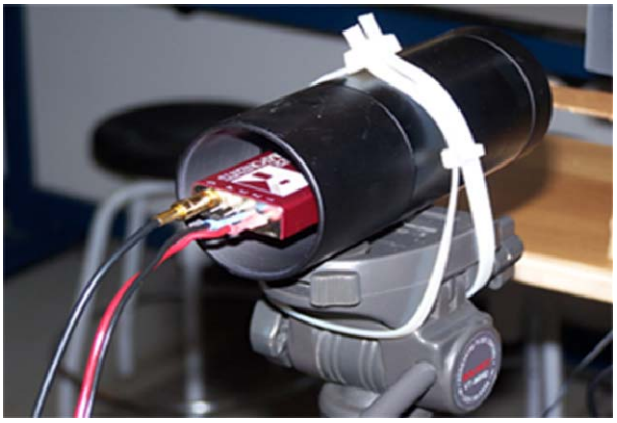

Rear view of the emitter system, showing the attachment of the laser to the expansion optics.

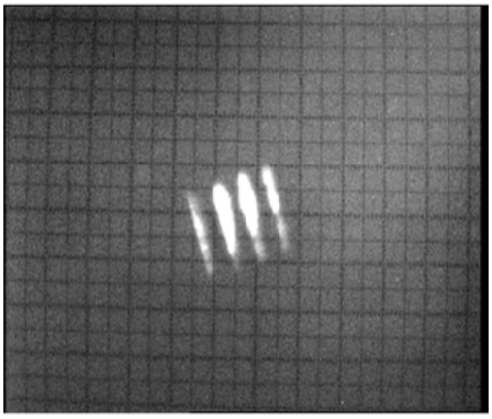

Image of the laser beam section striking a translucent paper screen. The sections of the four laser beams emitted by the four respective laser diodes which constitute the emission source can be clearly seen.

General view of the test set-up for emission characterisation: the laser emitter can be seen in the foreground and in the background is the screen which intercepts the infrared beam. Behind the screen is the infrared camera which records the beam spot image.

Fig. 5.12. Design and construction of the first version of the microlidar prototype for drift measurement in phytosanitary treatments. Images are from the characterisation tests of the optics system for the expansion and collimation of the infrared laser beam.

design process. Despite this, the results obtained are subject to some uncertainty due, principally, to ignorance of the typical optical parameters in drift clouds.

An initial laser diode based microlidar prototype will shortly be available. The measurements that will be obtained with this instrument are expected to help resolve the uncertainties mentioned above. The design outlined in Section 5.4 has been undertaken in such a way that, if necessary, it will be a relatively simple task to increase the value of the system constant K_s. The most economical option would be to replace the receiver telescope with 80 mm aperture with one of a larger diameter. This would entail a redesign of the collimation and focussing optics. A more expensive option would be to use a laser of higher power.

A scanning system will need to be implemented in more advanced versions so that the system is able to provide a bi-dimensional image of the pesticide plumes. In Spuler and Mayor (2005) an example of an eye-safe lidar system with scanning capabilities was presented. Other aspects that will need to be examined include the possibility of using a coaxial configuration for the purpose of reducing the minimum detection distance and the possible development of a customised receiver module with greater bandwidth and, therefore, better distance resolution.

6

Conclusions and future research lines

This chapter will report the main conclusions of the doctoral thesis and discuss potential future research lines.

6.1 Conclusions

Presented below are the main contributions of this doctoral thesis, grouped according to the objectives listed at the start of this work (Section 1.3).

Objective 1. *The design of a lidar system specifically for the remote sensing of pesticide drift.*

The first question that arises when the decision is taken to develop a new lidar instrument is what design methodology to apply. Although laser remote sensing is a well-established technique, modern monographs on lidar systems (Kovalev and Eichinger, 2004; Fuji and Fukuchi, 2005; Weitkamp, 2005) do not tackle the subject of design procedures and there is little to be found in the corresponding scientific literature (Agishev et al.., 2005). For these reasons, a new methodology has been developed in chapter 3 for use in lidar system designs for phytosanitary or ceilometry applications. This methodology is based on performing a parametric approximation of the signal-to-noise ratio, SNR (Eq. 3.14), from the system constant, K_s', the background-radiance system constant, K_b', and various characteristics of the receiver module (NEP_m, R_{io} and F). At the same time, the overlap factor, OVF (Eq. 3.16), is simulated by tuning the values of the field of view, ϕ, the laser beam divergence, θ, and the tilt angle, δ. The methodology has been validated through the construction of a 905-nm 5-kHz repetition rate diode-laser biaxial lidar ceilometer prototype and the execution of experimental measurements (topographic target and cloud detection).

The parametric methodology presented in chapter 3 was used in chapter 5 for the design of lidar instrument specifically for drift measurement. The question of eye safety was a basic requirement for this development (IEC 60825-1). SNR simulations were performed at different wavelengths (λ=905, 1064 and 1550 nm) to determine the energy intervals and reception area intervals required in each case. Based on these results and on the technological options available on the market, the final specifications of the lidar system were established. This will be comprised of a microlidar system with 25-µJ of pulse energy, emitting at 1550 nm via an Er-doped fibre laser (Table 5.10). Development of this instrument will entail a significant advance in the study of drift, providing information with temporal and distance resolution, something beyond the capabilities of the *in situ* collectors used at the present time (Section 2.1.1). Furthermore, the specifications of this system have been adapted specifically for the requirements of drift measurement, unlike the atmospheric lidars used in previous studies (Section 2.3.1). It will be an affordable and compact system, eye-safe, capable of near-field measurements (measurement range between 35 and 500 m) and with a high range resolution (2 m).

Objective 2. *Assessment of the capacity of lidar technology to quantify droplet concentration in drift clouds.*

The retrieval of physical properties (size distribution, volume and mass concentration) of aerosols (droplets) solely from lidar measurements is an ill-posed inverse problem (Ansmann and Müller, 2005). This kind of problem may have several solutions or the solution may have a non-continuous dependence on the input data. Due to the complexity of this problem, determination of the concentration in drift plumes by using lidar systems has only been dealt with – to the author's knowledge – in two previous studies (Hiscox et al., 2006; Khot et al., 2011), which were reviewed in Section 2.3.1.

In this thesis (Chapter 4), calibration of the lidar system was tackled as much from a theoretical perspective as an experimental one, with a study of the relationship between the backscattered time-integrated elastic lidar signal and the measurements obtained via the passive collectors commonly used for drift monitoring. A quantitative analytical model was formulated (Eq. 4.25), with which it was possible to ascertain the relationship between the measurements obtained from the two sensor types and which involved various parameters related to application and meteorological conditions: the mean cross-plume velocity, $\overline{w_p}$, collector efficiency, η_c, mean final tracer concentration, $\overline{\rho_{m,f}}$, and the effective radius of the droplets, $\overline{r_{eff}}$. The results of the experimental campaign revealed for each of the tests a strong linear relationship ($R^2 \approx 0.90$) between the measurements obtained from the two sensor types. This has led to the conclusion that the aforementioned application and meteorological parameters are spatially invariant for a given test.

The correlations obtained in this thesis are significantly higher than those calculated ($R^2 \approx 0.77$) by Khot et al. (2011), who also compared drift measurements with those taken by *in situ* collectors. This discrepancy may be because in their correlation study the authors considered simultaneously the measurements obtained in all the tests. In other words, they did not calculate the correlation for each of the tests separately. In a similar manner, the correlation between the lidar signal and the collectors for the tests presented in this thesis falls substantially ($R^2 \approx 0.67$) if all the measurements are considered simultaneously. These results allow the conclusion that for different tests the application and meteorological parameters are not spatially invariant and, therefore, the relationship between the lidar signal and the measurements of the passive collectors cannot be considered linear.

It can be deduced from the above that calibration of the lidar signal using cooperative sensors is valid for a given test, but that this calibration cannot be extrapolated to different tests.

6.2 Future research lines

An experimental prototype will be manufactured of the drift measurement lidar instrument. As was explained in detail in Section 5.5, the development of this system has been planned in two stages. In the first of these, a 1550 nm pulsed laser diode module will be used as emitter and a PIN photodetector module as receiver. This low cost version will enable familiarisation with this wavelength and facilitate a preliminary validation of the design. The final version will then be implemented based on an Er-doped fibre laser and an APD receiver module.

The availability of this instrument will open the door to the execution of a wide range of tests. Perhaps the most immediate of these will comprise an intercomparison campaign with cooperative sensors capable of measuring the concentration and distribution of drift droplet sizes, similar to those used with the Aglite system (see Section 2.3.2). This will simplify calibration of the lidar signal. It is expected that the developed instrument will enable estimation of the spray drift flux [g/s], a parameter which can be calculated if the drift concentration (calibrated lidar signal) and the cross-plume velocity, $\overline{w_p}$, are known. Flux measurement with the lidar may entail a substantial improvement over the present mass balance approach (Balsari et al., 2005; Salyani et al., 2007), the purpose of which is to quantify the fraction of the applied pesticide product which escapes from the treated area.

Consideration should also be given to the possible use of the developed instrument in other agroforestry applications such as measurement of the PM generated in agricultural and livestock farming, the monitoring of sprinkler irrigation and fertilizer spraying or the prevention of forest fires. This latter application, of particular importance in the Mediterranean basin, has been the subject of previous studies (Vilar and Lavrov, 2000; Utkin et al., 2002). These authors proposed the development of a lidar system at the same wavelength (1.5 μm) as that used in the lidar system design of this thesis.

There is great potential in the use of lidar systems to monitor drift and agricultural air quality in general. The availability of these instruments will enable better understanding of the phenomenon of drift and, as a result, the adoption of more efficient techniques to reduce or prevent its occurrence. It is the hope of the author of this thesis that the work presented here will contribute to the development of an agriculture which is more sustainable and respectful of mankind and the environment, while at the same time fulfilling its basic function of providing sufficient quality produce to feed us all.

Appendix. Spatial filter design

The ceilometer's receiving subsystem presented in Chapter 3 is characterized by a relatively wide field of view (4.92 mrad, Table 3.4) which has advantages in terms of measurement capacity but implies the reception of a higher background power. This appendix studies the possible use of a diaphragm working as a spatial filter. The combination of such diaphragm with a wide field of view allows to reach an appropriate backscattered power / background radiation ratio without renounce to the near / far field measurement capacity.

In relation to Fig. A.1 the image of atmospheric cross-section $\overline{O_1O_2}$ through the convergent lens $\overline{AB}$ (representing e.g. an equivalent system similar to L_1, L_2, L_3 in Fig. 3.7) is a position-offset confusion bright circle rather than a point in its image focal plane (Measures, 1992). Under background light conditions –as is always the case- if a photodetector is placed at the image focal plane the whole active area becomes background illuminated while only a small part of it corresponds to the backscatter signal return from $\overline{O_1O_2}$ (what is called confusion circle or signal spot). The idea of placing a diaphragm in the receiving optical system is to reduce the amount of background light arriving to the photodetector but without distorting the signal spot (backscattered lidar signal).

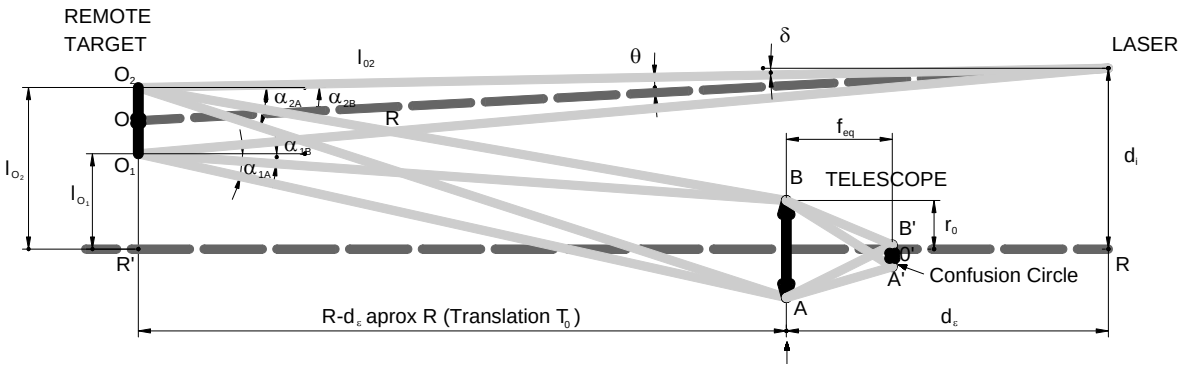

Fig. A.1. Geometrical representation of the laser / telescope biaxial arrangement when aiming at a remote target. The laser emits an optical beam with divergence θ and tilt angle δ (in relation to the telescope receiving axis $\overline{RR'}$) and illuminates remote target cross-section $\overline{O_1O_2}$ (e.g. a cloud) at a distance R. At reception, primary telescope lens $\overline{AB}$ images this target (Gregorio et al., 2006).

With a view to choosing a simple diaphragm shape and determine the best working plane along the receiving optical system of Fig. 3.7, two tentative planes, $\overline{QQ'}$ and $\overline{PP'}$ have been considered, and the simplifying assumption of uniform distribution of backscattered light radiation. Thus is not strictly true but enables a straightforward formulation of the problem. $\overline{QQ'}$ is an evaluation plane between primary lens L_1 and divergent lens L_2, at a distance d_Q from L_1 (Fig. 3.7) while $\overline{PP'}$ is the focal image plane of L_3.

Next, in order to compute both the signal spot size and its position offset (vertical displacement) in evaluation planes $\overline{QQ'}$ and $\overline{PP'}$ (Fig. 3.7), and starting from the emission / receiving biaxial arrangement ray-tracing model of Fig. A.1, the equivalent convergent lens $\overline{AB}$ (Eq. 3.24) is formally replaced with the receiving optics system of Fig. 3.7.

By using the well-known matrix ray-propagation analysis methodology (Möller,1988), signal spot radius ($\overline{A'B'}/2$ in Fig. A.1) and centre position (O' in Fig. A.1) in evaluation plane $\overline{QQ'}$ are computed from L_1 thin-lens matrix and translation (displacement) matrix in response to the four principal rays arriving to $\overline{AB}$ aperture (Fig. A.1). Following similar input variable and sign conventions these four principal rays are defined by their input height, y_i and arrival angles α_i as follows

$$\begin{aligned} y_i &= \pm r_0 \\ \alpha_i &= -\frac{d_i \pm r_0}{R} + (\delta \pm \theta) \end{aligned} \tag{A.1}$$

where subindex "i" stands for rays 1A, 1B, 2A and 2B and r_0 is the Fresnel lens radius, d_i is the distance between emission / reception optical axes, R is range (formally, the distance between the target and the primary (Fresnel) lens), δ is the tilt angle between emission / reception axes, and θ is the laser beam divergence (half-angle).

As a result of this geometrical-optics analysis, the signal spot radius in evaluation plane $\overline{QQ'}$ (i.e., at a distance d_Q from the Fresnel lens L_1) is

$$r_s = \left(1 - \frac{d_Q}{f_1}\right) r_0 + d_Q \frac{r_0}{R} + d\theta \tag{A.2}$$

where r_s is the signal spot radius, d_Q is the distance between the evaluation plane $\overline{QQ'}$ and the Fresnel lens L_1, f_1 is the Fresnel lens focal distance (Table 3.4) and the rest of variables have already been defined in Eq. (A.1).

The signal spot position offset in evaluation plane $\overline{QQ'}$ can be expressed as

$$r_f = -d_Q \frac{l_0}{R} \tag{A.3}$$

where

$$l_0 = d_0 - \delta R \tag{A.4}$$

where r_f is the vertical position offset in relation to the receiving optical axis ($\overline{RR'}$ in Fig. A.1) and the remaining variables have already been defined.

Likewise, signal spots characteristics can be evaluated at $\overline{PP'}$ focal plane under the confocal arrangement $d_1 = |f_1| - |f_2|$, $d_2 = |f_2| + |f_3|$, $d_3 = |f_3|$ (Fig. 3.7). The spot radius at $\overline{PP'}$ can be

obtained from Eq. (A.2) above in a very simple way by collapsing the whole receiving optics of Fig. 3.7 into a new equivalent lens L_1 with $f_1 = f_{eq}$ (Eq. 3.25) and setting $d_Q = f_{eq}$. Therefore, the spot radius at $\overline{PP'}$ (APD focal plane) becomes

$$r_s = f_{eq}\frac{r_0}{R} + f_{eq}\theta \tag{A.5}$$

where f_{eq} is the equivalent focal distance of the receiving optical system (304.8 mm) and the remaining variables have already been defined in Eq. (A.1), and the spot offset becomes

$$r_f = -f_{eq}\frac{l_0}{R} \tag{A.6}$$

From Eqs. (A.2)-(A.6) above and as a first approximation to quantify potential diaphragm efficiency in terms of a background-radiation rejection bound, this bound can be defined as the ratio between the background spot area and the signal spot area at the evaluation planes above. Because it has been assumed the initial approximation of uniform radiance distribution, the background spot area simply becomes the photodetector active area when considering $\overline{PP'}$ plane (i.e. the diaphragm is placed just over the photodetector surface) or L_2 divergent-lens area when considering $\overline{QQ'}$ plane moved to $d_Q = d_1 = |f_1| - |f_2|$ (i.e. diaphragm placed over L_2). In this latter case $d_Q = d_1$ for tentative mechanical support considerations.

With these considerations the background rejection ratio at the L_2 divergent lens plane $\overline{QQ'}$ is computed as

$$RD(R) = \frac{\pi \cdot r_2^2}{\pi \cdot \left[\left(1 - \frac{d_1}{f_1}\right) r_0 + d_1 \frac{r_0}{R} + d_1\theta\right]^2} = \left(\frac{r_2}{r_s'}\right)^2 \tag{A.7}$$

where r_s' is the signal spot radius (over evaluation plane $\overline{QQ'}$), r_2 is the L_2-divergent-lens radius (12.5 mm) and $d_1 = f_1 - f_2$ is the distance between the Fresnel lens, L_1, and the divergent lens, L_2 (see Fig. 3.7) (279.8 mm).

The rejection ratio at the photodetector focal plane $\overline{PP'}$ is

$$RF(R) = \frac{\pi \cdot r_D^2}{\pi \cdot \left[f_{eq}\frac{r_0}{R} + f_{eq}\theta\right]^2} = \left(\frac{r_D}{r_s}\right)^2 \tag{A.8}$$

where r_s is the signal spot radius (over evaluation plane $\overline{PP'}$) and r_D is the APD active area radius.

Table A.1 computes numerical results about the signal spot radius, r_s, position offset in relation to the receiving optical axis, r_f, and rejection ratios RD and RF (Eqs. A.7-A.8) for 3 range values ($R = 100$ m, $R = 1000$ m and $R \to \infty$).

	R = 100 m			R = 1000 m			$R \to \infty$		
	r_s [mm]	r_f [mm]	Reject.	r_s [mm]	r_f [mm]	Reject.	r_s [mm]	r_f [mm]	Reject.
Divergent Lens plane RD =	7.154	-0.139	3.049	6.962	0.238	3.226	6.941	0.279	3.247
Photodiode focal plane RF =	0.923	-0.152	2.646	0.714	0.259	4.425	0.691	0.305	4.717

Table A.1. Cross-comparison of main spot characteristics and background rejection ratios for two different positions of the diaphragm and three target ranges. r_s and r_f are respectively, the imaged spot radius and position offset (Eqs. A.2-A.6). RD and RF are the background rejection ratios (Eqs. A.7, A.8) and R is the target range. The diaphragm is tentatively located at L_2-divergent lens plane ($\overline{QQ'}$, Fig. 3.7) or at the photodetector focal plane ($\overline{PP'}$, Fig. 3.7).

It therefore emerges that for medium-to-far ranges ($R > 1000$ m), it is possible to achieve high rejection ratios by placing a diaphragm at the photodetector focal plane.

In this ceilometer prototype, and mainly due to its larger commercial availability, a rectangular slit diaphragm (1×3 mm) has been chosen. Other interesting slit diaphragm shapes (e.g. R^{-2} compensating diaphragms) are also found in the literature (Tikhomirov, 2001). Following similar analytical developments as the ones previously presented, it can be shown that by using this diaphragm a 1.9 rejection ratio can be achieved for height above 5 km.

From Table A.1 it is obvious that the signal spot offset moves along the vertical direction of the focal plane as a function of range R. From a practical point of view, this characteristic makes it necessary to align the diaphragm slit along the "vertical" direction of movement in the focal plane, otherwise the signal becomes clipped in the near range.

References

Abramochkin, A.I., Tikhomirov, A.A., 1999. Optimization of a lidar receiving system. 2. Spatial filters. Atmospheric and Oceanic Optics 12, 331-342.

AEPLA, 2012. Evolución del Mercado Fitosanitario 2000-2010. Available online http://www.aepla.es/evolucion-2000-2010 (accessed June 2012).

Agishev, R.R., Comeron, A., 2002. Spatial filtering efficiency of monostatic biaxial lidar: analysis and applications. Applied Optics 41(36), 7516-7521.

Agishev R., Gross B., Moshary F., Ahmed S., Gilerson A., 2005. Development of a SNR parameterization scheme for general lidar assessment. Applied Physics B 80 (6), 765-776.

All Weather Inc., 2005. Cloud Height Indicator Laser Ceilometer, Model 8339. User's Manual, Sacramento, California.

All Weather Inc., 2007. Cloud Height Indicator Laser Ceilometer, Model 8340. User's Manual, Sacramento, California.

Allard, M., Cayer, F., Champagne, Y., Babin, F., Cantin, D., 2007. Novel applications of an affordable short-range digital Lidar. Proceedings of the SPIE, 6681, 66810L1-11.

Analog Modules, Inc., 2002. Model 313A. High bandwidth bipolar transimpedance amplifier. Online http://www.analogmodules.com/admincenter/datasheets/313a.pdf (accessed April 2012).

Ansmann, A., Müller, D., 2005. Lidar and atmospheric aerosol particles. In: Weitkamp, C. (Ed.), Lidar. Range-Resolved Optical Remote Sensing of the Atmosphere. Springer, New York, pp. 105-141.

Balsari, P., Marucco, P., Tamagnone, M., 2005. A system to assess the mass balance of spray applied to tree crops. Transactions of the ASAE 48(5), 1689-1694.

Balsari, P., Marucco, P., Tamagnone, M., 2007. A test bench for the classification of boom sprayers according to drift risk. Crop Protection 26, 1482-1489.

Behrendt, A., Pal, S., Wulfmeyer, V., Valdebenito, A.M.B., Lammel, G., 2011. A novel approach for the characterisation of transport and optical properties of aerosol particles near sources. Part I: Measurement of particle backscatter coefficient maps with a scanning UV lidar. Atmospheric Environment 45, 2795–2802.

Berkoff, T.A., Welton, E.J., Campbell, J.R., Scott, V.S., Spinhirne, D.J., 2003. Investigation of overlap correction techniques for the Micro-Pulse Lidar NETwork (MPLNET). In: Proceedings of the Geoscience and Remote Sensing Symposium IGARSS'03, vol. 7, pp. 4395-4397.

Bilanin, A.J., Teske, M.E., Barry, J.W., Ekblad, R.E., 1989. AGDISP: The aircraft spray dispersion model, code development and experimental validation. Transactions of the ASAE 32(1): 327-334.

Bingham, G.E., Marchant, C.C., Zavyalov, V.V., Ahlstrom, D.J., Moore, K.D., Jones, D.S., Wilkerson, T.D, Hipps, L.E., Martin, R.S., Hatfield, J.L., Prueger, J.H., Pfeiffer, R.L., 2009.

Lidar based emissions measurement at the whole facility scale: Method and error analysis. Journal of Applied Remote Sensing 3(1), 033510. doi:10.1117/1.3097919.

Briand, O., Bertrand, F., Seux, R., Millet, M., 2002. Comparison of different sampling techniques for the evaluation of pesticide spray drift in apple orchards. Science of the Total Environment 288, 199–213.

Bui, Q., Womac, A., Howard, K.D., Mulrooney, J.E., Amin, M.K., 1998. Evaluation of samplers for spray drift. Transactions of the ASAE 41(1), 37-41.

Butler Ellis, M.C., Miller, P.C.H., 2010. The Silsoe spray drift model: A model of spray drift for the assessment of non target exposures to pesticides. Biosystems Engineering 107(3), 169-177.

Cambra-López, M., Aarnink, A.J.A., Zhao, Y., Calvet, S., Torres, A.G., 2010. Airborne particulate matter from livestock production systems: a review of an air pollution problem. Environmental Pollution 158, 1-17.

Carlile, W.R., 2006. Pesticide Selectivity, Health and the Environment. Cambridge University Press, Cambridge, United Kingdom.

Carnuth, W., Trickl, T., 1994. A powerful eyesafe infrared aerosol lidar: application of stimulated Raman backscattering of 1.06 micron radiation. Review of Scientific Instruments 65, 3324-3331.

CEC - Commission of the European Communities, 1991. Directive 91/414/EEC, concerning the placing of plant protection products on the market. Directorate-General for Agriculture, DG VI B II-1, Brussels, Belgium.

CEC - Commission of the European Communities, 2000. Directive 2000/60/EEC of 23 October 2000 establishing a framework for community action in the field of water policy.

CEC - Commission of the European Communities, 2002. Towards a thematic strategy on the sustainable use of pesticides. Communication from the commission to the Council, the European Parliament and the Economic and Social Committee, Brussels, Belgium.

CEC - Commission of the European Communities, 2006. Directive 2006/118/EC 12 December 2006 on the protection of groundwater against pollution and deterioration.

CEC - Commission of the European Communities, 2009. Directive 2009/128/EC of 21 October 2009 establishing a framework for Community action to achieve the sustainable use of pesticides.

Chueca, P., Garcerá, C., Moltó, E., Jacas, J.A., Urbaneja, A., Pina, T., 2010. Spray deposition and efficacy of four petroleum-derived oils used against Tetranychus urticae (Acari: Tetranychidae). Journal of Economic Entomology 103, 386-393.

Collis, R.T.H., 1968. Lidar observations of atmospheric motion in forest valleys. Bulletin of the American Meteorological Society 49, 918-922.

Collis, R.T.H., Russell, P.B., 1976. Lidar measurement of particles and gases by elastic backscattering and differential absorption. In: Hinkley, E.D. (Ed.), Laser Monitoring of the Atmosphere, E. D. Hinkley, Ed., Springer, Berlin/Heidelberg, pp. 71–151.

Cooke, B.K., Hislop, E.C., 1993. Spray tracing techniques. In: Matthews, G.A., Hislop, E.C., (Eds.), Application Technology for Crop Protection, CAB International, Wallingford, UK, pp. 85-100.

Cooper, J.F., Smith, D.N., Dobson, H.M., 1996. An evaluation of two field samplers for monitoring spray drift. Crop Protection 15, 249-257.

De Young, R.J., Barnes, N.P., 2010. Profiling atmospheric water vapour using a fiber laser lidar system. Applied Optics 49(4), 562-567.

Degreane Horizon, 2012. Laser Ceilometer, Model ALC30. Datasheet available online, http://www.degreane-horizon.com/GB/meteorology/autonomous-measurements/cloud-height-measurement.html (accessed February 2012).

Deirmendjian, D., 1969. Electromagnetic Scattering on Spherical Polydispersions. Elsevier, New York.

Dumbauld, R.K., J.R. Borklund, Saterlie, S.F., 1980. Computer model for predicting aircraft spray dispersion and deposition above and within forest canopies: User manual for the FSCBG computer program. Report No. 80-11. Davis, Calif.:USDA Forest Service.

EEC - European Economic Community, 2005. Regulation (EC) No 396/2005 of the European Parliament and of the Council of 23 February 2005 on maximum residue levels of pesticides in or on food and feed of plant and animal origin and amending Council Directive 91/414/EECText with EEA relevance.

EEC - European Economic Community, 2009. Regulation (EC) 1107/2009 of the European Parliament and of the council, of 21 October 2009 concerning the placing of plant protection products on the market and repealing Council Directives 79/117/EEC and 91/414/EEC.

Eichinger, W.E., Cooper, D.I., Hatfield, J.L., Hipps, L.E., Nicholls, J.J., Pfeiffer, R.L., Preuger, J.H., 2006. Use of elastic lidar to examine the dynamics of plume dispersion from an agricultural facility. In: Proceedings of the Workshop on Agricultural Air Quality: State of the Science, Ecological Society of America, pp. 215-226.

Eliason Engineering Inc., 2012. Cloud Ceilometer, Model CBME80. Datasheet online http://www.eliasson.com/products/cbme80.shtml (accessed February 2012).

EPA, 1999. Spray Drift of Pesticides. EPA Publication No.735F99024, Environmental Protection Agency, Washington, DC.

Erisman, J.W., Bleeker, A., Hensen, A., Vermeulen, A., 2008. Agricultural air quality in Europe and the future perspectives. Atmospheric Environment 42 (14), 3209–3217.

Excelitas Technologies Inc, 2011. Long Wavelength Enhanced Silicon APD, Models C30954EH, C30955EH and C30956EH. Datasheets available online, http://www.excelitas.com/downloads/DTS_LongWLEnSiliconAPDSeries.pdf, (accessed February 2012).

Felsot, A., Unsworth, J.B., Linders, J.B.H.J., Roberts, G., Rautman, D., Harris, C., Carazo, E., 2011. Agrochemical spray drift; assessment and mitigation – A review. Journal of Environmental Scienc and health, Part B., 46, 1-13.

Foreman, J.W., 1965. Measurement of localized flow velocities in gases with a laser Doppler flowmeter. Applied Physics Letters 7 (8), 77–78.

Freudenthaler, V., 2003. Optimized background suppression in near field lidar telescopes. In: Proceedings of the 6th International Symposium on Tropospheric Profiling: Needs and Technologies (ISTP 2003), pp. 243-245.

Fuji, T., Fukuchi, T., (Eds.), 2005. Laser Remote Sensing. Taylor & Francis Group, Boca Raton, FL.

Gage Applied Technologies, 2011. CompuScope 12501/12502. Available online at http://www.gage-applied.com/Products/PDF/GaGe-CS1250X-0311.pdf (accessed May 2012).

Ganzelmeier H., Rautmann D., Spangenberg R., Streloke M., Herrmann M., Wenzelburger H-J., Walter H-F., 1995. Studies on the spray drift of plant protection products. Mitteilungen aus der Biologischen Bundesanstalt für Land-und Forstwirschaft. Berlin-Dahlem. Heft, vol. 305.

Gaumet, J.L., Heinrich, J.C., Cluzeau, M., 1998. Cloud-base height measurements with a single-pulse erbium-glass laser ceilometer. Journal of Atmospheric and Ocenic Technology 15(1), 37-45.

Gil, Y., Sinfort, C., 2005. Emission of pesticides to the air during sprayer application: A bibliographic review. Atmospheric Environment 39, 5183-5193.

Gimmestad, G.G., Roberts, D.W., Stewart, J.M., West, L.L., Wood, J.W., 2003. NEXLASER – An Unattended Tropospheric Ozone and Aerosol Lidar – First Results. In: Proceedings of the Geoscience and Remote Sensing Symposium IGARSS'03, vol. 3, pp. 1754-1756.

Gimmestad, G.G., 2005. Differential-absorption lidar for ozone and industrial emissions, In: Weitkamp, C. (Ed.), Lidar. Range-Resolved Optical Remote Sensing of the Atmosphere. Springer, New York, pp. 187-212.

Gimmestad, G.G., Roberts, D.W, 2004. 1.5 Microns: the future of unattended aerosol lidar? In: Proceedings of the Geoscience and Remote Sensing Symposium IGARSS'04, vol. 3, pp. 1944-1946.

Glass, C.R, 2006. Field study methods for the determination of bystander exposure to pesticides. In: Martínez Vidal, J.L., Garrido Frenich, A. (Eds.), Pesticide Protocols (Methods in Biotechnology) 19. Humana Press Inc., Totowa, New Jeresey, pp. 165–177.

Gong, W., Chyba, T.H., Temple, D.A., 2007. Eye-safe compact scanning LIDAR technology. Optics and Lasers in Engineering 45, 898-906.

Gregorio, E., Rocadenbosch, F., Comerón, A., 2006. 905-nm biaxial lidar ceilometer prototype. Proceeding of the SPIE 6362, 63621L1-12.

Gregorio, E., Rocadenbosch, F., 2007. Perspective of remote optical measurement techniques (ROMTs). In: Proceedings of the Geoscience and Remote Sensing Symposium IGARSS'07, pp. 2955-2958.

Gregorio, E., Solanelles, F., Rocadenbosch, F., Rosell, J.R., Sanz, R., 2011. Airborne spray drift measurement using passive collectors and lidar systems. Proceedings of the SPIE 8174, 8174IL1-12.

Gregorio, E., Rocadenbosch, F., Tiana-Alsina, J., Comerón, A., Sanz, R., Rosell, J.R., 2012. Parameter design of a biaxial lidar ceilometer. Journal of Applied Remote Sensing 6(1), 063546. doi: 10.1117/1.JRS.6.063546.

Hamamatsu Photonics, 1998. Photon Counting. Using Photomultiplier Tubes. Japan.

Hamamatsu Photonics, 2004. Characteristics and Use of Si-APD. Japan.

Hamamatsu Photonics, 2005. Si-APD, S6045 series. Japan.

Hamamatsu Photonics, 2007. APD module, C5331 series. Japan.

Hamamatsu, 2012 APD Modules. http://sales.hamamatsu.com/en/products/solid-state-division/si-photodiode-series/apd-modules.php?src=hp (accessed February 2012).

Harrell, S.R., Wilcox, W., Killinger, D., Rines, G.A., Schwarz, R., 1995. High power, eye-safe 1.57 micron OPO lidar for atmospheric boundary layer measurements. Proceedings of the SPIE 2366, 354-357.

Hartung, J., Seedorf, J., Trickl, T., Gronauer, H., 1997. Emission and Distribution of Airborne Particulates from a Piggery. In: Proceedings of the 9th International Congress in Animal Hygiene, pp. 184-187.

He, J.F., Zhag, Y.J. Liu, W.Q., Ruan, J., Wang, L.M., 2010. Random-modulation CW laser ceilometer signal processing based on compound PN sequence. Proceedings of the SPIE 7656, 76562W.

Hecht, J., 2008. Understanding Lasers: An Entry-Level Guide. IEEE Press, New York.

Hecht, J., 2010. Laser remote sensing: New needs and technology push laser remote sensing in the atmosphere. Laser Focus World 46(6), 35-40.

Heese, B., Flentje, H., Althause, D., Ansmann, A., Frey, S., 2010. Ceilometer lidar comparison: backscatter coefficient retrieval and SNR determination. Atmospheric Measurement Techniques 3, 1763-1770.

Henderson, R., Schulmeister, K., 2004. Laser Safety. Taylor & Francis, New York.

Hiscox, A.L., Miller, D.R., Nappo, C.J., Ross, J., 2006. Dispersion of fine spray from aerial applications in stable atmospheric conditions. Transactions of the ASABE 49(5), 1513–1520.

Hiscox, A.L., Miller, D.R., Holmén, B.A., Yang, W., Wang, J., 2008. Near-field dust exposure from cotton field tilling and harvesting. Journal of Environmental Quality 37 (2), 551–556.

Hoff, R.M., Mickle, R.E., Froude, F.A., 1989. A rapid acquisition lidar for aerial spray diagnostics. Transactions of the ASAE 32(5), 1523-1528.

Hofman, V., Solseng, E., 2001. Reducing Spray Drift. Noth Dakota State Univesity. http://www.ag.ndsu.edu/pubs/ageng/machine/ae1210w.htm (accessed July 2012).

Holmén, B.A., Eichinger, W.E., Flocchini, R.G., 1998. Application of elastic lidar to PM_{10} emissions from agricultural nonpoint sources. Environmental Science & Technology 32, 3068-3076.

Holmén, B.A., James, T.A., Ashbaugh, L.L., Flocchini, R.G., 2001a. Lidar-assisted measurement of PM_{10} emissions from agricultural tilling in California's San Joaquin Valley. I: Lidar. Atmospheric Environment 35, 3251-3264.

Holmén, B.A., James, T.A., Ashbaugh, L.L., Flocchini, R.G., 2001b. Lidar-assisted measurement of PM_{10} emissions from agricultural tilling in California's San Joaquin Valley. I: Lidar. Atmospheric Environment 35, 3265-3277.

Holmén, B.A., Miller, D.R., Hiscox, A.L., Yang, W., Sammis, T.W., Bottoms, R., 2008. Near-source particulate emissions and plume dynamics from agricultural field operations. Journal of Atmospheric Chemistry 59(2), 117-134.

Huddleston, E.W., Ledson, T.M., Ross, J.B., Sanderson, R., Miller, D.R., Steinke, W.E., Aylor, D.E., Perry, S.G., 1996. Development of a pesticide drift model for orchard air-blast spraying. In: Proceedings of the Brighton Crop Protection Conference: Pests and Diseases, pp. 1187-1192.

Hulburt, E.O., 1937. Observations of a searchlight beam to an altitude of 28 kilometers. Journal of the Optical Society of America 27(11), 377-382.

ICNIRP, 1996. Guidelines on Limits of Exposure to Laser Radiation of Wavelengths between 180 nm and 1.000 μm.

IEC 60825-1, 2007. Safety of Laser Products – Part 1: Equipment Classification and Requirement. Geneva: International Electrotechnical Commission, Edition 20;2007-03.

ISO 22866, 2005. International Standard. Equipment for Crop Protection. Methods for Field Measurement of Spray Drift.

ISO 22856, 2008. Equipment for Crop Protection –Laboratory Measurement Methods of Spray Dift.

Jenoptik Optical Systems Inc., 2012. Ceilometer, Model CHM15K-x. Datasheet online, http://www.jenoptik.com/cms/products.nsf/0/9EA4CC3F1176069EC1257775007F0BE7/$File/chm_15k_15k-x_en_web.pdf?Open, (accessed February 2012).

Johnstone D.R., Rendell C.H., Sutherland, J.A., 1977. The short-term fate of droplets of coarse aerosol size in ultra-low-volume insecticide application on to a tropical field crop. Journal of Aerosol Science 8(6), 395-407.

Kärkkäinen, A.M., Piironen, A.K., Kähkönen, T., Lönnqvist, J., 1997. The characteristics and performance of Vaisala's new CT75K lidar ceilometer. Proceedings of the SPIE 3104, 12-17.

Khot, L.R., Miller, D.R., Hiscox, A.L., Salyani, M., Walker, T.W., Farooq, M., 2011. Extrapolation of droplet catch measurements in aerosol application treatments. Atomization and Sprays 21(2), 149-158.

Klett, J.D., 1985. Lidar inversion with variable backscatter/extinction ratios. Applied Optics 24, 1638-1643.

Koschmieder, H., 1924. Theorie der horisontalen Sichtweite. Beitr. Beiträge zur Physik der freien Atmosphäre 12, 33-53 (in German).

Kovalev, V.A., Eichinger, W.E., 2004. Elastic Lidar: Theory, Practice, and Analysis Methods, Wiley-Interscience, New York.

Laser Components, 2009. Pulsed Laser Diode Module LS-Series. Datasheet available at http://www.lasercomponents.com/fileadmin/user_upload/home/Datasheets/lce/ls-series.pdf (accessed May 2012).

Laven, P., 2011. MiePlot - A Computer Program for Scattering of Light from a Sphere using Mie Theory & the Debye Series. Available at http://www.philiplaven.com/mieplot.htm (accessed May 2012).

Lavrov, A., Utkin, A.B., Vilar, R., 2010. Simple eye-safe lidar for cloud height measurement and small forest fire detection. Optics and Spectroscopy 109 (1), 144-150

Leosphere, 2009. Cloud & aerosol lidar for atmospheric monitoring. ALS 300/450 Product information. Orsay, France.

Ludbrook, F.T., Winstanley, J.V., 1977. New laser ceilometer. IEE Journal on Electronic Circuits and Systems 1(2), 64-72.

Maiman, T.H., 1960. Stimulated optical radiation in ruby. Nature 187, 493–494.

Marchant, C.C., Wilkerson, T.D., Bingham, G.E., Zavyalov, V.V., Andersen, J.M., Wright, C.B., Cornelsen, S.S., Martin, R.S., Silva, P.J., Hatfield, J.L., 2009. Aglite lidar: A portable elastic lidar system for investigating aerosol and wind motions at or around agricultural production facilities. Journal of Applied Remote Sensing 3(1), 033511. doi: 10.1117/1.3097928.

Marchant, C.C., Moon, T.K., Gunther, J.H., 2010. An iterative least-squares approach to elastic lidar retrievals for well characterized aerosols. IEEE Transactions on Geoscience and Remote Sensing 48 (5), 2430–2444.

Marchant, C.C., Moore, K.D., Wojcik, M.D., Martin, R.S., Pfeiffer, R.L., Prueger, J.H., Hartfield, J.L., 2011. Estimation of dairy particulate matter emission rates by lidar and inverse modeling. Transactions of the ASABE 54(4), 1453-1463.

Marrs, R.H., Williams, C.T., Frost, A.J., Plant, R.A., 1989. Assessment of the effects of herbicides spray drift on a range of plant species of conservation interest. Environmental Pollution 59, 71-86.

May, K.R., Clifford, R., 1967. The impaction of aerosol particles cylinders, spheres, ribbons and discs. Annals of Occupational Hygiene 10, 83-95.

Mayor, S.D., Spuler, S.M., 2004. Raman-shifted eye-safe aerosol lidar. Applied Optics 43(19), 3915-3924.

Mayor, S.D., Spuler, S.M., Morley, B.M., Loew, E., 2007. Polarization lidar at 1.54 μm and observations of plumes from aerosol generators. Optical Engineering 46(9), 096201.

McClellan, J.H., Parks, T.W., 2005. A personal history of the Parks-McClellan algorithm. IEEE Signal Processing Magazine 22(2), 82-86.

McCormick, M.P., Melfi, S.H., Olsson, L.E., Tuft, W.L., Elliott, W.P., Egami, R., 1972. Mixing-height measurements by lidar, particle counter, and rawinsonde in the Willamette Valley, Oregon. NASA Tech. Note D-7 103: 77.

McDonald, J.E., 1962. Large-sphere limit of the radar back-scattering coefficient. Quarterly Journal of the Royal Meteorological Society 88, 183-186.

Meade Instruments Corporation, 2005. ETX-80 AT-TC Instruction Manual. Irvine, California.

Measures, R., 1992. Laser Remote Sensing: Fundamentals and Applications. Krieger Publishing Co, Malabar, FL.

Menlo Systems GmbH, 2012. High Sensitivity Fast PIN Photodetector Series FPD 510. Online http://www.menlosystems.com/media/pdf/DataSheet/FPD510_DataSheet.pdf (accessed May 2012).

Mickle, R.E., 1994. Utilizing vortex behaviour to minimize drift. Journal of Environmental Science and Health, Part B, 29, 621-645.

Mickle, R.E., 1996. Influence of aircraft vortices on spray cloud behaviour. Journal of the American Mosquito Control Association 12(2), 372-379.

Mickle, R.E., 1999. Analysis of Lidar Studies Conducted During Aerial Spray Drift Trials. REMPSpC Report, Ayr, Ontario, Canada.

Miller, D.R., Stoughton, T.E., 2000. Response of spray drift from aerial applications at forest edge to atmospheric stability. Agricultural and Forest Meteorology 100, 49-58.

Miller, D., Salyani, M., Hiscox, A., 2003. Remote measurement of spray drift from orchard sprayer using LIDAR. In: Proceedings of the 2003 ASAE Annual International Meeting, paper No. 031093.

Miller, D.R., Khot, L.R., Hiscox, A.L., Salyani, M., Walker, T.W., Farooq, M., 2012. Effect of atmospheric conditions on coverage of fogger applications in a desert surface boundary layer. Transactions of the ASABE 55(2), 351–361.

Miller P.C.H., 1993. Spray drift and its measurement. Matthews, G.A., Hislop, E.C., (Eds.), Application Technology for Crop Protection, CAB International, Wallingford, UK, pp. 101-121.

Miller, P.C.H., 2003. The measurement of spray drift. Pesticide Outlook 14, 205–209.

Möller, K.D., 1988. Optics. University Science Books, Mill Valley, California.

Morille, Y., Haeffelin, M., Drobinski, P., Pelon, J., 2007. STRAT: An automated algorithm to retrieve the vertical structure of the atmosphere from single-channel lidar data. Journal of Atmospheric and Oceanic Technology 24(5), 761-775.

Multiwave Photonics, S.A., 2010. MOPA-L Series Pulsed Fiber Lasers. Datasheet online at http://www.multiwavephotonics.com/img_upload/produtos/5129_3.pdf (accessed April 2012).

Münkel, C., Leiterer, U., Dier, H., 2002. Affordable lidar for atmospheric aerosol and cloud studies. Proceedings of the SPIE 4484, 198-206.

MTECH Systems Inc., 2012. Ceilometer Sensor, Model 8200-CHS. Datasheet available online http://www.mtechsystems.com/data-sheets/8200-CHS-Ceilometer-Sensor.pdf (accessed February 2012).

Navidi, W.C., 2006. Estadística para Ingenieros y Científicos. McGraw-Hill, México D.F. (in Spanish).

Nuyttens, D., Taylor, W.A., De Schampheleire, M., Verboven, P., Dekeyser, D., 2009. Influence of nozzle type and size on drift potential by means of different tunnel evaluation methods. Biosystems Engineering 103: 271-280.

Patterson, E.M., Roberts, D.W., Gimmestad, G.G., 1989. Initial measurements using a 1.54-µm eyesafe Raman shifted lidar. Applied Optics 28, 4978-4981.

Perkin Elmer, Inc., 2008. Long Wavelength Enhanced Silicon APDC30954EH, C30955EH and C30956EH Series. Datasheet available online http://www.perkinelmer.com/PDFS/downloads/dts_longwlensiliconapdseries.pdf (accessed April 2012).

Perkin Elmer, Inc., 2010. Avalanche Photodiode. A User Guide. Datasheet online, http://www.perkinelmer.com/CMSResources/Images/44-6538APP_AvalanchePhotodiodesUsersGuide.pdf (accessed April 2012).

Platt, U., Perner, D., Pätz, H.W., 1979. Simultaneous measurements of atmospheric CH_2, O_3 and NO_2 by differential optical absorption. Journal of Geophysical Research 84, 6329–6335.

Reba, M.N.M., Rocadenbosch, F., Sicard, M., Muñoz, C., Tomás, S., 2007. Piece-wise variance method for SNR estimation in elastic/Raman lidar signals. In: Proceedings of the Geoscience and Remote Sensing Symposium IGARSS'07, pp. 3158-3161.

Riley, C.M., Wiesner, C.J., 1998. On-target and off-target deposition. In: Ecobichon, D.J. (Ed.), Occupational Hazards of Pesticide Exposure: Sampling, Monitoring, Measuring. Taylor & Francis, Philadelphia, Pa, pp. 9-50.

Rocadenbosch, F., 1996. Lidar Sensing of the Atmosphere: Receiver Design and Inversion Algorithms for an Elastic System. PhD thesis, Universitat Politècnica de Catalunya, Dep. Signal Theory and Communications, Barcelona, Spain.

Rocadenbosch, F., Comerón, A., Pineda, D., 1998. Assessment of lidar inversion errors for homogeneous atmospheres. Applied Optics 37(12), 2199-2206.

Rocadenbosch, F., Soriano, C., Comerón, A., Baldasano, J.M., Rodríguez, A., Muñoz, C., García-Vizcaino, D., 2001. 3D scanning portable backscatter lidar platform for atmospheric remote sensing: performance and architecture overview. Proceedings of the SPIE 4168, 158–169.

Rocadenbosch, F., 2003a. Lidar-aerosol sensing. In: Driggers, R.G. (Ed.), Enciclopedia of Optical Engineering. Marcel Dekker Inc., New York, pp. 1090-1102.

Rocadenbosch, F., 2003b. Lidar-wind, Raman, and other sensing. In: Driggers, R.G. (Ed.), Enciclopedia of Optical Engineering. Marcel Dekker Inc., New York, pp. 1114-1127.

Rothman, L.S., Rinsland, C.P., Goldman, A., Massie, S.T., Edwards, D.P., Flaud, J.M., Perrin, A., Camypeyret, C., Dana, V., Mandin, J.Y., Schroeder, J., McCann, A., Gamache, R.R., Wattson, R.B., Yoshino, K., Chance, K.V., Jucks, K.W., Brown, L.R., Nemtchinov, V., Varanasi, P., 1998. The HITRAN molecular spectroscopic database and hawks (HITRAN atmospheric workstation): 1996 Edition. Journal of Quantitative Spectroscopy and Radiative Transfer 60, 665-710.

Saleh, B.E.A., Teich, M.C., 2007. Fundamentals of Photonics. Wiley, New York.

Salyani, M., Farooq, M., Sweeb, R.D., 2007. Spray deposition and mass balance in citrus orchard applications. Transactions of the ASABE 50(6), 1963-1969.

Schneider, J., Balis, D., Böckmann, C., Bösenberg, J., Calpini, B., Chaikovski, A., Comeron, A., Flamant, P., Freudenthaler, V., Hagard, A., Mattis, I., Mitev, V., Papayannis, A., Pappalardo, G., Pelon, J., Perrone, M.R., Resendes, D., Spinelli, N., Trickl, T., Vaughan, G., Visconti, G., 2000. A European aerosol research LIDAR Network to establish an aerosol climatology (EARLINET). Journal of Aerosol Science 31, S592-S593.

Schotland, R.M., 1964. The determination of the vertical profile of atmospheric gases by means of a ground based optical radar. In: Proceeding of the 3rd Symposium on Remote Sensing of the Environment, pp. 215–224.

Segelstein, D.J., 1981. The Complex Refractive Index of Water. MS thesis, Department of Physics, University of Missouri-Kansas City, Kansas City, Missouri, USA.

Setzler, S.D., Francis, M.P., Young, Y.E., Konves, J.R., Chicklis, E.P., 2005. Resonantly pumped eyesafe erbium lasers. IEEE Journal of Selected Topics in Quantum Electronics 11(3), 645-657.

Shapiro, S.S., Wilk, M.B., 1965. An analysis of variance test for normality (complete samples). Biometrika 52, 591-611.

Sicard, M., Pujadas, M., Alados-Arboledas, L., Pedrós, R., Díaz, J.P., Córdoba-Jabonero, C., Requena, A., Comerón, A., Rocadenbosch, F., Wagner, F., Rodrigues, J., Moreno, J.M.,

2011. SPALINET: The Spanish and Portuguese aerosol lidar network. Óptica Pura y Aplicada 44, 1–5.

Sigrist, M.W., 1993. Air Monitoring by Spectroscopic Techniques. Wiley-Interscience, New York.

Skolnik, M.I., 2001. Introduction to Radar Systems. McGraw-Hill, New York.

Smith, W.J., 2008. Modern Optical Engineering. Mc Graw-Hill, New York.

Smullin, L.D., Fiocco, G., 1962. Optical echoes from the moon. Nature 194, 1267.

Solanelles F., Fillat A., Escolà A., Planas S., 2001. Effect of air injector nozzles on the spray distribution of a pear orchard. Parasitica 57, 61-68.

Solanelles, F., 2009. Avaluació de Diferents Tècniques d'Aplicació per a la Reducció de la Contaminació en els Tractaments Fitosanitaris. PhD thesis (in catalan), Universitat de Lleida, Dep. Agroforestry Engineering, Lleida, Spain.

Spinhirne, J.D., 1993. Micro-pulse Lidar. IEEE Transactions on Geoscience and Remote Sensing 31, 48-55.

Spinhirne, J.D., Chudamani, S., Cavanaugh, J.F., Bufton, J.L., 1997. Aerosol and cloud backscatter at 1.06, 1.54, and 0.53 μm by airborne hard-target-calibrated Nd:YAG/methane Raman lidar. Applied Optics 36(15), 3475-3490.

Spuler, S.M., Mayor, S.D., 2005. Scanning eye-safe elastic backscatter lidar at 1.54 μm. Journal of Atmospheric and Oceanic Technology 22(5), 696-703.

Stoughton, T.E., Miller, D.R., Yang, Y., Ducharme, K.M., 1997. A comparison of spray drift predictions to lidar data. Agricultural and Forest Meteorology 88, 15-18.

Streicher, J., Werner, C., Dittel, W., 2004. Design of a small laser ceilometer and visibility measuring device for helicopter landing sites. Proceedings of the SPIE 5240, 31-41.

Takeuchi, N., Sugimoto, N., Baba, H., Sakurai, K., 1983. Random modulation CW lidar. Applied Optics 22 (9), 1382-1386.

Teske, M.E., Bird, S.L., Esterly, D.M., Curbishley, T.B., Ray, S.L., Perry, S.G., 2002. AgDRIFT: A model for estimating near-field spray drift from aerial applications. Environmental Toxicology and Chemistry 21(3), 659-671.

Teske, M.E., Thistle, H.W., Schou, W.C., Miller, P.C.H., Strager, J.M., Richardson, B., Butler Ellis, M.C., Barry, J.W., Twardus, D.B., Thompson, D.G., 2011. A review of computer models for pesticide deposition prediction. Transactions of the ASABE 54(3), 789-801.

Thorlabs, Inc., 2009. APD 110x Series. Avalanche Photodetectors. Operation Manual. Available online, http://www.thorlabs.com/Thorcat/19500/19566-D02.pdf (accessed April 2012).

Thorlabs, Inc., 2012a. Beam expanders with collimation adjustment. Available online, http://www.thorlabs.de/catalogpages/V21/949.PDF (accessed April 2012).

Thorlabs, Inc., 2012b. RB13 Series 3-Axis Translation Stage. User Guide. Online, http://www.thorlabs.com/Thorcat/12700/12782-D02.pdf (accessed May 2012).

Tikhomirov, A.A., 2001. Predetector Processing of Lidar Returns in Atmospheric Laser Sensing. Russian Physics Journal 44(10), 1115-1127.

Tomás, S., 2011. Contributions of elastic-backscatter lidars to wind field retrieval and Atmospheric Boundary Layer monitoring. PhD thesis, Universitat Politècnica de Catalunya, Dep. Signal Theory and Communications, Barcelona, Spain.

Tsai, M.Y., 2007. The Washington Spray Drift Studies: Understanding the Broader Mechanisms of Pesticide Spray Drift. PhD thesis, University of Washington, Seattle, USA.

Turner, D. B., 1994. Workbook of Atmospheric Dispersion Estimates: An Introduction to Dispersion Modeling. CRC Press, Boca Raton, Fl.

Unsworth, J.B., Wauchope, R.D., Klein, A.W., Dorne, E., Zeeh, B., Yeh, S.M., Akerblom, M., Racke, K.D., Rubin, B., 1999. Significance of the long range transport of pesticides in the atmosphere. Pure and Applied Chemistry 71(7), 1359-1383.

Utkin, A.,B., Lavror, A.V., Costa, L., Simoes, F., Vilar, R., 2002. Detection of small forest fires by lidar. Applied Physics B 74, 77–83

Vaisala Inc., 1999. Ceilometer, Model CT25k. User's Guide, Finland.

Vaisala Inc., 2004. Ceilometer, Model CL31. User's Guide, Finland.

Vaisala Inc., 2010. Cloud Height-range Cloud Height detection, Model CL51. Datasheet available online, http://www.vaisala.com/en/products/ceilometers/Pages/CL51.aspx, (accessed February 2012).

Valdebenito, A.M.B., Pal, S., Behrendt, A., Pal, S., Wulfmeyer, V., Lammel, G., 2011. A novel approach for the characterisation of transport and optical properties of aerosol particles near sources. Part II: Microphysics-chemistry-transport model development and application. Atmospheric Environment 45, 2981–2990.

Van den Berg, F., Kubiak, R., Benjey, W.G., Majewski, M.S., Yates, S.R., Reeves, G.L., Smelt, J.H., Van der Linden, A.M.A., 1999. Emission of pesticides into the air. Water, Air & Soil Pollution 115, 198–218.

Vilar, R., Lavrov, A., 2000. Estimation of required parameters for detection of small smoke plumes by lidar at 1.54 μm. Applied Physics B 71, 225–229

Wang, J., Hiscox, A.L., Miller, D.R., Sammis, T.W., 2008. A dynamic Lagrangian, field-scale model of dust dispersion from agriculture tilling operations. Transactions of the ASABE 51(5), 1763-1774.

Wang, J., Hiscox, A.L., Miller, D.R., Sammis, T.W., 2009. A comparison of Lagrangian model estimates to LIDAR measurements of dust plumes from field tilling. Journal of the Air & Waste Management Association 59, 1370–1378.

Wen, L., Jin, J., Wojcik, M.D., 2011. High-resolution simulations of particulate matter emitted by different agriculture tillage under different weather conditions in California, USA. Environmental Earth Sciences 64, 1021-1029.

Weitkamp C. (Ed.), 2005. Lidar: Range-Resolved Optical Remote Sensing of the Atmosphere. Springer, New York.

Wojcik, M.D., Martin, R.S., Hatfield, J.L., 2012. Using lidar to characterize particles from point and diffuse sources in an agricultural field. In: Chang, N.B. (Ed.), Environmental Remote Sensing and Systems Analysis. CRC Press, Boca Raton, FL, pp. 299–331.

Yates, S.R., McConnell, L.L., Haperman, C.J., Papiernik, S.K., Gao, S., Trabue, S.L., 2011. Managing agricultural emissions to the atmosphere: state of the science, fate and mitigation, and identifying research gaps. Journal of Environmental Quality 40, 1347-1358.

Yusà, V., Coscollà, C., Mellouki, W., Pastor, A., de la Guardia, M., 2009. Sampling and analysis of pesticides in ambient air. Journal of Chromatography A 1216, 2972–2983.

Zalay, A.D., Bouse, L.F., Carlton, J.B., Crookshank, H.R., Eberle, W.R., Howle, R.E., Shrider, K.R., 1980. Measurement of airborne spray with a laser Doppler velocimeter. Transactions of the ASAE, 23, 548–552.

Zavyalov, V.V., Marchant, C.C., Bingham, G.E., Wilkerson, T.D., Hatfield, J.L., Martin, R.S., Silva, P.J., Moore, K.D., Swasey, J., Ahlstrom, D.J., Jones, T.L., 2009. Aglite lidar: calibration and retrievals of well characterized aerosols from agricultural operations using a three-wavelength elastic lidar. Journal of Applied Remote Sensing 3(1), 033522. doi:10.1117/1.3122363.

List of publications

Journals

Rocadenbosch, F., Frasier, S., Kumar, D., Lange, D., Gregorio, E., Sicard, M., 2012. Backscatter error bounds for elastic lidar two-components inversion algorithm. IEEE Transactions on Geoscience and Remote Sensing 50(11), 4791-4803.

Gregorio, E., Rocadenbosch, F., Tiana-Alsina, J., Comerón, A., Sanz, R., Rosell, J.R., 2012. Parameter design of a biaxial lidar ceilometer. Journal of Applied Remote Sensing 6(1), 063546. doi: 10.1117/1.JRS.6.063546.

Sanz, R., Llorens, J., Escolà, A., Arnó, J., Ribes, M., Masip, J., Camp, F., Gràcia, F., Solanelles, F., Planas, S., Pallejà, T., Palacin, J., Gregorio, E., Del Moral, I., Rosell, J.R., 2011. Innovative lidar 3D dynamic measurement system to estimate fruit-tree leaf area. Sensors 11(6), 5769-5791.

Sanz, R., Llorens, J., Rosell, J.R., Gregorio, E., Palacin, J., 2011. Characterisation of the LMS200 laser beam under the influence of blockage surfaces. Influence on 3D scanning of tree orchards. Sensors 11(3), 2751-2772.

International conferences

Escolà, A., Rosell, J.R., Gil, E., Sanz, R., Arnó, J., Del Moral, I., Llorens, J., Masip, J., Gregorio, E., Planas, S., 2012. Electronic canopy characterization and variable rate application in precision fruticulture and viticulture. In: 1st RHEA International Conference on Robotics and associated High-technologies and Equipment for Agriculture. Pisa, Italy.

Gregorio, E., Solanelles, F., Rocadenbosch, F., Rosell, J.R., Sanz, R., 2011. Airborne spray drift measurement using passive collectors and lidar systems. Proceedings of the SPIE 8174, 8174IL1-12.

Kumar, D., Rocadenbosch, F., Sicard, M., Comerón, A., Muñóz, C., Lange, D., Tomás, S., Gregorio, E., 2011. Six-channel polychromator design and implementation for the UPC elastic/Raman LIDAR. Proceedings of the SPIE 8182, 81820W.

Solanelles, F., Gregorio, E., Sanz, R., Rosell, J. R., Arnó, J., Planas, S., Escolà, A., Masip, J., Ribes-Dasi, M., Gracià, F., Camp, F., 2009. Spray drift measurements in tree crops using a lidar system. In: Proceedings of the 10th Workshop on Spray Application Techniques in Fruit Growing, Wageningen, The Netherlands, pp. 40–41.

Gregorio, E., Rocadenbosch, F., Comerón, A., 2007. Design methodology of a ceilometer lidar prototype. In: Proceedings of the Geoscience and Remote Sensing Symposium IGARSS'07, pp. 3162-3165.

Gregorio, E., Rocadenbosch, F., 2007. Perspective of remote optical measurement techniques (ROMTs). In: Proceedings of the Geoscience and Remote Sensing Symposium IGARSS'07, pp. 2955-2958.

Sicard, M., Reba, M.N.M., Rocadenbosch, F., Gregorio, E., Kumar, D., Tomas, S., Comerón, A., Molero, F., Pujadas, M., Guerrero, J.L., Alados, L., Pedros, R., Martínez, J.A., 2007. Intercomparison of Spanish advanced lidars in the framework of EARLINET. In: Proceedings of the Geoscience and Remote Sensing Symposium IGARSS'07, pp. 2763-2766.

Gregorio, E., Rocadenbosch, F., Comerón, A., 2006. 905-nm biaxial lidar ceilometer prototype. Proceeding of the SPIE 6362, 63621L1-12.